

Alternating Current Electroluminescent Properties of Zinc Sulfide Powders

By

Alireza Salimian [BSc (Hons), MSc]

A thesis submitted in partial fulfilment of the requirements of the
University of Greenwich for the degree of Doctor of Philosophy

School of Science
University of Greenwich, Medway Campus
Chatham Maritime, Kent ME4 4TB, UK

January 2012



DECLARATION

“I certify that this work has not been accepted in substance for any degree, and is not concurrently being submitted for any degree, other than that of the PhD, being studied at the University of Greenwich. I also declare that this work is the result of my own investigations except where otherwise identified by references and that I have not plagiarised another’s work”.

(Alireza Salimian)

.....
PhD Supervisor/Advisor

(Prof. B. Z. Chowdhry)

19-01-2012

ACKNOWLEDGMENTS

I am deeply grateful to the following people who all, in one way or another, helped me to complete this work.

- ❖ Prof. Babur Z. Chowdhry, Greenwich University, for promoting me to complete the work and providing me with advice on the quality of this work. His kind dedication and supportive role was critical in ensuring this work was completed.
- ❖ I would especially like to thank Dr Dave Wray, Greenwich University, who provided me with an extensive amount of time and dedication in the field of ICP-MS analysis which formed a novel part of this thesis.
- ❖ Many of the staff at the Diamond and Berlin Synchrotron centre's who, with their kind assistance made an extensive difference in the novelty of X-ray analysis part of this research.
- ❖ Dr Lorna Anguilano, ETC, Brunel University, for her extensive support and expert advice in the field of X-ray powder diffraction.
- ❖ Dr Michael Thomas & Prof. John Nicholson, Greenwich University, for their administrative support

WOLFSON CENTRE, Brunel University

- ❖ Special thanks to Professor Jack Silver, Director of Wolfson Centre, Brunel University for granting me unlimited access to many of the facility's equipments and premises and providing me with dedicated advice when needed.
- ❖ Dr George Fern for his supervisory support and enabling me to have access to the Berlin and Diamond synchrotron.
- ❖ Dr Paul Harris & Prof Robert Withnal of Wolfson Centre for their valuable expert advice on the topic of ACEL phosphors.

ABSTRACT

Alternating Current Electroluminescent Properties of Zinc Sulfide Powders

In order to investigate the alternating current electroluminescent properties of zinc sulfide powders the following experiments were conducted: synthesis of zinc sulfide phosphors (comprised of zinc, sulfur and copper dopant); thermal shocking of phosphor materials (sudden cooling, using liquid nitrogen, of phosphor particles heated up to 500°C) and analysis of their alternating current electroluminescent properties as well as studies of particle crystal structures by synchrotron and conventional X-ray powder diffraction techniques. Inductively coupled plasma mass spectrometry was utilized to investigate the concentration of co-activator atoms within the zinc sulfide crystal lattice. Electroluminescent panels were prepared and the emission properties were evaluated theoretically in order to obtain a mathematical relationship between various parameters involved in the electroluminescent process.

Thermal quenching of zinc sulfide phosphor alters its photoluminescent and electroluminescent properties. The dominant wavelength of the material alters from 504 nm to 517 nm. It appears that the blue centres are vulnerable to the thermal quenching procedure carried out as the blue emission deteriorates and the overall blue emission of the material is reduced due to the role that the interstitial Cu^+ species play in this mechanism. The interstitial Cu^+ is not as stable in its location within the lattice compared to substitutional Cu^+ and hence a thermal shock is prone to effect its location or association with the surrounding atoms. The green emission centre, however, appears to be unaffected. Results obtained from layer by layer analysis of the material demonstrate that the surface of the phosphor particles contain most of the copper content (copper to zinc molar ratio of 0.08% in the surface compared to 0.06% at inner levels distributed within the lattice). The location of the outer copper layer may play a key role in the alternating current electroluminescence (ACEL) process; further experiments need

to be conducted in order to prove the foregoing hypothesis. Irrespective of the amount of copper impurity (dopant) initially added to the zinc sulfide precursor, prior to synthesis of the phosphor, during the high temperature firing of the material (above 700°C) a considerable amount of the copper will be ejected from the lattice and be washed off in the latter steps of the synthesis process (where the newly synthesized phosphor is washed in concentrated ammonia solution); an initial copper content of 1.2% molar ratio is reduced to 0.154%; however, the duration of the high temperature firing is a key factor in the final amount of copper present within the lattice.

XRPD experiments of a working ACEL device (*i.e.*, when the AC field is applied across the electroluminescent phosphor) show that the diffraction lines all shift, but remain within the region where broad diffraction intensity is observed for a powder sample (*i.e.* random orientation). Indeed the sharp diffraction lines are observed to span across each broad diffraction area associated with the sphalerite phase. The panel exhibits a different diffraction pattern when the device is powered in an AC field compared to when it is not exposed to the field. This clearly indicates that the particles possess piezoelectric properties and the electric field causes strain on the crystal lattice.

When considering the major drawbacks of ACEL technology, *i.e.* its short life time and degradation characteristics, defining a mathematical model of its emission degradation is a step towards understanding part of the mechanism of the ACEL process. Due to the various number of parameters involved in the phenomenon of electroluminescence (such as particle size, copper content and random distribution of crystal planes) and the fact that emissions arise from certain centres randomly distributed over each phosphor particle, mathematical models are only accurate when they are formulated in relation to the analysis of a particular batch of phosphor sample and used to prepare a particular panel. Hence, no overall mathematical formulation can be produced to measure the emission properties of various ACEL panels produced by different batches of zinc sulfide phosphors.

The findings of this research indicate that sample preparation technique which involves addition of raw zinc sulfide to an already copper doped zinc sulfide causes an increase in

the occurrence of nano p-n junctions species within the lattice where the copper locations form the p-type and the n type is formed from the release of some sulfur atoms from zinc sulfide structure during the high temperature firing relative to the conventional phosphor preparation methods. Larger particles have a higher probability of contacting interstitial copper sites during firing and preparation as copper atoms tend to migrate out of the zinc sulfide lattice toward the surface. Hence larger particles (commercial phosphors) demonstrate better emission properties. Thermal quenching affects the interstitial copper sites more than the other luminescent centres formed of substitutional copper sites. Hence the lowered blue emission occurs. Due to the probability of high dispersion of Cu atoms within the ZnS lattice a useful mathematical model cannot easily be developed for an EL panel. EXAFS analysis cannot be fully relied up on in respect of the interstitial copper environment in these phosphors considering that a small fraction of the copper impurity in the phosphor exists at interstitial sites. However, the results from experiments using XANES confirm a change in the electronic configuration of Zn atoms when samples are quenched.

Alireza Salimian [BSc (Hons), MSc]

*A perfection of means, and confusion of aims, seems to be our main
problem.*

Albert Einstein

**I would like to dedicate this work to my mother and father & my loving wife
Saeideh Aliakbari who motivated me in drawing aims for my life.**

TABLE OF CONTENTS

Title page.....	i
Declaration.....	ii
Acknowledgements.....	iii
Abstract.....	iv
Dedication.....	vii
Contents.....	viii
List of Figures.....	xiii
List of Tables.....	xvi
Abbreviations & Symbols.....	xvii

Chapter 1 : Zinc sulfide matrix phosphors & alternating current electroluminescence (ACEL).....	1
1.1 Phosphors.....	1
1.2 II-VI compounds and their intrinsic properties.....	1
1.2.1 Crystal structure.....	2
1.2.2 Crystal formation.....	2
1.2.3 Electronic band structure.....	3
1.3 Zinc sulfide phosphors.....	3
1.3.1 Emission spectra.....	4
1.3.2 Energy levels of luminescent centres.....	6
1.3.3 Factors affecting the luminescence & electroluminescence of zinc sulfide phosphors.....	8
1.3.4 Host lattice.....	10
1.3.5 Defects in host lattice structure.....	12
1.3.6 Host lattice-activator interactions.....	13
1.3.7 Luminescent centre and energy level positions.....	13
1.3.8 Zinc sulfide band gap.....	16

1.4 Electroluminescence	20
1.4.1 Concept of electroluminescence	20
1.4.2 Types of electroluminescence	21
1.4.2.1 Injection EL	21
1.4.2.2 High field EL	22
1.4.3 Carrier injection	23
1.4.4 Schottky barrier injection.....	23
1.4.5 Luminescence centre excitation mechanisms	26
1.5 Powder zinc sulfide phosphor electroluminescence	28
1.5.1 Alternating current (AC) powder EL.....	28
1.5.2 Ferroelectric materials used in electroluminescent panels.....	33
1.6 ACEL and its current status	34
1.7 DC powder EL	36
1.8 Overview of other display technologies	37
1.8.1 Cathode ray tubes (CRTs).....	38
1.8.2 Liquid crystal displays (LCD)	38
1.8.3 Field emission displays (FEDs)	39
1.9 Project objectives	39
Chapter 2 : Experimental techniques	40
2.1 ACEL Panel preparation using powder zinc sulfide.....	40
2.2 Analysis Study of phosphor to medium ratio in ACEL panel preparation	42
2.3 Scanning electron microscopy (SEM)	44
2.4 X-ray powder diffraction (XRD)	44
2.5 Synchrotron X-ray analysis & extended X-ray absorption fine structure (EXAFS)	46
2.6 Inductively coupled plasma mass spectrometry (ICP-MS)	50
2.7 Laser light scattering particle size analyser (HORIBA LS920).....	51
2.8 Jeti Spectro-radiometer	52
2.9 Photoluminescence (PL) emission spectroscopy	53
2.10 Elemental analysis via X-ray spectrometry	54
Chapter 3 : Improving phosphor synthesis techniques.....	55
3.1 Introduction.....	55
3.2 Zinc sulfide produced via thermal decomposition of thiourea dioxide (TDO)	55
3.2.1 Synthesis of CuS together with zinc sulfide	57
3.3 Preparation of zinc sulfide using thioacetamide	60

3.4 Using amorphous commercial luminescent grade zinc sulfide from Sylvania to prepare ACEL phosphors.....	62
3.4.1 Effect of various salts, NaCl, NaBr and NaI, as flux during the firing procedure	62
3.4.2 Firing under various amounts of NaCl as flux.....	64
3.5 Atmospheric conditions during firing.....	64
3.5.1 Firing under argon gas	65
3.5.2 Firing under hydrogen sulfide gas (H ₂ S)	68
3.6 Enhancing the preparation steps during the firing of the materials	69
3.6.1 Single firing tests	70
3.6.2 Double firing tests.....	71
3.6.3 Enhancing the double firing technique	74
3.6.4 Copper content & the double firing technique.....	77
3.6.5 Mixing copper doped and un-doped amorphous zinc sulfide prior to firing ...	80
3.7 Discussion.....	85
3.8 Key observations.....	87
Chapter 4 : Thermal quenching of commercial AC-EL zinc sulfide phosphors.....	88
4.1 Introduction.....	88
4.2 Quenching of the uncoated commercial samples.....	90
4.3 Quenching of the coated commercial samples.....	90
4.4 Multiple thermal quenching of the uncoated samples	91
4.5 Time related thermal quenching of the samples	92
4.6 Results.....	93
4.6.1 Peak emission.....	93
4.6.2 ACEL emission spectrum of thermal shock treated and untreated uncoated phosphors	95
4.6.3 ACEL emission spectrum of thermal shock treated and untreated coated phosphors	96
4.6.4 Emission properties of samples under multiple thermal quenching	97
4.7 X-ray powder diffraction (XRD) analysis of the samples	98
4.7.1 Basic X-ray analysis	98
4.7.2 The crystal structure of quenched and in-field electroluminescent phosphors investigated by synchrotron x-rays	100
4.7.2.2 X-ray analysis of the phosphor materials under controlled thermal conditions	104
4.8 Discussion.....	110

4.9 Key observations.....	112
Chapter 5 : Copper diffusion in to zinc sulfide lattice.....	113
5.1 Introduction.....	113
5.2 Preparation of the samples designed for copper content analysis via ICP-MS	114
5.3 Copper content analysis	115
5.3.1 Firing period and copper diffusion into the lattice.....	115
5.3.1.1 Initial copper content of 1.2%	116
5.3.1.2 Analysis of samples containing 0.6% copper	118
5.3.2 Firing temperature and copper diffusion into the lattice.....	119
5.4 Flux content and copper diffusion in single and double fired samples.....	120
5.4.1 Single firing preparation (AML).....	121
5.4.2 Double firing preparation (AMF)	121
5.5 Initial copper content's effect on the final amount of copper present in the lattice	123
5.6 Copper distribution within the lattice	125
5.6.1 Finding the right concentration of <i>aqua regia</i> as the digesting solution and performing the digestion	126
5.7 Discussion	132
5.8 Key observations.....	133
Chapter 6 : Effect of electric field and frequency on the emission properties of the ACEL panels.....	134
6.1 Introduction.....	134
6.1 Driving voltage and luminance	135
6.2 Electroluminescence decay at 181 volts	136
6.3 Creating a direct relationship between emission intensity, voltage and frequency	137
6.4 Luminescence decay under high driving frequency	138
6.5 Interference in the electric field	140
6.6 Luminescence studies of D1 sample under various voltages and frequencies	142
6.6.1 Voltage and frequency studies of D1 samples	143
6.6.2 Creating a relationship between the voltage and frequency	144
6.7 Crystal structure and luminescence efficiency	145
6.7.1 Voltage and frequency effect	146
6.7.2 Electroluminescence intensity decay at high frequencies.....	147
6.8 Discussion	148

6.9 Key observations.....	149
Chapter 7 Discussion	150
7.1 Thermal quenching analysis	150
7.2 Copper diffusion into the lattice	152
7.3 Efficient zinc sulfide phosphor particles.....	154
7.4 X-ray analysis of the phosphor particles.....	157
7.5 Panel analysis.....	161
7.6 Conclusion	168
7.7 Future work.....	170
REFERENCES	172
Appendix	179

List of Figures

Figure 1.1: Cubic and hexagonal crystal structure of zinc sulfide.....	2
Figure 1.2 : Luminescent centres and resulting transition in relation to the activator [X] and co-activator [Y] ratios within the zinc sulfide lattice. The activator is copper and the co-activator is chloride ²	5
Figure 1.3: Proposed energy levels within the band gap of ZnS for various dopants and acceptors ⁵	7
Figure 1.4: The spectrum of the luminescence centres excited by a single photon (1) and two-photon excitation (2). ¹⁷	10
Figure 1.5: Calculation of the energy bands in zinc sulfide from the atomic p-orbitals using the LCAO method ³¹	18
Figure 1.6: Simulation of the electronic states in ZnS, ZnS:Cl, ZnS:Cu and ZnS:Cu,Cl The yellow arrows in this diagram show the possible optical radiative transitions. Experimental values obtained for these energy levels match very closely to the predictions of the above diagram.....	19
Figure 1.7: Types of electroluminescence mechanism and related applications.....	21
Figure 1.8: Injection EL, electron and hole interaction within the band gap confinement and light emission ²⁰	22
Figure 1.9: The force imposed on an electron by an electric field.....	24
Figure 1.10: Different excitation mechanisms of luminescent centres (e: electron, H: hole) ³⁹	27
Figure 1.11: The structure of the Destriau cell, a mixture of the EL phosphor and dielectric medium is placed between two electrodes; upon application of alternating current light is emitted from the phosphor layer.....	28
Figure 1.12: Electroluminescence from ZnS:Cu,Cl particles. The double comet lines are illustrated at the threshold ($E=E_{th}$) voltage and above ($E>E_{th}$).....	30
Figure 1.13: Injection of electrons and holes from opposite ends of a Cu_2S needle into the ZnS:Cu,Cl surrounding lattice.....	31
Figure 1.14: ACEL panels are the only flexible light emitting panels available, specially where low ambient lighting is present they are a fantastic solution to decorative & information display ideas, Jaguar use Electroluminescent products to light the interior of their C-X75 Concept Car.....	35
Figure 1.15: Structure of a DCEL device ⁵⁵	37
Figure 2.1: Demonstration of the ACEL panel structure.....	41
Figure 2.2: Effect of phosphor to medium binder ratio on the emission of the ACEL panel. The ratio of 80% phosphor powder to medium is the optimum ration after which the luminance of the material will tend to decrease.....	43
Figure 2.3 Optical layout of the KMC-2 unit at Bessy II ⁶³	49
Figure 2.4: Plasma forming unit of the ICP-MS instrument.....	50
Figure 2.5: Analysis of the emission intensity, spectrum and dominant wavelength are calculated and presented by Jeti Spectrometer.....	52
Figure 2.6 A simple representation of PL analysis. The sample is stimulated by a static wavelength and meanwhile screened for emissions. In this example, the imaginary sample is stimulated at a wavelength of 360 nm and the emission at 600 nm is detected. (Note that this diagram does not represent the actual mode of action by a specific PL spectrometer).....	53
Figure 3.1: Reactions occurring during the thermal decomposition of thiourea dioxide.....	56
Figure 3.2: Electroluminescent property of Cup004 and Cup0004 samples compared to commercial Sylvania ACEL phosphor at 100 Hz frequency using 181 and 113 V driving voltage.....	58
Figure 3.3: SEM analysis of Cup004 sample; fine powders agglomerated.....	59
Figure 3.4: X-ray powder diffraction of sample Cup004 compared to commercial sample. Both samples demonstrate cubic crystal structure.....	59
Figure 3.5: X-ray powder diffraction of copper doped zinc sulfide prepared by thioacetamide route with cubic crystal structure.....	61
Figure 3.6: ACEL emission of the ZnS:Cu phosphors fired using NaCl, NaI & NaBr as flux compared to the commercial zinc sulfide phosphor from Sylvania (intensity unit: $Cd/m^2 \times 10^4$).....	64
Figure 3.7: Firing of zinc sulfide in an argon controlled atmosphere.....	66
Figure 3.8: SEM analysis of the SAr0 (left) and SAr1(right) samples after firing at 850°C.....	66
Figure 3.9: X-ray powder diffraction of SAr0 and SAr1 samples. The cubic crystal structure of the powders is unaffected by addition of sulfur.....	67
Figure 3.10: Firing of zinc sulfide under hydrogen sulfide & nitrogen controlled atmosphere.....	68

Figure 3.11: Firing of the materials in covered crucible, using NaCl bath to ensure the material is cooled steadily when removed from the furnace.....	70
Figure 3.12: SEM analysis of samples AmL1 (bottom), AmL2 (top left) and AmL4 (top right & bottom). 71	71
Figure 3.13: SEM analysis of samples AmF1 (top left), AmF2 (top right), AmF3 (bottom left) & AmF4 (bottom right).	72
Figure 3.14: X-ray powder diffraction of AmF2 & AmL2 samples. No observable difference in crystal structure.	73
Figure 3.15: The ratio of Cu/Zn in terms of moles of copper per 100 moles of zinc based on results from ICP-MS analysis for AmF and AmL samples compared to commercial grade Sylvania ACEL ZnS:Cu phosphor.	74
Figure 3.16: ACEL emission intensity of commercial copper doped zinc sulfide produced by Sylvania at 181 Volts and 400Hz frequency.	75
Figure 3.17: ACEL emission of T22A (red) and T22B (green) compared to commercial Sylvania phosphor at 181 volts and 400Hz frequency. No significant difference between the two samples but weak emission compared to the commercial samples.	76
Figure 3.18: ACEL emission of T22C (Red) and T22D (green) compared to commercial Sylvania phosphor at 181 volts and 400Hz frequency. The synthesis technique of T22C seems inferior to the other T22 samples in terms of intensity output.	76
Figure 3.19: ACEL emission of the H1,2 and 3 samples compared to Sylvania phosphor at 113 volts and 400Hz.....	78
Figure 3.20: ACEL emission of the H1S,H2S and H3S samples compared to Sylvania phosphor at 113Volts and 400Hz.The H2S and H3S samples demonstrate weak emission possibly due to the low level of copper impurity present in ZnS host as illustrated in figure 6.21.	79
Figure 3.21: The ratio of Cu/Zn in terms of moles of copper per 100 moles of zinc, based on results from ICP-MS analysis for H series samples.H1 and H1S samples contain the highest amount of copper impurity.	79
Figure 3.22: D1 (red: 113v, green 123v, purple 181v) sample compared to Sylvania (blue 181v) using 400 Hz frequency. This sample is a close match (66.66%) to commercial samples.	81
Figure 3.23: D1 sample (red) compared to D2 (pink) using 113v driving voltage and 400Hz frequency....	81
Figure 3.24: SEM analysis of D1 samples. Particle's sizes range from 1-10 microns.	82
Figure 3.25: SEM analysis of D2 samples. Particle's sizes range from 1-10 microns.	82
Figure 3.26: Surface of panel prepared by the D1 phosphor. D1 samples due to their smaller size (~5 microns) demonstrate closer packing along with agglomerations when screen printed.	83
Figure 3.27: Surface of panel prepared by the Sylvania phosphor. The larger size of these particles (~30 microns) seems to create a more homogenous film when screen printed.	84
Figure 3.28: X-ray powder diffraction of the D1 sample demonstrating cubic crystal structure.....	84
Figure 3.29: Scanning electron microscopy of Sylvania particles.	85
Figure 4.1 Instant cooling of samples with liquid nitrogen.	89
Figure 4.2: The relationship between luminance and the associated driving voltage (113V and 181V) of the nitrogen shock treated samples at 400Hz frequency. Thermal shocking reduces the overall emission of the phosphors.....	93
Figure 4.3: Dominant emission wavelength of the nitrogen shock treated samples at (113V and 181V) under 400Hz frequency compared to that of an untreated sample. Dominant wavelength is shifted toward a longer wavelength.	94
Figure 4.4: ACEL emission spectrum of uncoated samples (liquid nitrogen shocked and cooled steadily) at 181V and 400Hz.Quenched samples demonstrate both change to spectrum and intensity whileslowly cooled samples only demonstrate reduction in emission intensity.	95
Figure 4.5: ACEL emission spectrum of coated samples (liquid nitrogen shocked and cooled steadily) at 181V and 400Hz. Quenched samples demonstrate both change to spectrum and intensity whileslowly cooled samples only demonstrate reduction in emission intensity.	96
Figure 4.6: ACEL emission spectrum of uncoated samples repeatedly (3 times) heated to 500°C and rapidly cooled by liquid nitrogen shocked at at 181V and 400 Hz. Repeated firing does not alter the dominant wavelength but reduces the intensity of emission.	97
Figure 4.7: ACEL emission spectrum of uncoated samples heated to 500°C for 20, 40 and 60 minutes and rapidly cooled by liquid nitrogen at 181V and 400 Hz.Extended heating time does not alter the amount of dominant wavelength shift but reduces the intensity.	97

Figure 4.8: XRD analysis of coated and uncoated Sylvania phosphors treated at 500°C followed by nitrogen shocking compared to untreated standard sample. The cubic crystal structure of these samples is unaffected.	98
Figure 4.9: XRD analysis of coated and uncoated Sylvania phosphors treated at 500°C and cooled steadily compared to untreated standard sample. The cubic crystal structure of these samples is unaffected.	99
Figure 4.10: XRD analysis of uncoated Sylvania phosphors heated at 500°C for 20, 40 and 60 minutes and cooled by liquid nitrogen compared to untreated standard sample. The cubic crystal structure of these samples is unaffected.	99
Figure 4.11: XRPD of the ACEL phosphors (GU400S-blue and GU400N-red line). The cubic (333) lattice parameter seems to be reduced extensively.	102
Figure 4.12: XAS data in R and E (inset scale). The Zn K-edge XAS data do not allow for an easy understanding of the subtle crystallographic differences between quenched and non-quenched specimens. However, the data indicate that the electronic structure has altered due to changes in Zn K-edge shape. ...	103
Figure 4.13: Expansion of XRPD pattern of EL phosphor deposited in the EL panel. The orange line is 'off' and the black line shows the panel in operation. The top grey line shows the broad powder pattern observed in a capillary. All the peaks do shift when the field is applied.	104
Figure 4.14: X-ray powder diffraction analysis of uncoated Sylvania phosphors at room temperature, 100°C, 200°C and 400°C. All peaks are shifted to the left when analysis is carried out at higher temperatures.	106
Figure 4.15: X-ray powder diffraction analysis of uncoated Sylvania phosphors at room temperature, 100°C, 200°C and 400°C compared to quenched and steadily cooled samples, demonstrating the crystal planes shifting when the sample is heated.	107
Figure 4.16: Alternation in intensity of peaks related to certain crystal planes after quenching the uncoated Sylvania sample at 400°C.	108
Figure 4.17: Demonstration of the percentage change in peak intensity of the crystal planes after the standard uncoated Sylvania phosphor is quenched at 400°C. H prefix indicates crystal planes related to hexagonal crystal form, otherwise cubic. Various peaks are reduced in an irregular fashion.	109
Figure 5.1: Sylvania zinc sulfide particles. The particles are composed of nanorods that agglomerate to form the 1.5 micrometer particles.	116
Figure 5.2: The ratio of Cu/Zn in terms of moles of copper per 100 moles of zinc (% molar) based on results from ICP-MS analysis.	117
Figure 5.3: The ratio of Cu/Zn in terms of molar % based on results from ICP-MS analyses for D20-80 samples. D40 samples contain the highest level of copper impurity.	119
Figure 5.4: The ratio of Cu/Zn in terms of moles of copper per 100 moles of zinc (molar %) based on results from ICP-MS analysis for AMT samples. Hexagonal crystal structures contain less copper impurity compared to the cubic structure.	120
Figure 5.5: The ratio of Cu/Zn in terms of moles of copper per 100 moles of zinc (molar %) based on results from ICP-MS analysis for AmF and AmL samples compared to commercial grade ACEL ZnS:Cu phosphor produced by Sylvania.	122
Figure 5.6: The ratio of Cu/Zn in terms of moles of copper per 100 moles of zinc (molar%) based on results from ICP-MS analysis for H series samples. H1 series have the highest copper impurity.	124
Figure 5.7: Layer by layer digestion of the phosphor particle.	125
Figure 5.8: Proposed interpretation of the findings from layer by layer digestion of the Sylvania samples. A: even distribution of the copper all over the lattice, B: copper distribution in the outer layers of the lattice, and C: copper distribution in the inner layers of the lattice.	126
Figure 5.9: The setup of the phosphor and digesting solution.	127
Figure 5.10: Plot of $\{[Cu\text{ mg/l}]/[Zn\text{ mg/l}]\}$ against time (s) for 30% and 40% digesting solution concentrations.	128
Figure 5.11: Effect of digestion on the surface of the Sylvania phosphor particles. A: Untreated, B: 60 seconds, C: 120 seconds, D 180 seconds.	129
Figure 5.12: Effect of digestion on the surface of Sylvania phosphor particles. A: after 5 minutes treatment B: untreated sample.	130
Figure 5.13: Proposed mapping of the copper distribution within the zinc sulfide particles. It seems the surface of the phosphors contain higher ratio of copper to zinc (molar ratio) compared to the inner core layers.	131
Figure 6.1: Plotting luminance of the panel against the driving voltage at 400Hz frequency.	135

Figure 6.2: Luminance decay over a period of 500min, 181V and 400Hz.	137
Figure 6.3: Effect of various frequencies on the luminescence over time.	139
Figure 6.4: Graphical presentation of the parameter a based on the dielectric used and the quantity of it. Bothe dielectrics reduce the parameter ' a ' however, strontium titanate seems to be reducing the compared to barium titanate.	142
Figure 6.5: Relationship between driving voltage and luminance at various frequencies using AMT850 zinc sulfide phosphors which are fired at 850°C with a cubic crystal structure.	146
Figure 6.6: Relationship between driving voltage and luminance at various frequencies using AMT1050 ZnS phosphors which are fired at 1050°C with a hexagonal crystal structure.	146
Figure 7.1: FESEM image of a single Osram Sylvania _type 728_-uncoated ACEL ZnS:Cu-based particle after etching with hydrochloric acid for 15 min, showing the layered structure along the [111] direction and pyramids at one end (courtesy of Wolfson Centre, Brunel university).	156
Figure 7.2: Estimated values of ' a ' at various frequencies in respect of formula 7.2 for AMT850 and AMT1050 samples. This parameter is affected more intensely in cubic crystal structure.	165
Figure 7.3: Estimated values of ' α ' at various frequencies in respect of formula 7.2 for AMT850 and AMT1050 samples. This parameter seems to be effected similarly for both cubic and hexagonal crystal structures.	166
Figure 7.4: Estimating the parameters (A and B) of formula 6.8c for AMT850 and AMT1050 at different frequencies.....	167

LIST of TABLES

Table 2.1: Various phosphor to oil ratio's for preparation of the ACEL panel and the panel luminance of the combination (based on average of five samples)	43
Table 2.2: Applications of X-ray powder diffraction. (Source: Max Planck institute for Metals research, Stuttgart, Germany).	46
Table 5.1: The amount of Cu and Zn found in Am1 and Am2 samples based on the ICP-MS results.....	117
Table 5.2: The amount of Cu and Zn found in D20-80 samples based on the ICP-MS results.	118
Table 5.3: Cu and Zn concentration of AMT samples based on the ICP-MS results.	120
Table 5.4: The amount of Cu and Zn found in AmF and AmL samples based on the ICP-MS results.	122
Table 5.5: Concentration of Cu and Zn found in AmF and AmL samples based on ICP-MS analysis.	124
Table 6.1: Estimated values of each variable in relation to the frequency of the AC current based on the model three.	140
Table 6.2: Preparation of sample with added dielectric material quantities.	141
Table 6.3: Estimation of the parameters (a & α) considering the equation 7.3 for AMT850 and AMT1050 samples.	147
Table 7.1: Estimating the parameters of formula 6.8c for AMT850 and AMT 1050 at different frequencies.	167

Abbreviations & Symbols

ACEL: Alternating current electroluminescence
CRT: Cathode ray tube
DCEL: Direct current electroluminescence
EL: Electroluminescence
EXAFS: Extended X-ray absorption fine structure
EDAX: Energy dispersive analysis by X-rays
FED: Field emission displays
ITO: Indium tin oxide
ICP-MS: Inductively coupled plasma mass spectrometer
LCD: Liquid crystal displays
LCAO: Linear combination of atomic orbital
PET: Polyethylene terephthalate
SEM: Scanning electron microscopy
TDO: Thiourea dioxide
XRPD: X-ray powder diffraction
XANES: X-ray absorption near edge structure

Chapter 1 : Zinc sulfide matrix phosphors & alternating current electroluminescence (ACEL)

1.1 Phosphors

The simplest description of a phosphor is a substance that exhibits luminescence. Luminescence can be described as the emission of visible light from a material due to external excitation (not to be confused with incandescence; the emission of light from a heated material, such as a light bulb). Structurally, phosphor materials are described in terms of a host lattice ‘activated’ by a low concentration of another element. The term “activator” is slightly archaic as it is now known that more than one element in a host lattice can take part in luminescent emission and dopant or doping element is a more correct term to use for referring to the impurity element. Taking silver and aluminium doped zinc sulfide phosphors as examples; phosphors are written as follows: “ZnS:Ag,Al” indicating silver and aluminium as doping elements within a zinc sulfide host lattice.

1.2 II-VI compounds and their intrinsic properties

Sulfides, oxides, selenides and tellurides of zinc, cadmium and mercury are referred to as “II-VI” phosphors. Among this group of phosphors zinc sulfide has been the most widely used. The first time that zinc sulfide particles were observed to demonstrate luminescence was in 1866 when Theodor Sidot, a French scientist, synthesised these particles for the purpose of crystal growth and crystal studies¹.

1.2.1 Crystal structure

Two types of crystal structure have been observed with the II-VI group of materials, the cubic (zinc blende) or the hexagonal (wurtzite) structures (Figure 1.1). However, zinc sulfide has been observed in both forms depending on the firing temperature at which it has been crystallised.

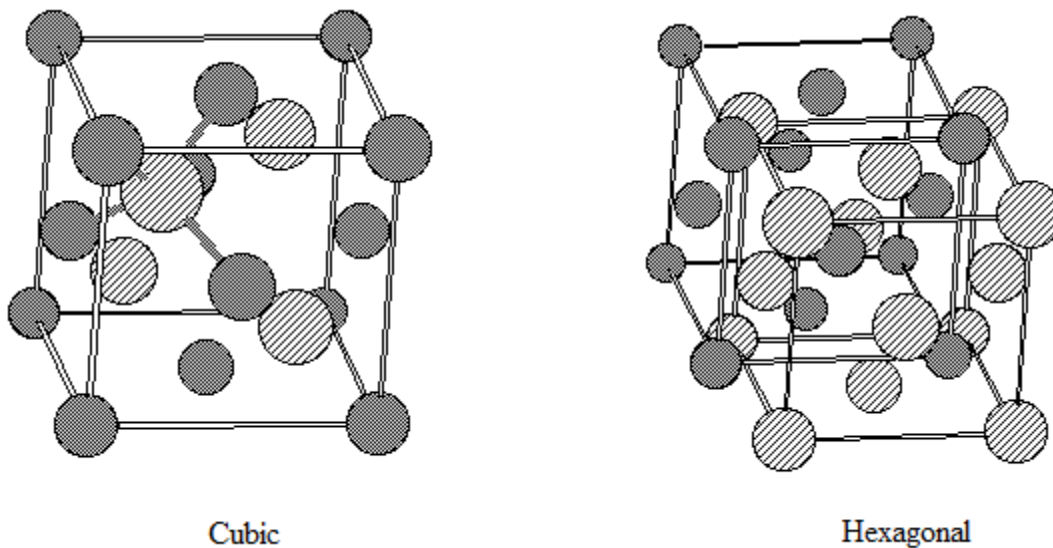


Figure 1.1: Cubic and hexagonal crystal structure of zinc sulfide.

1.2.2 Crystal formation

Type II-VI materials do not melt at relatively high temperatures, but do sublime. This is because these materials demonstrate a very high sublimation pressure. For example zinc sulfide sublimates at 1830 °C.

The usual procedure of making zinc sulfide phosphor particles involves firing of amorphous zinc sulfide material in crucibles at temperatures between 800-1200°C to

form crystalline particles, where a change from a cubic to a hexagonal crystal structure occurs at temperatures above 1020°C (the phosphor transition temperature). The crystal structure is fundamental to phosphor properties of these materials.

1.2.3 Electronic band structure

In type II-VI materials, the conduction band reside on the s orbital of the cation (zinc) while the valence band resides on the p orbital of the anion (sulfur). In these types of semiconductor materials, if either of the elements are replaced by heavier atoms, the band gap energy, E_g , of the material is decreased except in zinc oxide (3.37 eV) where E_g is smaller than zinc sulfide (3.68 eV)^{1,54}.

The direct band gap of the II-VI materials makes them ideal candidates as host materials for phosphors with a zinc sulfide band gap of 3.68 eV for the cubic and 3.91 eV for the hexagonal structures. The radiative emission in phosphors is caused by transitions taking place via energy levels of activators introduced as impurity materials. Perturbation of the conduction band creates the associated energy levels of impurity materials in the host lattice¹.

1.3 Zinc sulfide phosphors

Addition of metals, as impurities, to zinc sulfide during firing leads to phosphor materials which demonstrate the luminescent properties of the metal impurities. Addition of copper, for example, produces green emitting phosphors while replacing the copper with silver generates a blue emission. Since the host lattice's ability to exhibit luminescence is

activated by the addition of such materials, the term *activator* is used to describe the metal impurity to be incorporated into the host lattice.

It was demonstrated by Kroger¹ that the halide flux added during the firing procedure of zinc sulfide phosphors, not only acted as a crystal growth promoter, but also it incorporated halide atoms into the lattice which had an effect on the formation of luminescent phosphors. The halide atom is therefore referred to as the co-activator.

1.3.1 Emission spectra

The luminescent properties of copper or silver doped zinc sulfide materials can be divided into five groups depending on the ratio of the activators and co-activators incorporated into the lattice (Figure 1.2)². As described earlier, the luminescent properties of the phosphor material are related to the luminescent centres, which are composed of the activator and co-activator as well as the interactions between them. As illustrated graphically in Figure 1.2, the nature of these luminescent centres governs the emission specificity of the luminescence.

Green-Cu centre (G-Cu): this type of centre can be formed by copper or silver activators in combination with aluminium, chlorine or bromine co-activators in equal ratios within the lattice. The luminescence transition takes place from the co-activator level to the activator level in different combination pairs having different distances between each. These centres generate spectra that consist of broad bands which are well distinguished from the edge bands.

Self Activate centre (SA): these centres are formed in the absence of copper atoms as a result of divalent zinc vacancies with mono-valent chlorine or trivalent aluminium sites

(if aluminium impurity existed). Two chloride ions compensate the charge deficiency of the divalent zinc with one of the chlorine atoms associating directly with the zinc whilst the other is isolated and remains responsible for the primary state of the emission. The geometrical symmetry of the hole at the divalent zinc vacancy determines the polarization of the luminescence.

Red-Cu centre (R-Cu): it has been shown that these centres are formed by mono-valent copper vacancies substituting the zinc vacancy and closest divalent sulfur vacancies to the site. This implies the reverse of what has been observed with the SA centres in respect of activator and co-activator relationship³.

Blue-Cu centre (B-Cu): it has been suggested that these centres may form as a result of an association between the mono-valent substantial and interstitial copper vacancies⁴.

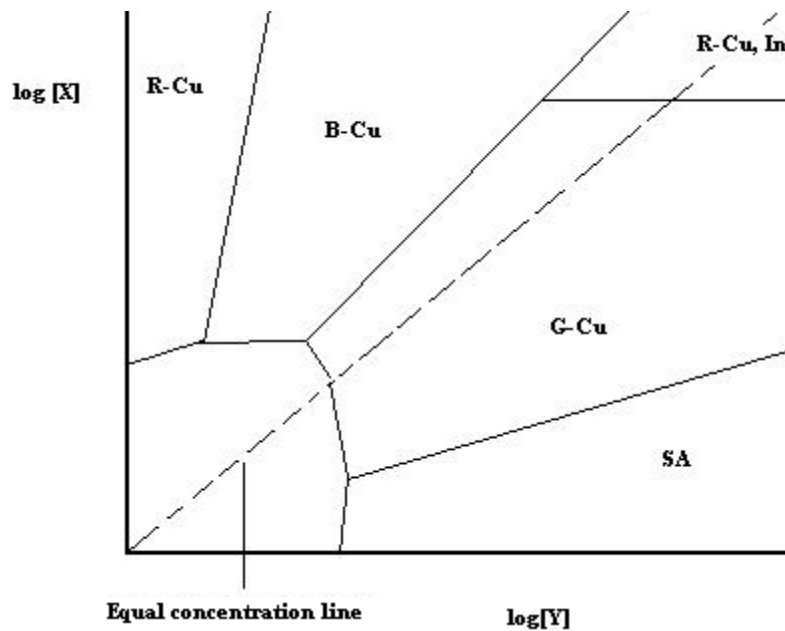


Figure 1.2 : Luminescent centres and resulting transition in relation to the activator [X] and co-activator [Y] ratios within the zinc sulfide lattice. The activator is copper and the co-activator is chloride².

1.3.2 Energy levels of luminescent centres

Figure (1.3)⁵ demonstrates some of the proposed energy levels within the band gap of zinc sulfide for various dopants and acceptors. Zinc sulfide, in its pure form, demonstrates UV emissions (~ 3.37 eV) but lacks any visible luminance⁶. Substituting Cl^- for S without any other activator, e.g. copper, results in a blue line being observed near 440 nm (2.8 eV). In this situation the material, as described earlier, is referred to as self-activating (SA). As the chlorine has only one negative charge, a compensating charge defect- e.g. two Cl^- ions must reside on the S sites together with a Zn vacancy. Shinoya et al⁷ suggested this Zn vacancy is involved in the 2.8 eV blue emission. When Cu atoms are substituted at the Zn sites in absence of Cl co-activator, a blue line emission close to the SA centre and a red line at 677 nm (1.81 eV) appear. The intensity of the red line depends on the preparation technique involved⁸.

It is necessary to consider that all doped zinc sulfide samples (doped with Cu, Cl or a combination of both) are diamagnetic over a wide temperature range from 1.5 to 300 K⁹. As a result a wide range of paramagnetic defects are ruled out, including Cu^{2+} , Cu^0 and even Zn^{1+} or S^{1-} defects. Hence the copper in all these materials has to be in a Cu^{1+} state, when not excited. The Cu^{1+} has a d^{10} configuration without any empty d states; however, when a hole is trapped on a substitutional Cu^{1+} , one of the d states becomes vacant and a temporary d^9 configuration Cu^{2+} is formed¹⁰. In cubic symmetry the d state splits into t_2 and e states, equivalent to 0.75-0.95 eV. Suzuki and Shionoya suggested that the highest t_2 state is about 1.3 eV above the valence band for a Cu-Cl pair¹¹. Suzuki & Blinks et al¹² explained the Cu-B line as a pair of adjacent substitutional and interstitial Cu^+ sites. There are three blue lines observed in ZnS:Cu.Cl band gap systems: a blue line for only

Cl doping (SA centre), a blue line for Cu only (Cu-B), and a blue line when the host lattice is doped with both Cu and Cl. It is not clear if these are really the same line or distinct lines; currently, they are considered as aggregate Cu cluster emissions. When Cl or other co-activators such as Br are added together with Cu, a green 520 nm line is observed equivalent to 2.4 eV energy band together with the blue line; the blue or green emission is dependent on the Cu/Cl ratio. For the blue line to be dominant, the optimum Cu concentration is 0.065% with a low Cl concentration, while for 0.01-0.04% Cu with comparable Cu and Cl concentrations, the green line is dominant¹⁰. The actual numbers of possible luminescence centres are far more than what has been mentioned here¹³; hence Figure 1.3 provides a summary of the proposed defect energy levels.

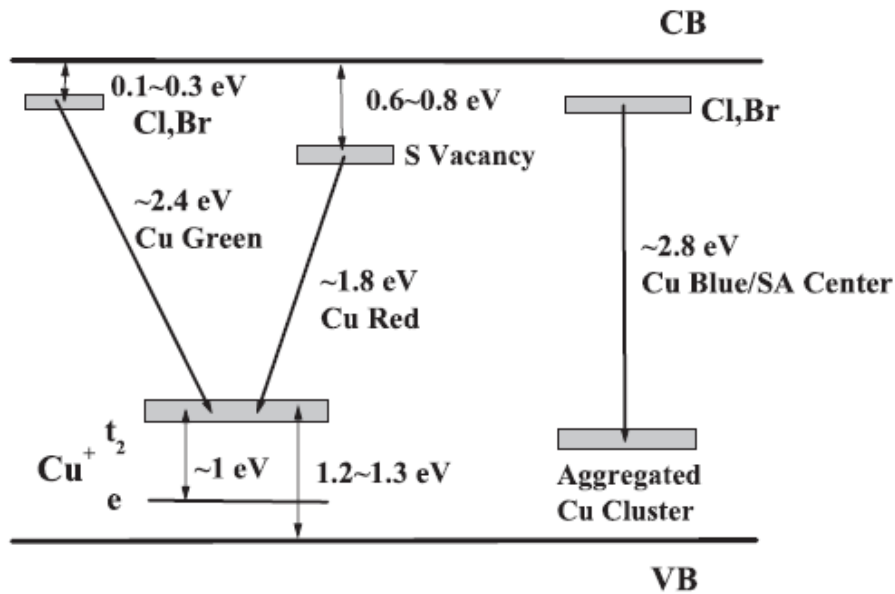


Figure 1.3: Proposed energy levels within the band gap of ZnS for various dopants and acceptors⁵.

1.3.3 Factors affecting the luminescence & electroluminescence of zinc sulfide phosphors

A small contamination of the zinc sulfide phosphors prior to firing with group VIII B elements (Fe, Ni and Co) reduces and even totally extinguishes the luminescence intensity of the phosphor material; such materials are referred to as luminescence killers¹⁴. This is because group VIII B ions have absorption bands residing in the visible spectrum and their associated spectra overlap that of G-Cu centres. It has been suggested that resonance energy transfer from excited G-Cu centres to the iron group ions takes place and hence by interfering with the luminescence function of the G-Cu centre, the luminescence efficiency is decreased¹⁴.

Overly high concentrations of activator atoms would result in the loss and elimination of luminescence; it has been hypothesised that the Auger effectⁱ may be involved in the loss of luminescence¹⁵. The energy of the excited copper-copper pairs is transferred to the unexcited activators across the lattice, raising electrons to the conduction band. This means the energy encircles the lattice and is released through non-radiative recombination traps.

Zinc sulfide phosphors lose their emission quality over time and it has been proposed that the reason for the ageing of copper doped zinc sulfide phosphors (ZnS:Cu) is due to the migration of the interstitial Cu^{2+} ions away from their proposed locations within the lattice¹⁶. It is well known that the barrier regions of electroluminescent spots (areas on the phosphor particle surface that seem to emit light) are localized in separate small areas

ⁱ The Auger effect is a phenomenon in physics in which the emission of an electron from an atom causes the emission of a second electron. When an electron is removed from a core level of an atom, leaving a vacancy, an electron from a higher energy level may fall into the vacancy, resulting in a release of energy. Although sometimes this energy is released in the form of an emitted photon, the energy can also be transferred to another electron, which is ejected from the atom. This second ejected electron is called an Auger electron.

corresponding to dislocations and second-phase inclusions¹⁶. It can therefore be assumed that the different kinds of luminescent centres have a different distribution pattern within the zinc sulfide crystal lattice.

The formation of the luminescent sites results from the initial stages of phosphor firing during which the zinc sulfide are formed in their crystalline form¹⁷. At a high temperature (above 700°C), copper is incorporated into the nodes occupying zinc vacancies, generating the "green" luminescent centres. During the cooling of the fired phosphor a portion of the copper atoms shift to the interstitial sites, forming the "blue" luminescent centres with a 2.8 eV band gap and the number of "green" centres with a band gap of 2.4 eV decrease. Additional dopants such as halides are used to introduce defect states into the lattice to further enhance EL efficiency. A low percentage of copper in the lattice results in blue emissions where the Cu exists in defect centres¹⁷.

The association of the green band with radiation of the centres localised in the surface region of zinc sulfide crystals has been proved via studies in which nanocrystalline copper doped zinc sulfide materials demonstrated green luminescence only¹⁸.

Kokin et al¹⁷ investigated the spectra of two-photon excited luminescence of powder zinc sulfide and measured its electroluminescence spectra under different conditions at different stages of degradation. It was proposed that the centres of green and blue luminescence are non-uniformly distributed over the grains. Their two-photon-excited luminescence analysis provided valuable information on luminescent centre locations in the volume of the crystal; these findings are presented in Figure 1.4.

I , rel. units

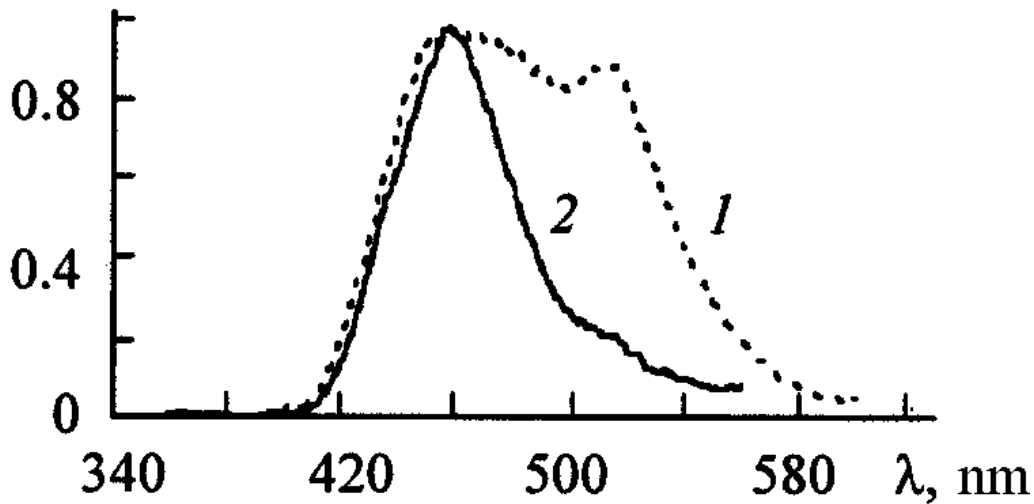


Figure 1.4: The spectrum of the luminescence centres excited by a single photon (1) and two-photon excitation (2).¹⁷

1.3.4 Host lattice

Electroluminescent phosphors can be regarded as complex solid solutions of crystals¹⁵ where the exact combination of atoms present in the solution gives rise to the unique photo-emissive properties of the phosphor. In the case of zinc sulfide phosphors, the zinc sulfide lattice can be regarded as the host solvent while luminescent centres or activators are the solute components of this solid solution. High field electroluminescent materials should have a set of five specific properties¹⁹ which would make them qualify as possible hosts. These properties are as follows:

- I. The proposed host should provide within its structure a substitutional lattice site for the luminescent centre.
- II. The material should be non-conducting in order to provide capacitive behaviour when placed under high electric fields ($\sim 10^5 \text{ Vcm}^{-1}$).
- III. The material should have high breakdown strength in the region of 1MV cm^{-1} .
- IV. A low phonon electron coupling constantⁱⁱ together with a higher state of crystalline structure with doping material present is required to minimize electron scattering.
- V. The band-gap of the material must be high (about $\sim 3.1 \text{ eV}$) to ensure that the generated light is not absorbed by the host lattice.

Zinc sulfide together with other sulfide based type II-VI compounds satisfies these requirements. The direct band gap of ZnS is wide enough to be transparent to the whole visible spectrum while electron momentum is conserved during the transition between the valence and conduction bands¹⁹.

Other properties of zinc sulfide such as effective electron mass ($0.4 m^*/m^0$)ⁱⁱⁱ, large dielectric constant of 8.9, low phonon energy and small phonon-electron coupling constant along with its band gap (3.68 eV) makes zinc sulfide one of the best high field electroluminescent phosphors²⁰.

ⁱⁱ Coupling of vibration energy of phonons and ionisation of electrons can lead to build up of heat.

ⁱⁱⁱ In a simplified picture that ignores crystal anisotropies, the electrons behave as free particles in a vacuum.

1.3.5 Defects in host lattice structure

Defects in zinc sulfide are either associated with zinc or sulfur positions in which case they are referred to as intrinsic point defects or these point defects are associated with the presence of an impurity element referred to as extrinsic point defects. As already discussed, the impurity is the doping element used in synthesis of these materials. The optical and electrical properties of semiconductors are significantly influenced by these defects both qualitatively and quantitatively; however measurements of these parameters are virtually impossible due to the complicated nature of the system²¹.

Intrinsic point defects in zinc sulfide, include the vacancies on cation and anion sub-lattices which accordingly relate to Zn^{2+} and S^{2-} . Some of the point defects have been characterised in zinc sulfide; for example, a double ionized zinc vacancy is reported to create a defect level ~ 1.0 eV above the valence band edge²².

Extrinsic point defects present in zinc sulfide create an interesting electron-hole interaction environment which has attracted many researchers to investigate the process. Photoconductivity measurements have illustrated the presence of a donor level 0.25 eV below the conduction band of zinc sulfide, when chlorine has been substituted as an anion in the zinc sulfide lattice²³ while an ionized acceptor level appears which is thought to be associated with induced compensating isolated zinc vacancies. However, there are many debates in relation to the defects in zinc sulfide due to the complex nature of the electronic structure. Assignment of defect levels in the band gap of zinc sulfide is also a current topic of debate between researchers.

1.3.6 Host lattice-activator interactions

When an activator is placed within the zinc sulfide host lattice, the electrons associated with the activator arrange themselves in such a way so as to minimise the energy of the activator ion. This arrangement is disrupted when an external electrical or magnetic field is applied. Outer shell electrons, unlike inner shell electrons, are mostly affected by these fields and hence the energy levels associated with them would be greatly influenced by these fields, particularly when $d-d$ or $d-f$ radiative transitions are involved^{22,23,24}.

1.3.7 Luminescent centre and energy level positions

The position of the activator ion within the host lattice is referred to as the luminescent centre. Many factors influence the energy level of these centres, most importantly lattice symmetry, bond length and molecular orbital overlap between cations and anions²⁴. Crystal field theory can be used to understand how lattice symmetry can be an important factor in determining these energy levels within the crystal. In crystal field theory the metal ion is assumed to be free in gas form and the ligands behave like point charges while it is assumed that the orbitals of the metal and the ligands do not interact. In this context the attraction between the positively charged metal ion and the electrons of the ligand bonds the two together and crystal field theory describes how the ligands influence the d electrons of the metal and split them into lower and higher energy levels. The energy difference between the two energy levels depends on the following factors:

- Nature of the metal ion (cation).
- Oxidation state of the cation. A higher oxidation state leads to a larger splitting.
- Arrangement of the anion (ligands) around the metal ion.

- Type of anion surrounding the metal ion. The stronger the effect of the anion then the greater the difference between the low and high energy $3d$ groups.

In transition metals, there are five partly filled d -orbitals, each capable of containing two electrons. These five d -orbitals are degenerate - they have the same energy - when there are no ligands around the metal. When an anion approaches the metal ion, the electrons of the anion will be closer to some of the d -orbitals and further away from others. The d -electrons closer to the anion will have a higher energy than ones further away because they sense more repulsion and hence the d -orbitals split in energy. What determines the way that the orbitals split is the orientation of the anion with respect to the metal d orbitals. The most common type of complex is octahedral where six anions position themselves around the metal ion pointing directly at the metal d -orbitals causing splitting of the energy levels. If instead of six, four anions form a tetrahedron around the metal ion, their electrons are not oriented directly towards the d -orbitals resulting in a lower splitting of the energy levels.

If there are six anions there will most likely be one along each axis, so the complex will have octahedral symmetry. Because the d_{xy} , d_{xz} and d_{yz} orbitals are further away from the anion (ligand), they will be lower in energy than the d_z^2 and $d_{x^2-y^2}$, which are closer to the anion. In tetrahedral crystal field splitting, the reverse occurs, the lower energy orbitals will be d_z^2 and $d_{x^2-y^2}$, and the higher energy orbitals will be d_{xy} , d_{xz} and d_{yz} .

Considering zinc sulfide doped with copper, in a tetrahedral symmetry the t_{2g} ($3d_{xy}, 3d_{y^2}, 3d_{xz}$) components of the metals doubly degenerate d -orbitals point at the sulfur

ligands and an electron from one of these orbitals must come close to the unpaired electron of the sulfur causing a repulsion which will increase the energy of the d -orbital electron. Contrary to the foregoing, the e_g ($3d_{z^2}$ and $3d_{x^2-y^2}$) orbitals point between the ligands and their associated energy levels will not be altered by the ligands. As a result of this symmetry in positioning of the atoms, the e_g levels will be lower in energy compared to the t_{2g} level²⁵.

The bond length of the host material influences the energy level of the luminescent centre in a different way. By considering Coulomb's law^{iv}, treating the constituent atoms of the lattice as point charges the effect of bond length on energy levels can be explained in a different approach. Coulomb's law can be stated as:

$$F = \frac{q_1 \cdot q_2}{4\pi \cdot \epsilon \cdot r^2} \quad (1.1)$$

Where q_1 and q_2 are the respective charges with distance r between them and a dielectric permittivity of ϵ . The electrostatic force on a point charge q in space under the influence of an electric field E is given by:

$$F = q \cdot E \quad (1.2)$$

So

$$E_q = \frac{q}{4\pi \epsilon \cdot r^2} \quad (1.3)$$

^{iv} Coulomb's law, describes the electrical forces present between two charged particles.

This (equation 1.3) demonstrates the local electric field due to charge q . The above equations demonstrate that as the bond length r increases, the related electrostatic force and field decrease.

Using point charges as a model, Gerloch²⁶ proposed equation 1.4 as the relationship between energy level separation and charge of the anion.

$$D_q = \frac{1}{6} z e^2 \frac{\alpha^4}{r^5} \quad (1.4)$$

Where D_q is a measure of the energy level separation, z is the charge of the anion, e is the electron charge, α is related to the wave function of d -orbital and r is the bond length. This equation clearly shows that transitions involving d -orbital, the position of energy levels and hence their associated emission energy can vary with regards to the bond lengths in the structure.

1.3.8 Zinc sulfide band gap

Linear combinations of atomic orbitals (LCAO) and pseudo-potentials are used for the calculation of physical parameters in solids²⁷. This method is used for the calculation of the band gap of many materials including zinc sulfide²⁸.

The calculation of the electronic states and their positions within the band gap of a semiconductor requires knowledge of the position of the upper part of the valence band (E_v) and the bottom of the conduction band (E_c); Harrison²⁹ has produced a mathematical model (equations 1.5-8) to calculate these values:

$$E_{relax} = \frac{U(\varepsilon - 1)}{2\varepsilon} \quad (1.5)$$

Where E_{relax} is the relaxation energy, ε is the dielectric constant and U is the inter-atomic coulomb repulsion.

$$V_2 = \frac{\eta\hbar}{md^2} \quad (1.6)$$

V_2 is the covalent bond energy, η is the equal to 2.16, \hbar is Planck's constant and m is electron mass, d is distance.

$$V_3 = \frac{\varepsilon_p^c - \varepsilon_p^a}{2} \quad (1.7)$$

$$V_1 = \frac{v_1^a - v_1^c}{2} = \frac{\varepsilon_p^a - \varepsilon_s^a - \varepsilon_p^c - \varepsilon_s^c}{8} \quad (1.8)$$

V_3 is the ionic bond energy, V_1 is the metallic bond energy, $\varepsilon_s^a, \varepsilon_s^c$ are the atomic terms for anionic and cationic S -states³⁰. The atomic terms of the anionic and cationic p -states are $\varepsilon_p^a, \varepsilon_p^c$, respectively.

Using equation 2.8, E_c and E_v can be measured as follows³¹.

$$E_c = \frac{\varepsilon_p^c + \varepsilon_p^a}{2} + \frac{U}{2} \quad (1.9)$$

$$E_v = \frac{\varepsilon_p^c + \varepsilon_p^a}{2} - \sqrt{V_2^2 + V_3^2} + 1.1V_1 + E_{relax} \quad (1.10)$$

The band gap of the zinc sulfide can be measured using the following expression:

$$E_g = E_c - E_v \quad (1.11)$$

Figure 1.5 demonstrates how these calculations are carried out using the LCAO method.

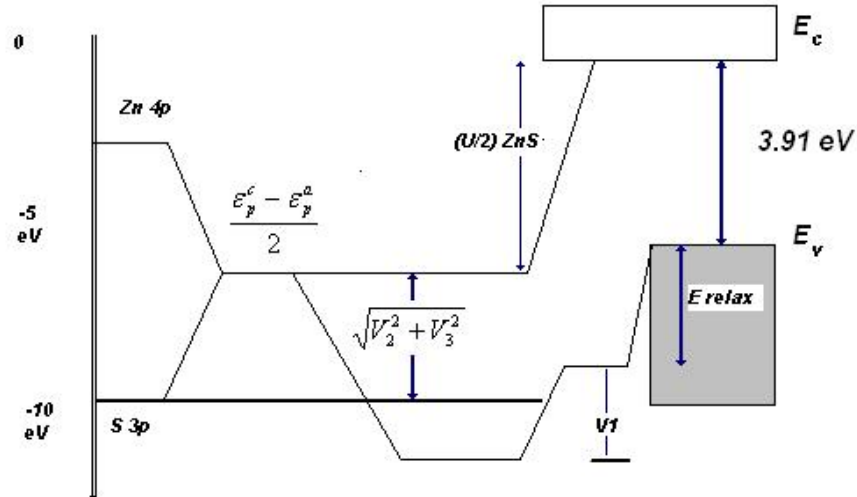


Figure 1.5: Calculation of the energy bands in zinc sulfide from the atomic p-orbitals using the LCAO method³¹.

Savchenko³¹ has produced a simulation of the electronic states of ZnS, ZnS:Cl, ZnS:Cu and ZnS:Cu,Cl phosphors (Figure 1.6). Electronic states with energies E1 and E2 correspond to Zn 4p and Zn sp³ orbitals. The E3 energy levels are formed by the 4p orbital bonding of the Zn-Zn bond. The non-bonding p-bands form the E4 energy level and hybridization state of copper sp³ orbital forms the E5 energy level. It is believed that Cl atoms compensate the Zn sp³ electronic states and thus the red emission band in these phosphors fades out³².

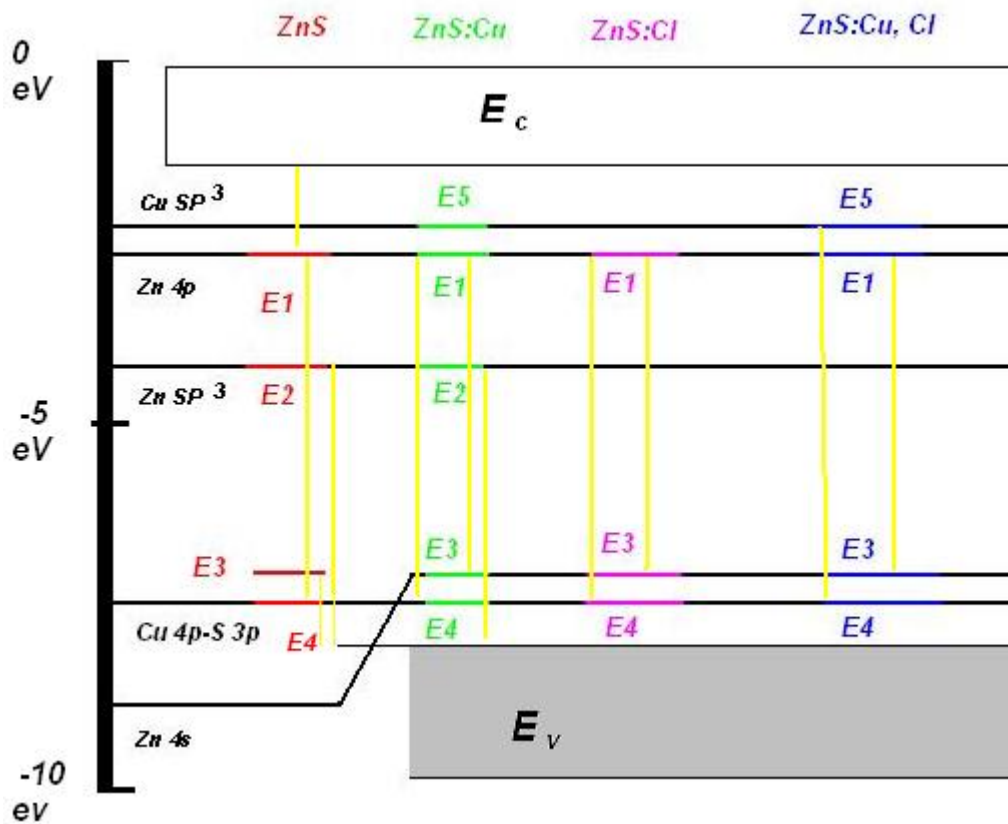


Figure 1.6: Simulation of the electronic states in ZnS, ZnS:Cl, ZnS:Cu and ZnS:Cu,Cl. The yellow arrows in this diagram show the possible optical radiative transitions. Experimental values obtained for these energy levels match very closely to the predictions of the above diagram.

1.4 Electroluminescence

The emission of light from certain materials under an electric field is known as electroluminescence (EL). In principle it involves the direct conversion of electrical energy into electromagnetic radiation. In comparison to the process of incandescence (in which light emission is determined by the heat generated), the cold emission of electroluminescent materials is directly related to the chemical and physical properties of its constituent material(s). This indicates that the emission from an electroluminescent material can be manipulated by altering its chemical and physical properties and hence a way of investigating the mechanism of the process and developing it more efficiently.

1.4.1 Concept of electroluminescence

The first observation of powder phosphors were reported by Destriau whilst examining electro-photoluminescence materials and most of the studies carried out on electroluminescent zinc sulfide (doped with copper) were conducted prior to the 1970's with pioneering work being carried out by Destriau³³.

The phosphor particles were embedded in an insulating matrix sandwiched between two flat electrodes and alternating field was applied to the specimen. Various materials such as sulfides, tungstates, germanates and silicates were then tested by Destriau, where field strengths of $\sim 10^5 \text{ V cm}^{-1}$ were applied and EL behaviour was observed³⁴.

1.4.2 Types of electroluminescence

The process of inorganic electroluminescence (EL) is defined as a process by which electromagnetic radiation is produced due the application of an electric field to crystalline semiconductor materials. The electroluminescence of inorganic semiconductors is classified into two groups: injection EL and high field EL (Figure 1.7)³⁴.

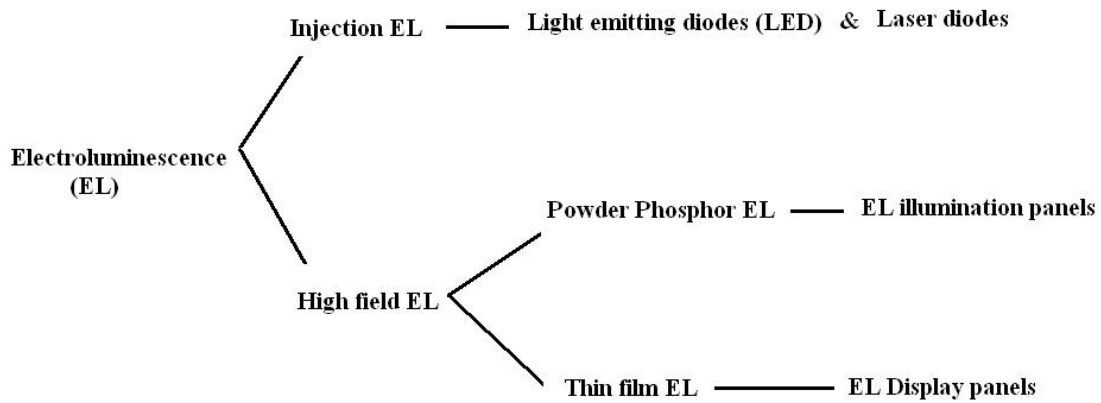


Figure 1.7: Types of electroluminescence mechanism and related applications.

1.4.2.1 Injection EL

In a p-n junction (positive-negative junction) at thermal equilibrium, a depletion layer is formed and a diffusion potential (V_d) is created across the junction. Upon application of a forward bias electric potential (V) across the junction, the diffusion potential decreases ($V_d - V$). This forces the injection of electrons from the negative region (n) to the positive region (p). This process is parallel to the migration of holes (positively charged) from the (p) to (n) states. Upon recombination of the electrons and holes electromagnetic radiation

with energy related to the energy gap of the junction are emitted; this process of light emission is termed injection EL (Figure 1.8)²⁰.

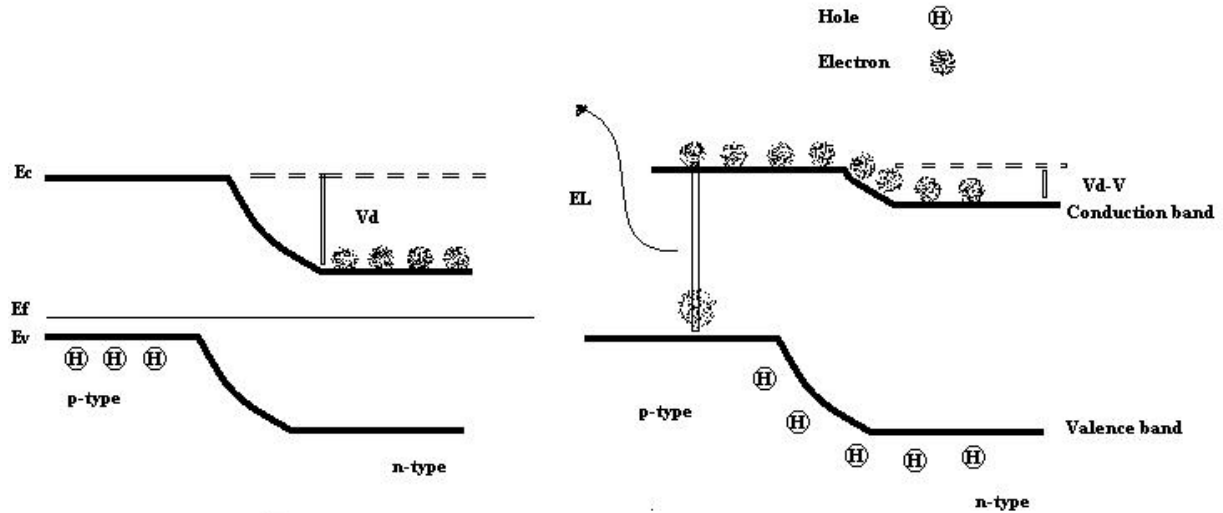


Figure 1.8: Injection EL, electron and hole interaction within the band gap confinement and light emission²⁰.

1.4.2.2 High field EL

High field EL involves application of high electric fields in the region of 10^6 V cm^{-1} to the electroluminescent material. Some of the electrons in the material reach energy levels sufficient to cause impact excitation of the luminescent centres present in the EL material. The electrons with sufficiently high energy are defined as the carriers. The high field EL can be described as carrier injection followed by the distribution of the carriers toward activation of the luminescent centres³⁶.

1.4.3 Carrier injection

Various theoretical models have been proposed for the injection of the carriers⁴¹. The carrier injection for powder EL material and thin films is thought to be similar but slightly different considering that in thin film EL the phosphor is a continuous layer of ZnS:Cu compared to the powder ZnS:Cu material being dispersed in a binder^v. The overall concept of these mechanisms states that electrons are injected into the semiconductor EL material, hence activating the luminescent centres³⁶.

1.4.4 Schottky barrier injection

Upon contact between metal and semiconductor, a barrier is formed known as the Schottky barrier³⁵ at the contact site. Considering a vacuum instead of the semiconductor, the work function is the minimum energy required to move an electron into a vacuum from its location within the Fermi energy levels. Considering an electron at a distance A from a metal (Figure 1.9), a positive charge is induced on the metal surface. The attractive force between the electron and the induced positive charge is equivalent to an attractive force between the electron and a positive charge mirror to the location of the electron i.e. distance A , this force is called the image force (F) with an associated potential energy as shown in Figure 1.9.

^v The thickness of the thin film can be as low as 2 microns while powder made panel constitute particles as large as ~30 microns dispersed in a dielectric binder. Hence thin films are activated at extremely high electric fields comparatively.

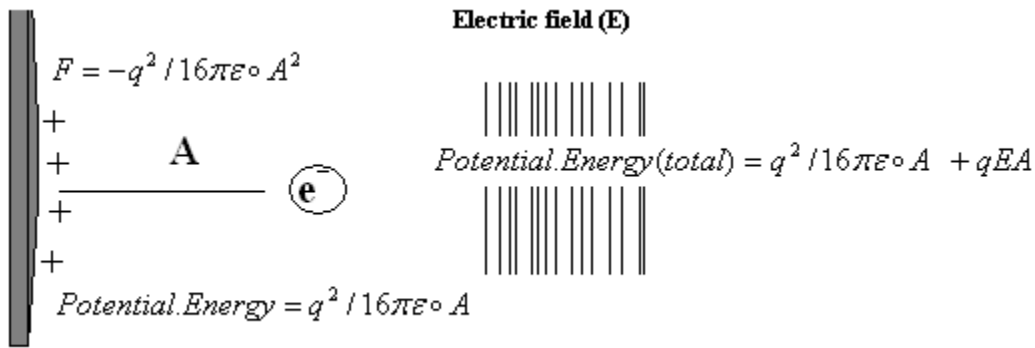


Figure 1.9: The force imposed on an electron by an electric field.

An external electric field reduces the total potential energy, which in turn lowers the effective metal work function. This decrease in the potential barrier is termed the Schottky effect. When the contact between a metal and a semiconductor is exposed to an electric field, the Schottky effect causes a decrease in the potential energy of the semiconductor and hence lowers the barrier³⁶. As a result the electron can be thermally injected into the semiconductor and excite the luminescent centres. In the case of powder ZnS:Cu EL phosphors, the semiconductor zinc sulfide and the copper impurity are thought to form a Schottky barrier³⁵. Lattice defects induce trapping of electrons in localised states of large band gap semiconductors³⁶. Upon application of an electric field, the trapped electrons are excited to the conduction band. The excited electrons can stimulate the luminescent centres to luminesce. This process is referred to as Poole-Frenkel emission. Upon application of high electric fields to Schottky barriers or electron traps the barrier becomes thin, hence promoting the tunnelling of the electrons into the conduction band³⁶. The current density of electrons via this route is only dependent on

the electric field. When electrons of a semiconductor are in thermal equilibrium, there is zero exchange energy between electrons and the lattice.

The energy distribution of electrons under thermal equilibrium is expressed by the Maxwell-Boltzman distribution function as:

$$\varepsilon = \frac{mv^2}{2} \quad (1.12)$$

Under the influence of an electric field, the electrons are provided with extra energy from the field and lose it to the lattice via phonons. The electrons move in the direction of the field by a drift velocity (v_d). Under this condition the Maxwell-Boltzamn distribution is altered to:

$$\varepsilon = \frac{m(v-v_d)^2}{2} \quad (1.13)$$

Moderate electric fields (less than 10^4 V cm^{-1}) generate electrons which lose their energy in the form of emitting phonons. When the electric field is increased above values of 10^5 V cm^{-1} the electrons gain sufficient energy to excite the luminescent centres via impact excitation³⁷.

More recent investigations have proposed two models for the transport of the energised electrons within the zinc sulfide crystal lattice; one regards the electron motion within the lattice to have ballistic characteristics whilst the other explains the transport of the

electron in the form of collision and field dependent-drift leading to a higher probability of electron-acceptor collisions³⁸.

1.4.5 Luminescence centre excitation mechanisms

Fields in the region of 20^6 V cm^{-1} are sufficient to generate hot electrons within the zinc sulfide lattice. Upon collisions within the lattice these energised electrons tend to ionise the whole matrix in which they collide and hence generate an ionised zinc sulfide lattice. The ionisation of the lattice implies the generation of electron-hole pairs. If impurities exist within the lattice (the doping element), upon ionisation, they tend to facilitate electron and hole recombination, leading to radiation of light³⁹. Direct impact ionisation of the luminescent centres can also occur by the collision of the electrons with the ion impurity, for example Mn^{2+} or Cu^{2+} centres which are often doped into EL phosphors. The d shell of the doping element is excited via such an electron collision mechanism leading to light emission³⁹. In zinc sulfide powder phosphors, the luminescent centres result from the association of the Cl^{1-} and Cu^{2+} ions (referred to as a Cl-Cu centre) forming the donor-acceptor pairs within the lattice. The electron-hole recombination in these phosphors is thought to occur in these centres. Emission from these Cl-Cu centres is usually green. However, in the presence of Mn^{2+} ions within the ZnS:Cu,Cl phosphor, the energy from this excited centres can be transferred to the Mn^{2+} centre leading to yellow emission which is characteristic of Mn^{2+} phosphors³⁹. Figure 1.10 illustrates the excitation processes of the luminescent phosphors.

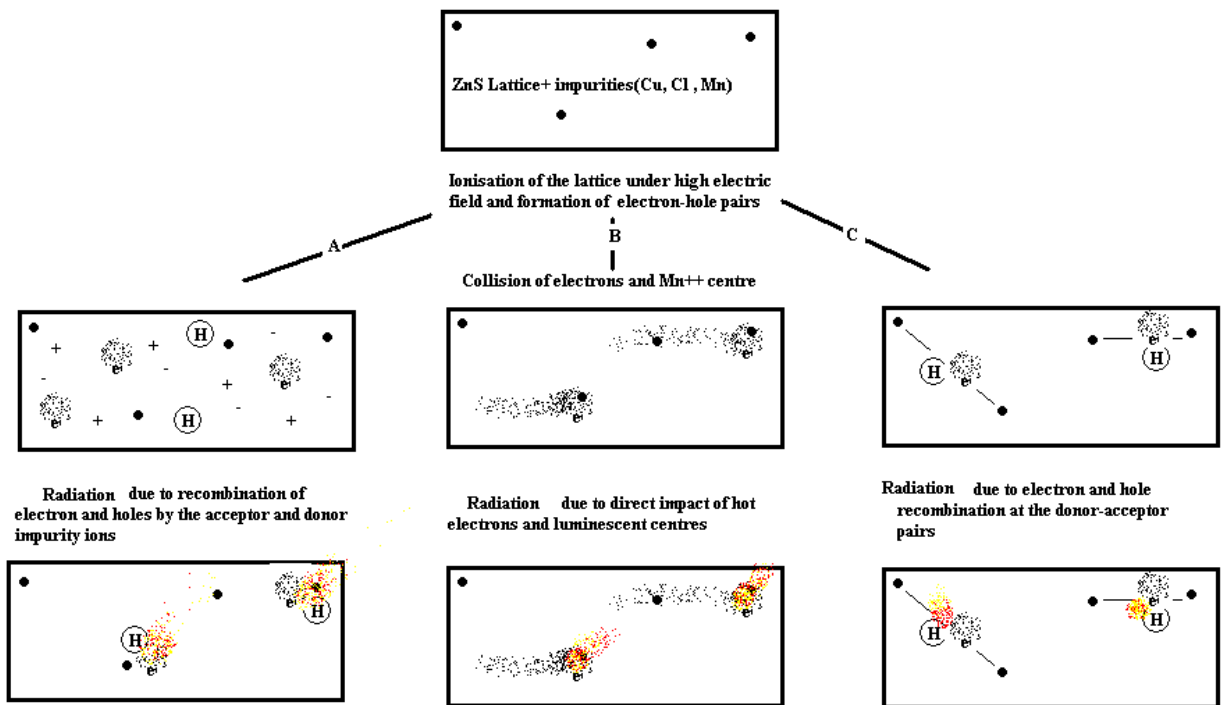


Figure 1.10: Different excitation mechanisms of luminescent centres (e^- : electron, H^+ : hole)³⁹.

1.5 Powder zinc sulfide phosphor electroluminescence

1.5.1 Alternating current (AC) powder EL

EL is observed when an electric field corresponding to an AC voltage is applied across the electrodes of a cell; a scheme which was originally designed and implemented by Destriau in the 1930's⁴⁰ (Figure 1.11).

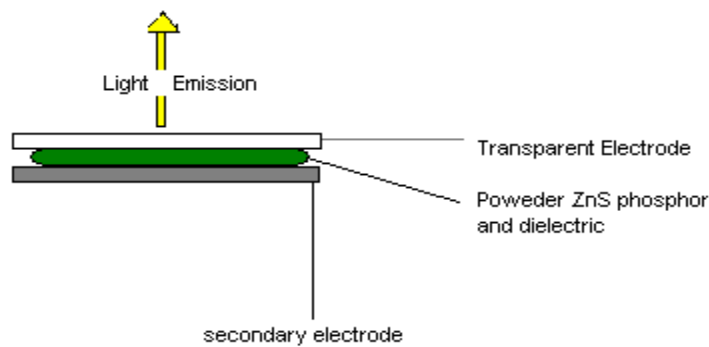


Figure 1.11: *The structure of the Destriau cell, a mixture of the EL phosphor and dielectric medium is placed between two electrodes; upon application of alternating current light is emitted from the phosphor layer.*

A phosphor material with particle sizes ranging from 5 to 40 μm is dispersed in a dielectric medium and sandwiched between two electrodes (Figure 1.11). The phosphor material is a zinc sulfide host with copper and other impurities in the region of $10^{-3} - 10^{-4}$ grams of copper to one gram zinc sulfide. The dielectric material in which the phosphor is dispersed has to possess a high dielectric constant. Under high potential difference, the structure is protected from dielectric breakdown by coating one of the electrodes with a piezoelectric insulator such as BaTiO_3 .

The magnitude of the applied voltage can be in the region of 50-200 V which would correspond to an electric field of about 10^5 V cm^{-1} across the phosphor. The relationship between the voltage and brightness is expressed by equation 1.14 where B is the brightness, V is the voltage, B_0 and b are constants which depend on the particle size of the phosphor, concentration and the dielectric constant of the medium⁴¹.

$$B = B_0 \exp(-b/V^{0.5}) \quad (1.14)$$

It has been shown that the presence of Cu^{2+} ions is absolutely essential for the AC electroluminescence process while the presence of the Cl^{-} ions is essential for brightness; the efficiency of the phosphor is increased by increasing the particle size and the operational life time of the phosphor has been reported to decrease in relation to particle size⁴².

During the 1960s a great deal of research was carried out by Fischer to elucidate a theoretical explanation for the mechanism of the ACEL process. During these studies optical observations of $\text{ZnS}:\text{Cu},\text{Cl}$ particles were made under a light microscope⁴³. Single particles were investigated and it was observed that light emitting regions within the particle took the form of “twinkling tails of a comet”. Investigations by Fischer showed that each half of the double comet lines lit up alternately when the nearest electrode turned positive⁴⁴ (Figure 1.12).

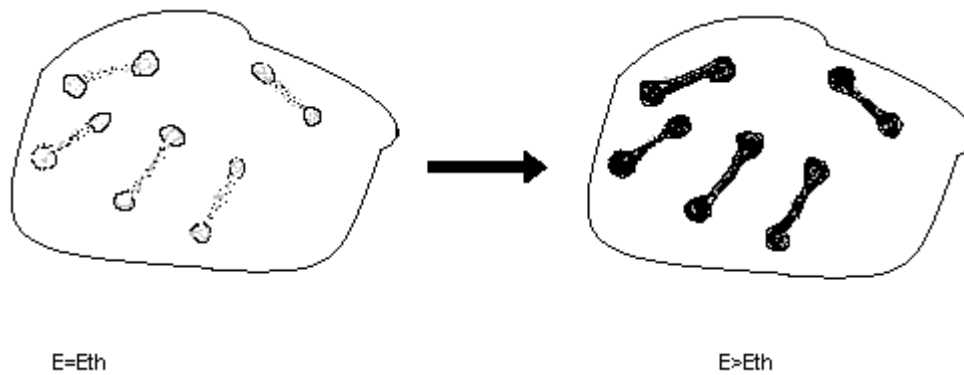


Figure 1.12: Electroluminescence from ZnS:Cu,Cl particles. The double comet lines are illustrated at the threshold ($E=E_{th}$) voltage and above ($E>E_{th}$)⁴⁴.

Based on the aforementioned observations a band model explanation of the electroluminescence process was proposed by Fischer⁴⁵. Zinc sulfide crystal particles were prepared by firing amorphous zinc sulfide containing copper and aluminium impurities at temperatures exceeding 1000°C. Using X-ray powder diffraction, it has been shown that the wurtzite crystal phase dominates the structural state of the prepared crystals. After the firing process at 1000°C, the particles are cooled down, there is a transition to the cubic structure from the wurtzite crystal phase; during this structural transition the copper which is being used as an activator, resides on crystal sites where defects are formed due to the transition. These copper ions form thin Cu_2S needles in the zinc sulfide crystal lattice. Due to the p-type semiconductor properties of Cu_2S and n-type semiconductor properties of the zinc sulfide a Schottky barrier junction is formed⁴⁶.

When voltages above the threshold are applied, electrons and holes are tunnelled from each end of these needles into the zinc sulfide lattice as illustrated in Figure 1.13. This is

because applied fields of higher than 10^4 V cm^{-1} can induce local fields greater than 10^6 V cm^{-1} in the lattice⁴⁷.

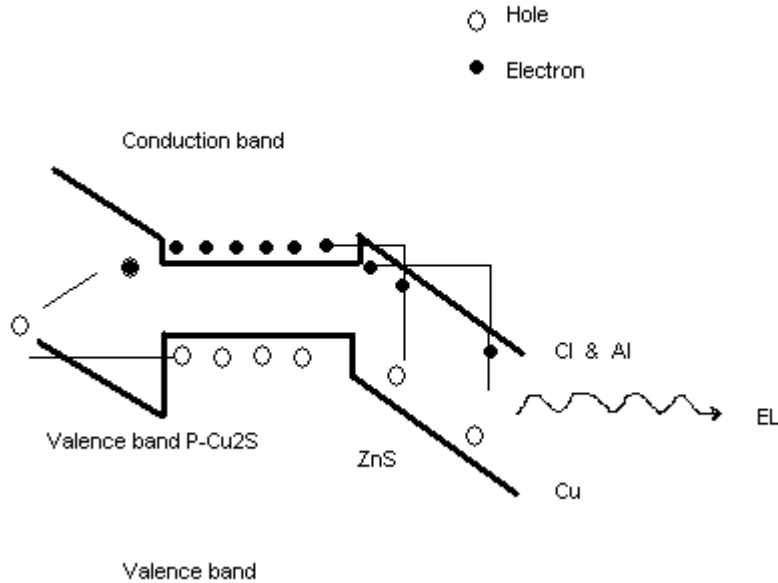


Figure 1.13: Injection of electrons and holes from opposite ends of a Cu_2S needle into the $\text{ZnS}:\text{Cu},\text{Cl}$ surrounding lattice⁴⁷.

In this system the electrons reside in the shallow traps of Cl^{1-} , while holes are concentrated on the Cu^{2+} ions which act as the recombination centres. Reverse bias of the field recombines the electrons and holes and hence light emission occurs. The Fowler-Nordheim equation (1.15) is an expression of the current flow (I) through the CuS-ZnS contact⁴⁸. In this equation E is the field strength and W is the work function related to the energy difference between electron affinity of zinc sulfide and copper sulfide, B & A are constants.

$$I = A \frac{E^2}{W^{3/2}} \exp\left(-B \frac{W^{3/2}}{E}\right) \quad (1.15)$$

Transmission electron microscope analysis of ZnS:Cu phosphor particles has shown dark patches with diameters of ~30 nm on twin boundaries of the ZnS:Cu crystals⁴⁹. X-ray analysis of these dark patches indicated the presence of monovalent copper ions, most likely Cu_2S . It was postulated that the Cu_2S structures are the copper needles, mentioned earlier, along the micro twin boundaries. It is hypothesized that the reasons for of the AC powder EL luminescence decay over time in relation to their light output efficiency decreases over time⁵² at different rates depending on the frequency of the power source is due to degradation of these copper needles along with the degradation of the structure of the phosphor material as a result of ambient conditions and the conditions under which the phosphor is used. The EL activation by copper needle theory is extensively studied using x-ray absorption spectroscopy by various researchers⁵⁰ however as yet the theory can still be debated⁵¹.

The luminescence decay has also been shown to be directly related to the driving frequency at which the EL device is operated⁵². Equation 1.16 illustrates this relationship, where α is a constant proportional to the driving frequency, L is luminance output, L_0 is light output at time 0 in ‘lumens’ and t is time in hours.

$$L/L_0 = (1 + \alpha.t)^{-1} \quad (1.16)$$

1.5.2 Ferroelectric materials used in electroluminescent panels

An electroluminescent panel is comprised of the phosphor layer sandwiched between two flat electrodes one of which is transparent (e.g. ITO coated plastic or glass). One of the major components used in the construction of these electroluminescent panels is the ferroelectric material used between the non-transparent electrode and the phosphor layer. The presence of this material is critical if the EL device is to be kept safe from electric field breakdown. The permanent electric dipole moment of certain polar materials can be reoriented by the application of an electric field. Such crystals are called ferroelectric. All ferroelectric crystals are necessarily both pyroelectric^{vi} and piezoelectric^{vii}. The temperature at which these materials lose their polar properties is called the Curie temperature (T_c). Exposure to an electric field under appropriate conditions can result in complete or partial realignment of the spontaneous polarization⁵³. A net dipole moment is not normally detectable in such materials because the surface charges are rapidly neutralized by ambient charged particles, hence the importance of the presence of these materials adjacent to the phosphor materials in electroluminescent devices can be appreciated.

A crystal is ferroelectric if it has a spontaneous polarization, P_s , which can be reversed in sense or reoriented by the application of an electric field larger than the coercive^{viii} field.

^{vi} *Pyroelectricity (from the Greek pyr, fire, and electricity) is the ability of certain materials to generate a temporary voltage when they are heated or cooled. The change in temperature slightly modifies the positions of the atoms within the crystal structure, such that the polarization of the material changes. This polarization change gives rise to a voltage across the crystal.*

^{vii} *Piezoelectricity is the ability of some materials to generate an electric field or electric potential in response to an applied mechanical strain.*

^{viii} *The coercive field of a material is the intensity of the applied magnetic field required to reduce the magnetization of that material to zero after the magnetization of the sample has been driven to saturation.*

Reversal is also known as switching. Crystalline properties (such as the defect distribution and conductivity, together with temperature, pressure, and electrode conditions) may effect the ferroelectric reversal. Most ferroelectrics have a characteristic value of P_s and T_c . Ferroelectric materials may be divided into three classes on the basis of the nature of the displacement vectors, Δ_I , that produce a reversal or reorientation of P_s . The one-dimensional class involves atomic displacements, all of which are parallel to the polar axis, as in the case of tetragonal BaTiO_3 ; in this class, $P_s > 25 \times 10^{-2} \text{ C m}^{-2}$. The two-dimensional class involves atomic displacements in a plane containing the polar axis: a typical example is BaCoF_4 ; this class has values of P_s between 10×10^{-2} and $3 \times 10^{-2} \text{ C m}^{-2}$. The three-dimensional class involves atomic displacements of similar magnitude in all three dimensions⁵⁴; a typical example is $\text{Tb}_2(\text{MoO}_4)_3$ where $P_s < 5 \times 10^{-2} \text{ C m}^{-2}$.

1.6 ACEL and its current status

The original apex of research, development and applications of ACEL was between 1950 and 1963, but were then soon left behind by the emerging thin film techniques or DC variants. However a second thrust occurred after the development of more efficient phosphors around 1990, and thus powder-based thick-film ACEL is still present in the market, since it is the only mature technology for flat and flexible large area light sources (figure 1.14). Durability and light output of AC-electroluminescent foil lamps have made tremendous advances, mostly due to improvements in the luminescent materials used²⁰. These products are still based - more or less exclusively - on zinc sulfide, although a lot of effort has been invested into broadening the pool of potential materials. Full theoretical

understanding of the underlying physics is still absent; development of phosphors, therefore, is still based on trial and error approaches²⁰. Nevertheless, thick-film (powder) ACEL in foil lamps is now applied for back-lighting of LCD displays or mobile phone keyboards, in automotive dashboards, for indoor illumination at modest light levels (e.g., luminescent tiles), safety installations, advertising purposes or decoration, albeit mostly under conditions with low ambient light influx^{50,51}, figure 1.14.



Figure 1.14: ACEL panels are the only flexible light emitting panels available, specially where low ambient lighting is present they are a fantastic solution to decorative & information display ideas, Jaguar use Electroluminescent products to light the interior of their C-X75 Concept Car^{ix}.

^{ix} Jaguar Cars Ltd, Project: C-X75: 2012.

1.7 DC powder EL

The structure of a DC powder EL is indeed very similar to that of the ACEL device with a thinner layer of phosphor; however, the polarity of the electrodes is important so that the ITO coated glass has to be the anode and the vapour coated aluminium back electrode is the cathode. The phosphor preparation of the DC powder EL is different from that of AC powder EL. Unlike ACEL powder phosphors, where zinc sulfide doped with copper is fired, the DCEL phosphors are prepared by immersion of doped ZnS:Mn phosphors in hot $CuSO_4$ solution followed by “forming” of the device. “Forming” is a process by which the device is conditioned so that during the application of a voltage, electrons are accelerated and bombard the Mn^{2+} centres emitting yellow-orange colour. Figure (1.15) illustrates the “forming” procedure.

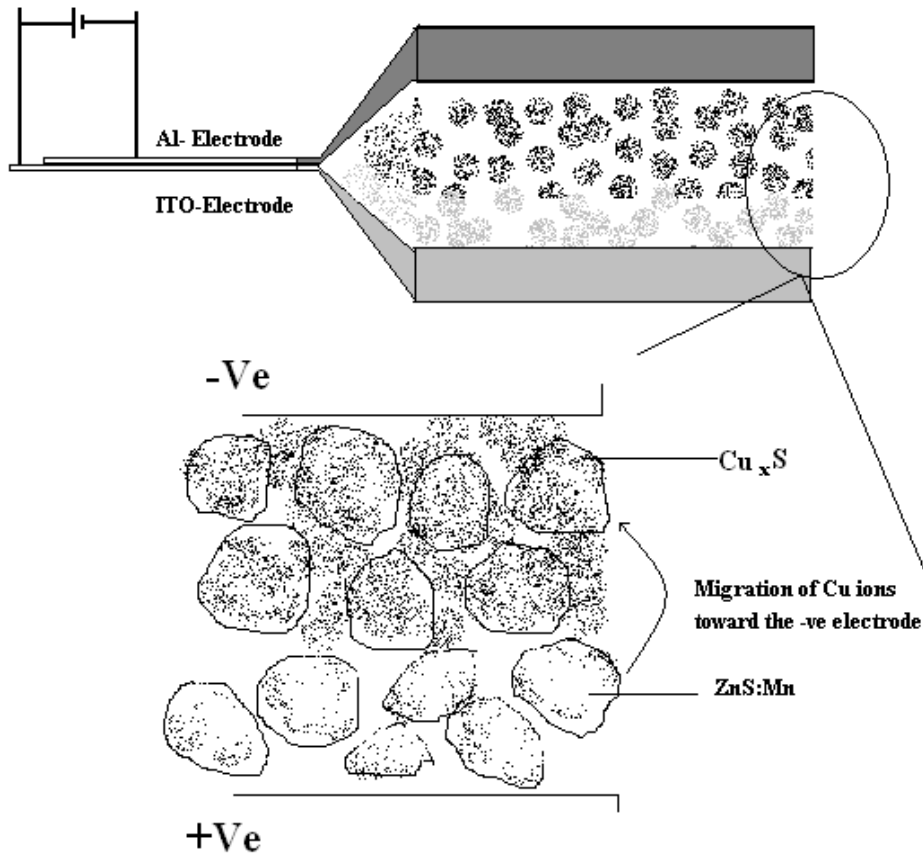


Figure 1.15: Structure of a DCEL device⁵⁵.

The conventional DCEL panels made using ZnS:Mn phosphors emit light in the yellow region of the spectrum. However, use of other doping materials (such as the alkaline earth sulfides and rare-earth elements) can produce various colours from blue to red⁵⁵.

1.8 Overview of other display technologies

A variety of display technologies exist that are used in modern day life. The television system, personal computers, laptops, advertising boards, hospital displays and many other commercial pieces of equipment all take advantage of display technology.

1.8.1 Cathode ray tubes (CRTs)

The cathode ray tube was invented by Karl Ferdinand Braun in 1897. Its primary use involved the display of electrical signals. However, it was later revolutionised by the work of Zworykin⁵⁶ and Farnsworth⁵⁷ to become what is now known as the CRT television. Beams of electrons bombarded a glass screen displaying emission of light in blue, green and red. Many of the CRT televisions, computers, video game machines, monitors and radar displays were based on cathode-ray tube technology. The drawback with this technology is the size and weight associated with the structure of the cathode ray tube and its high energy demand and hence it is gradually eliminated from the market.

1.8.2 Liquid crystal displays (LCD)

A group of molecules can exist in a state of matter where they can be regarded both as solid and liquid; they are not as ordered as solids yet possess some degree of alignment. Because of this property, these materials are referred to as liquid crystals; matter which is anisotropic in some of its properties while demonstrating fluid like properties. They were discovered by Reinitzer & Lehmann⁵⁸ and investigation of their commercial applications, mainly at the Sharp Corporation, dates back to the late 1960's⁵⁹. A great deal of research has been carried out on these materials ever since, gradually making them a rival to the cathode ray tube technology. The fundamental basis of this technology is the controlled transmission of certain wavelengths of light while filtering out the other wavelengths. Controlling this function of the crystals is carried out by electronic hardware which operates the system. Extensive research has been involved in optimising this technology,

e.g. mobile phone screens, laptops and many present television units are based on LCD technology.

1.8.3 Field emission displays (FEDs)

Field emission displays can offer superior quality images if used as a screen display technology. Their structure is simply based on an anode which is incorporated within a phosphor layer and fixed cathode tips stabilising the structure sandwiching the phosphor between the anode and cathode. Tunnelling of electrons between the cathode and anode excites the phosphor, and light is emitted⁵. This means that they will emit colour with the quality matching the CRT while their weight and size is competitive with LCDs⁶⁰. Unfortunately due to the vast quantities of money invested in LCD and plasma displays it is unlikely that this technology will be adopted in the foreseeable future.

1.9 Project objectives

The overall aims of this research involve:

- (i) Studies of the diffusion of copper atoms into the zinc sulfide crystal lattice during the firing procedure and crystal particle formation,
- (ii) A more in depth understanding of phosphor degradation under high AC drive frequency,
- (iii) Investigation of the factors involved in the synthesis of phosphors which may lead to an improvement in luminescence efficiency, and
- (iv) Mapping the distribution of doping copper over the phosphor particles.

Chapter 2 : Experimental techniques

A description of the instruments used in this study is presented in this chapter. These techniques are: preparation of ACEL panels, scanning electron microscopy (SEM), x-ray powder diffraction (XRPD), synchrotron x-ray diffraction at the Diamond synchrotron, extended x-ray absorption fine structure (EXAFS) at the Berlin's Bessy synchrotron, energy dispersive analysis with x-rays (EDAX), inductively coupled plasma mass spectrometer (ICP-MS), laser scattering particle size analyser, Jeti specboss radio-spectrometer and AC drive source. Each of these techniques were used to gather extensive information on the zinc sulfide phosphor particles, such as surface imaging, crystal structure, crystal size, emission properties and constitutional analysis.

2.1 ACEL Panel preparation using powder zinc sulfide

The ACEL panel is a simple set up of phosphor and dielectric material sandwiched between two electrodes one of them being transparent to allow the emission of light. The electric field across the electrodes is the driving force behind the process of electroluminescence and hence understanding the interaction of the field with the phosphor and dielectric particles would provide valuable knowledge which may lead to the fundamental understanding of the process at the atomic level. As previously explained the ACEL panel is very simple in structure, a layer of phosphor material mixed with a medium sandwiched between two conducting sheets one of which is transparent to allow the emitted light to escape and the other coated with a dielectric material to allow attainment of higher electric fields across the two plates. In industry, the phosphor and dielectric material are screen printed, which consequently allows production of standard

panels on a large scale; this also requires using very high quantities of materials. However, during this research, since the samples were prepared on a small scale, smaller quantities of samples were available and also to conserve time a simpler approach was used for the preparation of the panels. Two ITO coated glass pieces were used, one of which was coated with commercial dielectric material derived from barium titanate. The phosphor materials were then mixed with linseed oil in a ratio of 4(phosphor):1(oil) of total weight. All samples prepared for analysis were made using the 4:1 ratio, unless stated otherwise. The small amount of the phosphor/oil mixture ($\sim 15\mu\text{L}$) was then sandwiched between the two ITO coated glass units. Figure 2.1 shows the structure of the panel.

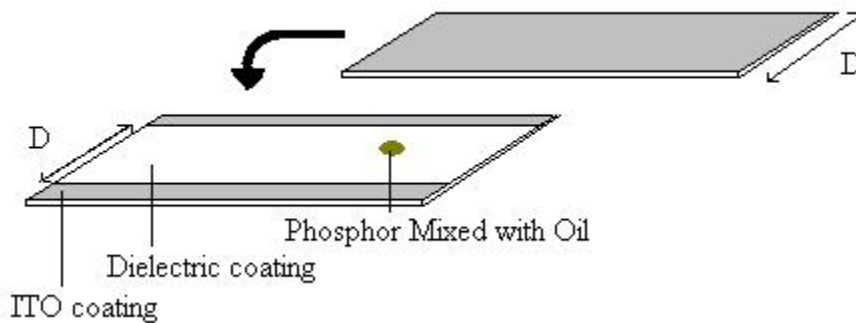


Figure 2.1: Demonstration of the ACEL panel structure.

2.2 Analysis Study of phosphor to medium ratio in ACEL panel preparation

A series of tests were carried out using uncoated ACEL phosphors manufactured by Sylvania. These materials were used for a variety of panel studies.

As all of the samples prepared for the panel making during this research were made using a mixture of phosphor and linseed oil (binder), these tests were carried out to find the optimum concentration of the phosphor required in the binder to investigate the relationship between this concentration and optimum emission intensity. A series of samples were prepared using various phosphors to medium binder ratio and used in a panel with a 12 μm spacer between the two plates. The 12 μm spacer was used to allow the use of higher amounts of phosphor compared to the usual structure which did not include a spacer to fulfil the aims of this experiment. To ensure that the ratio of the phosphor and medium were accurate the whole mixing procedure was carried out on the panel itself. The samples were then tested using 207 volts and 400 Hz frequency alternating current sinusoidal power source.

The procedures for the preparation of these samples and the ACEL emission efficiency of these samples are presented in Table 2.1 and Figure 2.2. Since the 81% phosphor to medium binder ratio gives the optimum results, this ratio was used for preparation of all the samples during this work.

Test sample	Medium (g) (linseed oil)	Phosphor (g) Sylvania Uncoated	%[Phosphor]	Emission luminance (cd/m ²)
1	0.0070	0.0017	19.54	7.08E+00
2	0.0090	0.0025	21.73	1.03E+01
3	0.0068	0.0034	33.33	2.57E+01
4	0.0085	0.0044	34.10	2.90E+01
5	0.0068	0.0068	50.00	4.27E+01
6	0.0065	0.0110	62.85	6.60E+01
7	0.0081	0.0270	76.92	9.83E+01
8	0.0074	0.0327	81.54	1.10E+02
9	0.0088	0.0433	83.10	1.07E+02
10	0.0088	0.0490	86.26	1.02E+02

Table 2.1: Various phosphor to oil ratio's for preparation of the ACEL panel and the panel luminance of the combination (based on average of five samples).

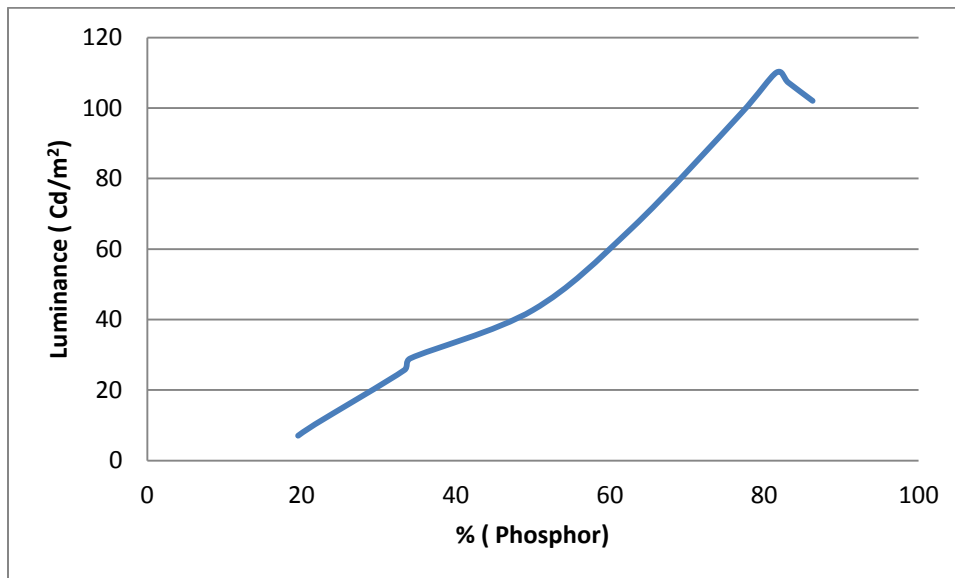


Figure 2.2: Effect of phosphor to medium binder ratio on the emission of the ACEL panel. The ratio of 80% phosphor powder to medium is the optimum ration after which the luminance of the material will tend to decrease.

2.3 Scanning electron microscopy (SEM)

The scanning electron microscope is designed for surface analysis and imaging of materials. This instrument utilises a beam of electrons as an electron probe that is scanned in a regular manner over the surface of the sample to be analysed. The electron beam, upon collision with the sample, stimulates the generation of secondary electrons from the surface of the specimen which, via a network of electronic hardware, is amplified and converted to a three dimensional image. This image resembles the pattern of the scattered secondary electrons and hence resembles the surface from which they have arisen. In this study SEM was utilised to obtain surface images of all the materials which were synthesised or tested in this study⁶¹.

2.4 X-ray powder diffraction (XRD)

X-ray powder diffraction is an instrumental technique which is used to identify minerals as well as other crystalline materials. XRD has provided scientists with a fast and reliable tool for mineral identification. It is particularly useful for identifying powder specimens. XRD can be used for evaluating anisotropic crystal features and to determine the proportion of different crystal structures present. Possible deviation of materials from their usual crystallographic composition, degree of crystallinity and degree of hydration of minerals that may contain water in their structure can all be identified by XRD⁶¹. However, it is difficult to obtain topological data by XRD and other instruments such as SEM are used for this purpose.

In an XRD instrument, the diffracted x-rays from the sample are detected by a detector and the signal is then electronically converted to count rates. When the angle between the x-ray source, sample and the detector is changed in a controlled range an x-ray pattern is produced.

Bragg's law is used to measure the distance between the planes of atoms in the sample.

Bragg's law can be expressed as:

$$n\lambda = 2d \sin \theta \quad (2.1)$$

where n is an integer, λ is the wavelength of incident x-rays, d is the distance between adjacent planes of atoms (d -spacing) and θ is the angle of incidence of the x-ray beam. Since the wavelength and the incident angle are known, Bragg's law can be used to calculate the d -spacing⁶². Characteristics of the generated d -spacing in an X-ray scan provides a unique fingerprint of the material present in the sample which, when compared to standard scans, can help in identifying the constituent/s of the sample. Table 2.2 illustrates various applications of this technique.

Diffraction Line parameter	Applications
Peak position	Unit cell parameter refinement Space group determination Phase identification
Intensity	Phase abundance Reaction kinetics Phase identification Preferred orientation
Width and shape	Instrumental resolution function Microstructure, crystal size, size distribution, lattice distortion, structure mistakes and dislocations

Table 2.2: Applications of X-ray powder diffraction. (Source: Max Planck institute for Metals research, Stuttgart, Germany).

2.5 Synchrotron X-ray analysis & extended X-ray absorption fine structure (EXAFS)

Extended X-Ray Absorption Fine Structure (EXAFS) is the measurement of the x-ray absorption coefficient, μ , (equations 2.2 and 2.3) in a material as a function of energy. The sample is exposed to X-rays of a narrow energy resolution; the incident and transmitted x-ray intensity is recorded as the incident x-ray energy is incremented⁶². The number of x-rays that are transmitted through a sample (I_t) is equal to the number of x-rays interacting with the sample (I_0) multiplied by a decreasing exponential that depends on the type of atoms in the sample, absorption coefficient μ , and the thickness of the sample, x :

$$I_t = I_0 e^{-\mu x} \quad (2.2)$$

The absorption coefficient is obtained from the natural log of the ratio of the incident x-ray intensity to the transmitted x-ray intensity:

$$\mu = -\ln(I/I_0)/x \quad (2.3)$$

The number of x-rays absorbed by the sample increases dramatically when the incident x-ray energy matches the binding energy of an electron of an atom within the sample; this leads to a drop in the transmitted x-ray intensity. This results in a unique absorption edge corresponding to different binding energies of its electrons. Each element in the Periodic table has a set of absorption edges. The synchrotron provides highly penetrating x-rays.

EXAFS spectra are displayed as graphs of the absorption coefficient of a given material versus energy, typically in the 500 – 1000 eV range beginning before an absorption edge of an element in the sample. The x-ray absorption coefficient is usually normalized to unit step height. This is undertaken by regressing a line to the region before and after the absorption edge, subtracting the pre-edge line from the entire data set and dividing by the absorption step height, which is determined by the difference between the pre-edge and post-edge lines at the value of E_0 (corresponding to the absorption edge). X-ray absorption spectra are produced over the range of 200 – 35,000 eV. The dominant physical process is one where the absorbed photon ejects a core photoelectron from the absorbing atom, leaving behind a core hole. The atom with the core hole is now excited. The energy of the ejected photoelectron will be equal to that of the absorbed photon minus the binding energy of the initial core state. The ejected photoelectron interacts with

electrons in the surrounding non-excited atoms in form of wave reflection. If the ejected photoelectron is assumed to have a wave-like nature and the surrounding atoms are described as point scatterers, it is possible to imagine the backscattered electron waves interfering with the forward-propagating waves⁶². The resulting interference pattern shows up as a modulation of the measured absorption coefficient, thereby causing an oscillation in the EXAFS spectra. The wavelength of the photoelectron is dependent on the energy and phase of the backscattered wave which exists at the central atom. The wavelength changes as a function of the energy of the incoming photon. The phase and amplitude of the backscattered wave are dependent on the type of atom causing the backscattering and the distance of the backscattering atom from the central atom. The dependence of the scattering on atomic species makes it possible to obtain information pertaining to the chemical coordination environment of the original absorbing (centrally excited) atom by analyzing the EXAFS data⁶³.

For this research the Bessy II KMC2 facility at the Berlin synchrotron was used to analyse the samples. The specifics of the apparatus are as follows. The optical layout of the KMC-2 unit at Bessy II (Figure 2.3) has a vertical and a horizontal entrance slit from 0-10 mm cooled by water. It takes advantage of a double 2SiGe 111 graded crystal monochromator with angular range of 2.16° to 70° . The energy range is 4 -15 keV. The post monochromator of the apparatus is a Rh-coated cylinder mirror with bending mechanics. It provides fixed horizontal focus at 35 m from the source with variable vertical focus 31-36 m from the source. The vertical beam deviation is 0.5° above the horizontal plane. The beam line provides an experimental set-up for EXAFS and XANES measurements in either air or helium atmospheres in the energy range of 4 keV –15 keV.

Beam intensity is stabilized by MOSTAB electronics with an accuracy of 0.3 %⁶¹. The detector system consists of three ionisation chambers, a Si-PIN photodiode for fluorescence measurements, a scintillation counter and an energy-dispersive detector (Röntec X-Flash). An add-on microprobe capillary system with a spatial resolution of >5 μm is available for micro-EXAFS, micro-fluorescence and micro-diffraction experiments. For X-Ray diffractometry and reflectometry the experimental hutch is equipped with a 6-axis HUBER goniometer and a 2-dimensional cross-wire detector with a spatial resolution of 150 μm . A high-resolution X-ray CCD camera with a pixel size of 6.7 μm can be used for experiments alignment⁶⁴.

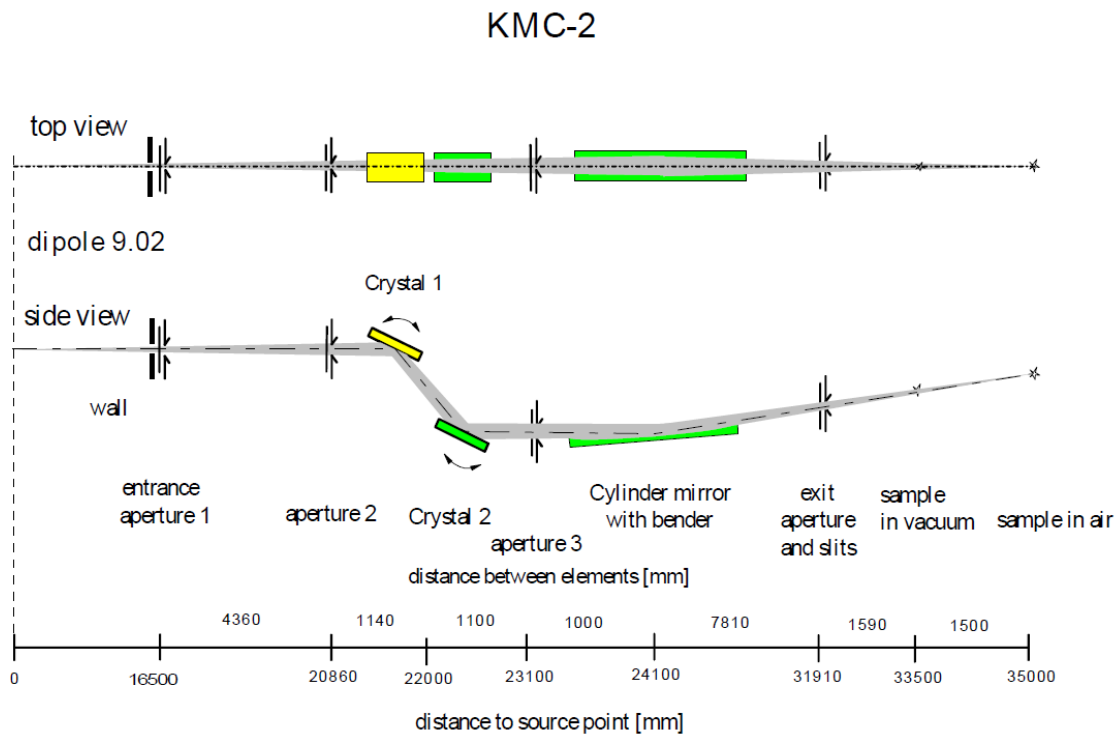


Figure 2.3 Optical layout of the KMC-2 unit at Bessy II⁶³.

2.6 Inductively coupled plasma mass spectrometry (ICP-MS)

Inductively coupled plasma mass spectrometry is an analytical technique which is usually used for the quantitative detection of trace metals in environmental samples; it is especially used for analysis of water for the presence of heavy metals. The core hardware of the ICP-MS, the torch, is a unit which generates gaseous argon in a highly ionised state called plasma^x. The temperature of this plasma can reach up to 8000°C. The basic structure of the torch is composed of an outer, middle and inner silicon tubes. The torch is situated within a water cooled radio frequency (r.f.) generator coil. The r.f. field is activated upon the flow of gaseous argon through the torch, producing an oscillating current in the induction coil that wraps around the tube. The induction coil produces an oscillating magnetic field that creates an oscillating current in the atoms of argon, ionising them and creating the plasma (Figure 2.4).

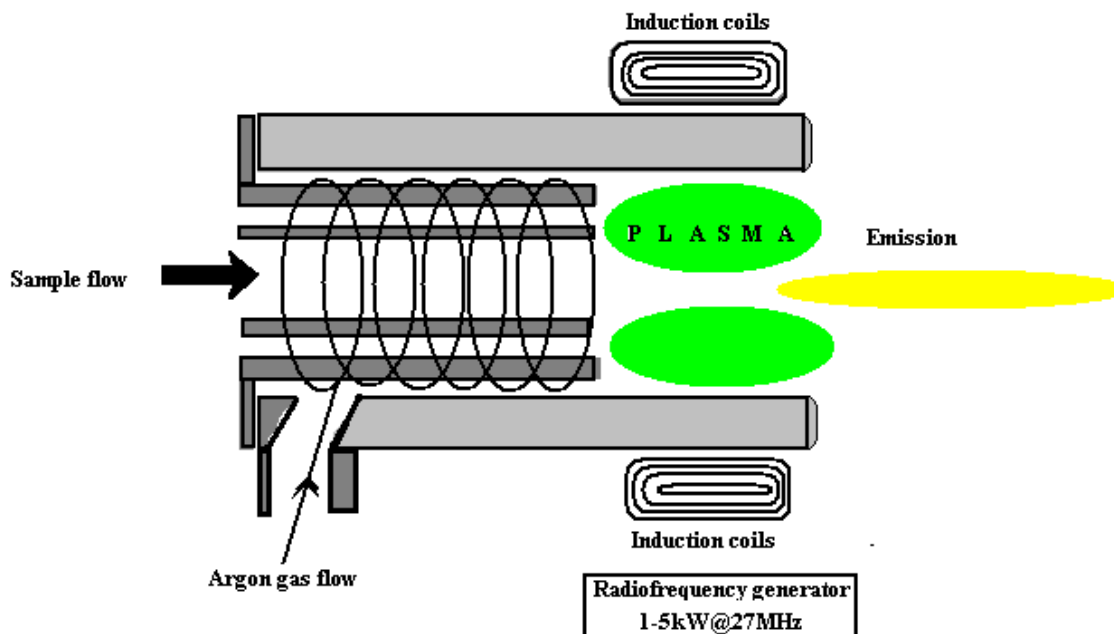


Figure 2.4: Plasma forming unit of the ICP-MS instrument.

^x Agilent Technologies. USA. Producer of atomic spectroscopy Instruments (<http://www.chem.agilent.com>)

A mass spectrometer is hyphenated with the ICP to form the ICP-MS apparatus and analyse the sample and generates the data relating to the atomic composition, hence identifying the metal atoms present with sensitivity in the ppm range⁶⁵.

2.7 Laser light scattering particle size analyser (HORIBA LS920)

Light scattering is the alternation of the direction and intensity of a light beam that strikes an object. Scattering can be considered as the total outcome of reflection, diffraction and refraction up on interaction of light and matter. Various models were proposed to explain the effect of particle size and shape on the scattering characteristics. A theory⁶⁶ was proposed by Gustav Mie in 1906 to formulate a relationship between particle geometry and scattering in any medium. The theory accurately predicts the angle and intensity of light scattered when it interacts with particle. However, there are certain constraints to this theory; some of the main constraints are that only monochromatic light is considered, the particle is isotropic and spherical, scattering and absorption are both considered and no quantum effects are considered.

This theory has proved to be of use in calculating the refractive index or size of spherical particles because the pattern of scattered light from the particles is very sensitive to small changes in size or refractive index. Once the scattering pattern is measured, comparing it to the predicted values by Mie theory⁶⁶ allows particle size to be calculated if the refractive index is known. Mie theory underpins particle size analysis by laser light scattering.

There are a variety of light scattering instruments commercially available, which operate in three different modes: solid particles suspended in a liquid medium, widely separated

solid particles floating in a gaseous stream and solid or liquid particles suspended in a gaseous medium. In this study a HORIBA instrument was used where solid particles were analysed while dispensed in water.

2.8 Jeti Spectro-radiometer

This apparatus is used for study of light emission. It is composed of a main sensor which is placed above the panel while having the ability to locate the exact emission spot to the laser targeting component. The device is connected to a computer via a USB link and all measurements are calculated by the Jeti software making the whole analysis computerised and easy to use (Figure 2.5). The emission intensity (Cdm^{-2}), spectrum and dominant wavelength are calculated and presented.

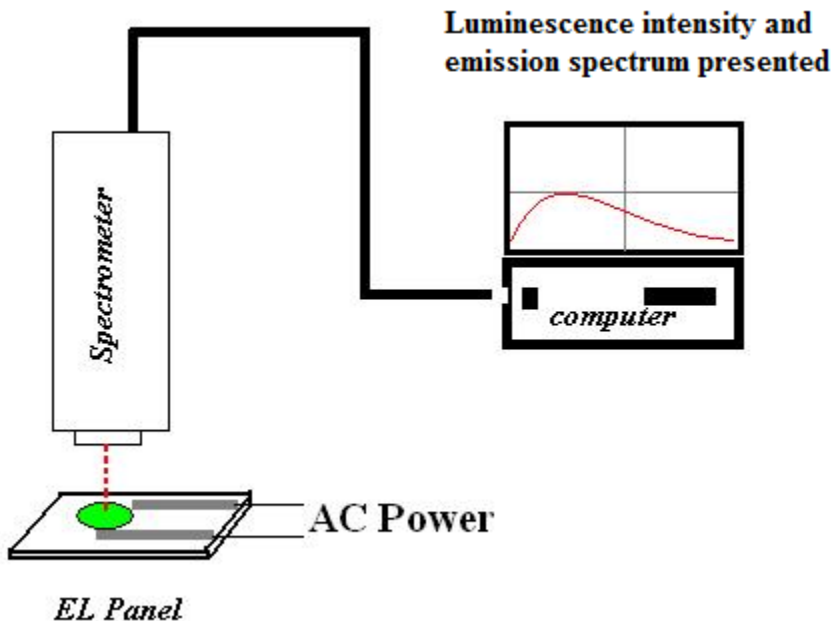


Figure 2.5: Analysis of the emission intensity, spectrum and dominant wavelength are calculated and presented by Jeti Spectrometer.

2.9 Photoluminescence (PL) emission spectroscopy

The sample being analysed is stimulated at a specific wavelength. A range of emission wavelengths can then be scanned, e.g. 300 to 700 nm. The instrument is equipped with software that can use the data output of the instrument, and produce the results in a graphical format (Figure 2.6).

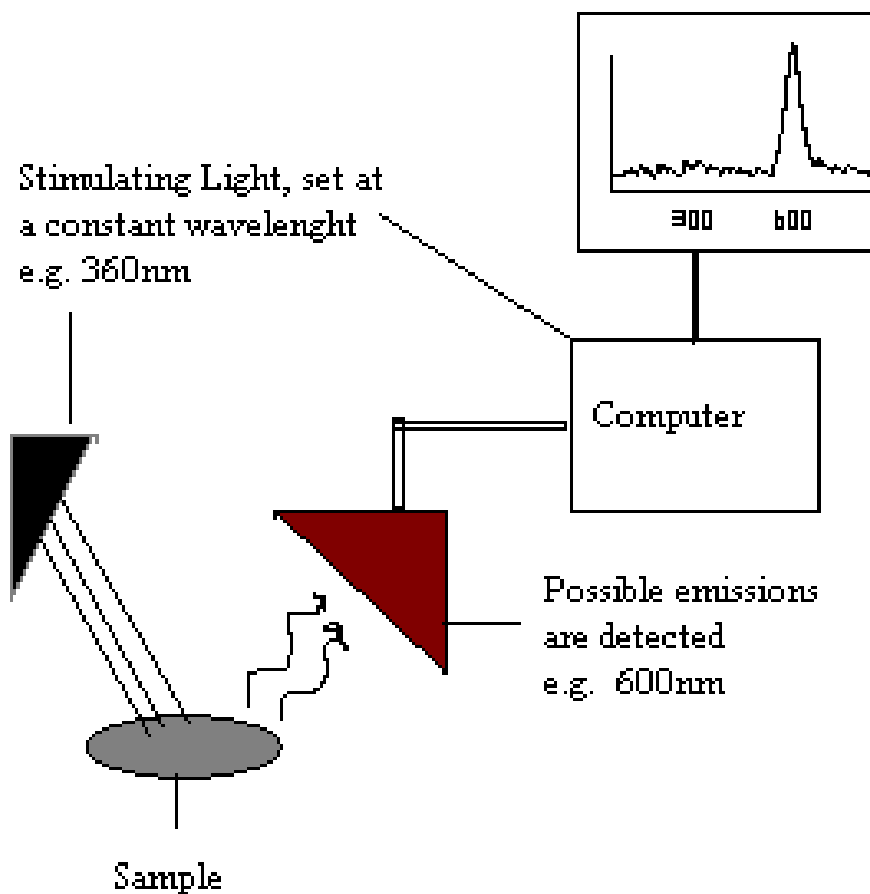


Figure 2.6 A simple representation of PL analysis. The sample is stimulated by a static wavelength and meanwhile screened for emissions. In this example, the imaginary sample is stimulated at a wavelength of 360 nm and the emission at 600 nm is detected. (Note that this diagram does not represent the actual mode of action by a specific PL spectrometer).

2.10 Elemental analysis via X-ray spectrometry

When a high energy beam of electrons interact with a specimen, the incident beam can excite electrons in discrete energy levels (electron shells) around the nucleus. These electrons will hence be ejected from their location and positively charged holes are created. Consequently the holes will be filled with an electron from higher energy shells and the difference in energy between the higher and lower shells can be emitted in form of an X-ray. The energy of the emitted X-ray can be measured by an energy dispersive spectrometer and interpreted as unique signals⁶⁷. Various signals produced are directly related to the chemical composition of the material. This approach allows the precise elemental composition of materials to be determined to a limit of ~0.1 – 1%. The TEM & SEM used for this experiment were equipped with an energy dispersive x-ray spectrometer (EDAX); elemental analyses can be obtained from small areas of the sample. This allows the precise determination of the composition of the sample. For example on one occasion during sample analysis, an image was observed which met with our expectations from the sample. However, after EDAX analysis it was shown that what we were observing was not part of the sample but was contamination caused by dirt.

Chapter 3 : Improving phosphor synthesis techniques

3.1 Introduction

Throughout this research, one of the main challenges was to produce phosphor materials with improved luminance output. A series of tests were designed to evaluate different factors during the synthesis which may play a key role in increasing the efficiency of the material in terms of light output. Meanwhile two techniques of zinc sulfide synthesis were evaluated for producing high quality zinc sulfide that can be used for EL phosphors. Thiourea dioxide (TDO) and Thioacetamide decomposition were tested. Using the zinc sulfide material produced via these techniques, some phosphor materials were produced. At the same time commercial luminescent grade ZnS from Sylvania was used to carry out phosphor synthesis and analysis of the materials. The work reported in this chapter examines the experiments that were carried out in achieving the synthesis of bright phosphor materials.

3.2 Zinc sulfide produced via thermal decomposition of thiourea dioxide (TDO)

The procedure for the synthesis of zinc sulfide involving thermal decomposition of thiourea dioxide in the presence of zinc ions in a solution was originally developed by Davies et al using zinc acetate⁶⁸. The ratio of zinc acetate to TDO needs to be 1:8 (w/w), respectively. To produce the particles, 50 g of zinc acetate was dissolved in 4 litres of deionised water and heated, using a stirrer, to 95°C. A total of 400 g of TDO was added to the solution, whilst being heated, stirred and allowed to react for one hour. The

precipitated ZnS was then filtered and washed with water and isopropanol (to obtain a shorter drying period).

The proposed reaction mechanism is presented in Figure 3.1.

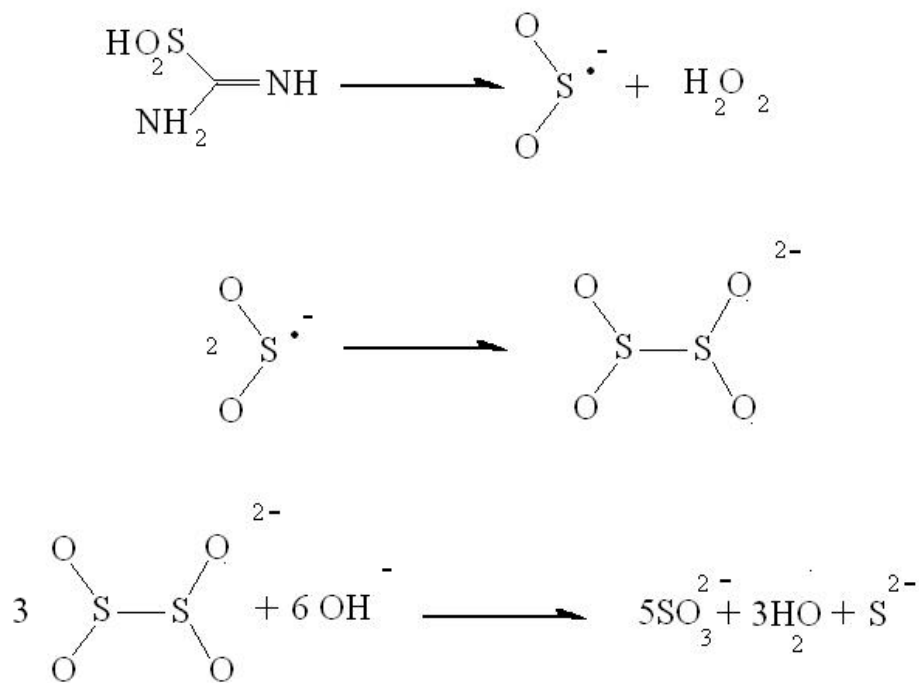


Figure 3.1: Reactions occurring during the thermal decomposition of thiourea dioxide.

The released sulfur ions are thought to react with the free zinc ions in the solution, thus forming the zinc sulfide particles. The zinc sulfide needs a copper impurity to become luminescent and hence copper acetate, in the required molar ratio, has to be added to the reaction mixture to produce the desired particles.

3.2.1 Synthesis of CuS together with zinc sulfide

A series of samples were prepared to incorporate the doping copper with the ZnS being synthesized as follows; a solution was prepared by dissolving 1g of copper acetate in 100 ml of deionised water. Two sets of a second solution were made by dissolving 50 g of zinc acetate (99.9% Aldrich) in 4 litres of deionised water and heated to 95 °C. Each of these two zinc acetate solutions was used to produce a phosphor with a different content of copper.

To the first solution 182 µL of the prepared copper acetate solution was added followed by the addition of 400 g of TDO. The sample prepared by this route was termed Cup 004 and contained 0.004 moles of copper per 100 moles of zinc. A second sample was prepared by adding 18.2 µL of copper nitrate solution following the same procedure which resulted in a sample containing 0.0004% copper content. This sample is referred to as Cup 0004.

Once dried the samples were heated at 800°C for a period of 1 hour using 10% (w/w) sodium chloride as flux. The samples were then washed using concentrated ammonia solution for a period of 48 hours. They were then used to prepare an AC panel and their electroluminescent behaviour was evaluated. The particles were analysed using scanning electron microscopy and x-ray powder diffraction. As shown in Figure 3.2, considering the emission intensity, both materials produced were very poor in terms of ACEL properties when compared to the commercial Sylvania phosphor.

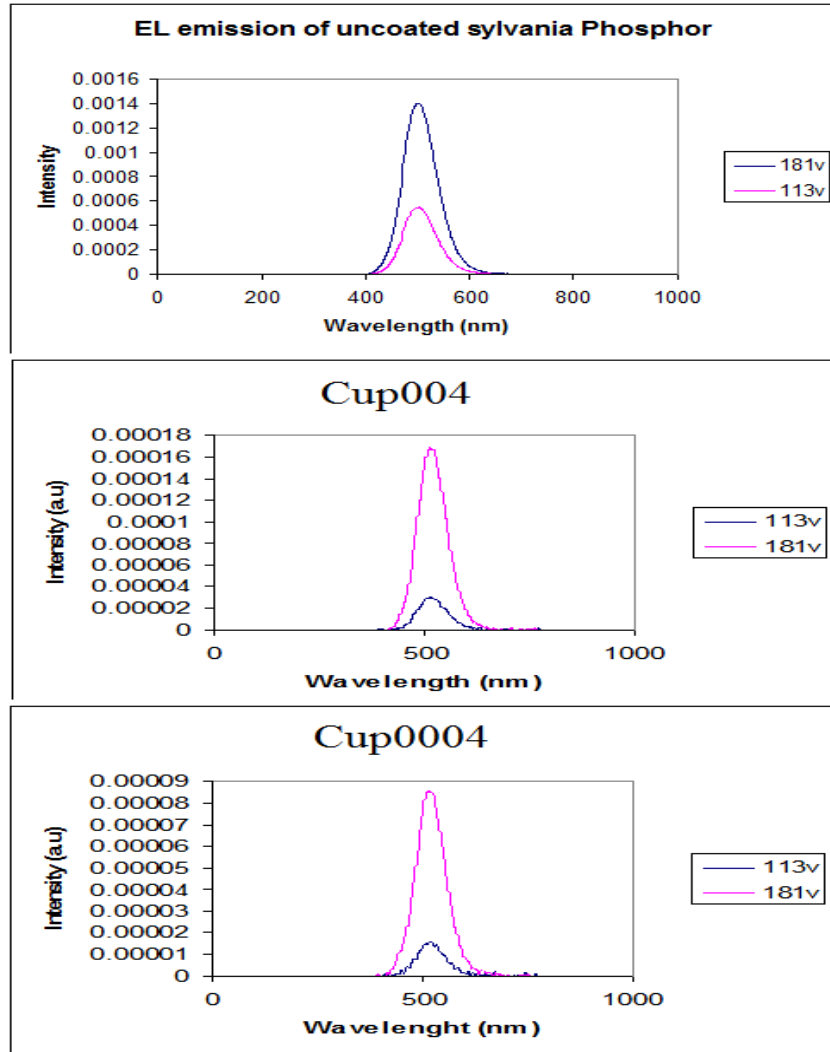


Figure 3.2: Electroluminescent properties of Cup004 and Cup0004 samples compared to commercial Sylvania ACEL phosphor at 100 Hz frequency using 181 and 113 V driving voltage.

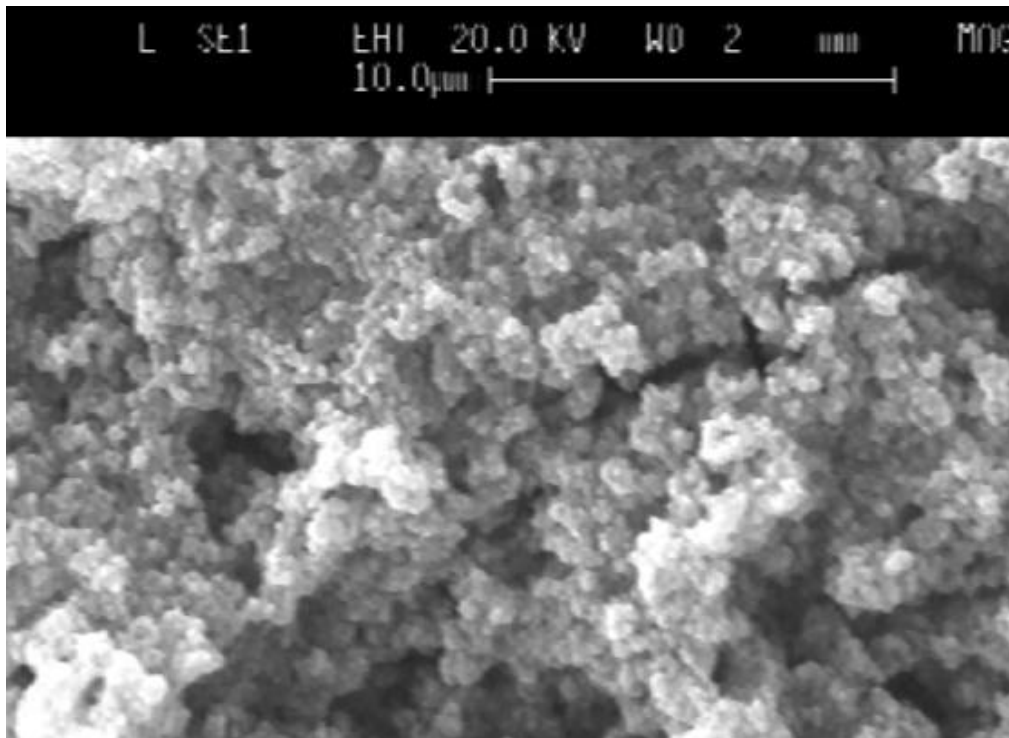


Figure 3.3: SEM analysis of Cup004 sample; fine powders agglomerated.

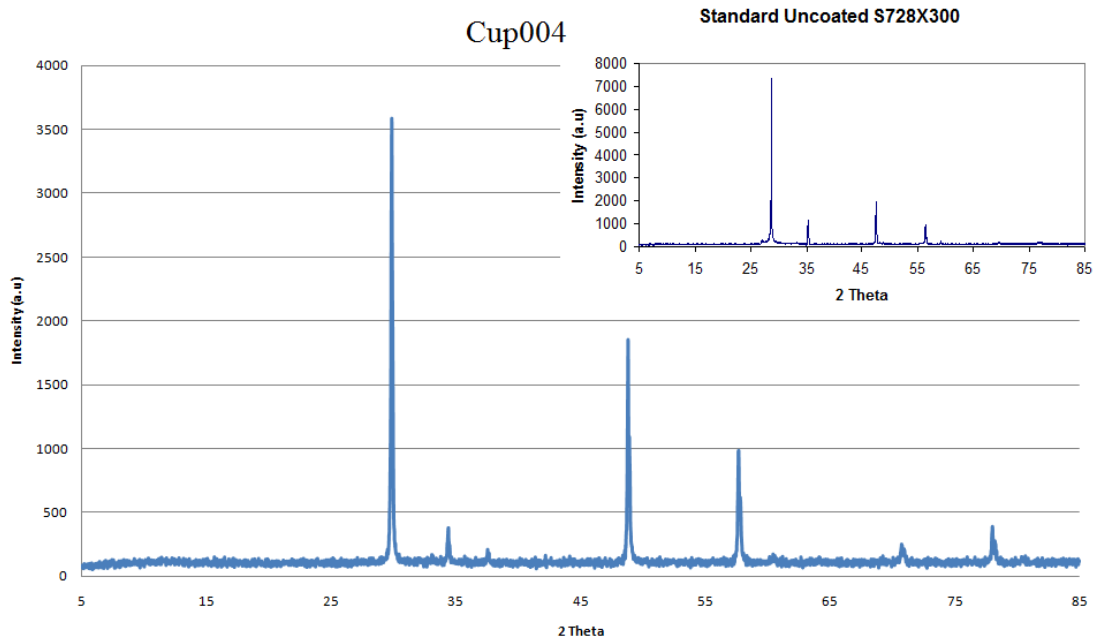


Figure 3.4: X-ray powder diffraction of sample Cup004 compared to commercial sample. Both samples demonstrate cubic crystal structure.

3.3 Preparation of zinc sulfide using thioacetamide

A zinc acetate solution was prepared as follows. 300 ml of deionised water in a 1 litre beaker was heated to 75°C on a magnetic stirrer/hotplate and 240 g of zinc acetate was added with stirring. Using the same copper acetate solution prepared earlier, a volume corresponding to 0.004% molar ratio of copper was added to this solution. The beaker was covered and re-heated to 75°C. When the zinc acetate had completely dissolved, the solution was filtered, using Whatman 542 filter paper. The solution was returned to a clean 1 litre beaker. The stirrer bar was removed and the beaker transferred to a water bath at 80°C with an overhead stirrer.

Thioacetamide solution was prepared as follows. 200 ml of deionised water in a 400 ml beaker was heated to 75°C on a magnetic stirrer/hotplate and 85 g of thioacetamide was added with stirring. The beaker was covered and re-heated to 75°C. When the thioacetamide had completely dissolved, the solution was filtered, using Whatman 542 filter paper. The solution was returned to the cleaned beaker. The stirrer bar was removed and the beaker transferred to the 80°C water bath.

The pH of the zinc acetate solution was adjusted as follows. A pH meter was calibrated using appropriate buffer solutions, then 30 ml of glacial acetic acid was added to the zinc acetate solution followed by 160 ml of ammonia solution (SG 0.88), added drop wise immediately, while the pH was monitored until a pH of 7.4 was obtained. The total amount of ammonia added was 185 ml.

The temperature of each solution was maintained at $80^{\circ}\text{C} \pm 2^{\circ}\text{C}$ before and after adding the thioacetamide solution to the buffered zinc acetate solution followed by 20 minutes stirring. The zinc sulfide precipitated was subsequently washed and filtered with water and isopropanol. The material was then washed with ammonia for a period of 48 hours to remove the excess copper. After drying, the material was analysed, as described in section 3.1. The x-ray analysis (Figure 3.5) confirmed the material to be zinc sulfide; however the material did not demonstrate any ACEL property when tested on a panel. Multiple attempts were made to prepare ACEL panel from these sets of material however no luminance was observed.

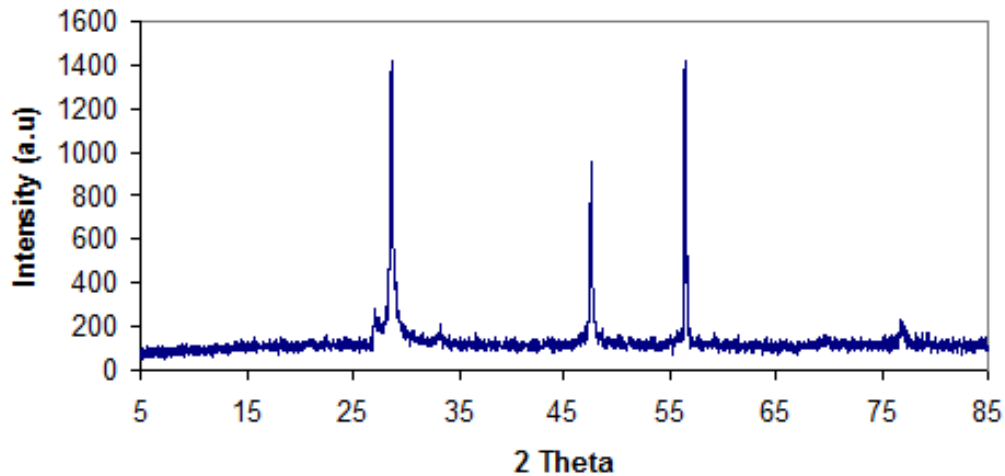


Figure 3.5: X-ray powder diffraction of copper doped zinc sulfide prepared by thioacetamide route with cubic crystal structure.

3.4 Using amorphous commercial luminescent grade zinc sulfide from Sylvania to prepare ACEL phosphors

Both the aforementioned techniques failed to produce ACEL zinc sulfide phosphor that can be regarded suitable in terms of performance for further analysis in this research, simply because their emission quality relative to the sensitivity of the jeti spectrometer were excessively weak making measurements and analysis unreliable. Hence, commercial grade undoped amorphous zinc sulfide was used for investigating multiple factors during the synthesis of ACEL phosphors. Various experiments were carried out ranging from analysing the effect of the salts used as a flux during the firing period, firing at controlled atmosphere and manipulating the preparation steps in making the phosphor.

3.4.1 Effect of various salts, NaCl, NaBr and NaI, as flux during the firing procedure

Understanding the role that the flux plays during the firing is desirable and hence a set of experiments were designed for this purpose. Initial experiments were designed by using various halide salts. It seemed important to investigate the anionic nature of the flux and the amount of flux used during the firing procedure in the hope of gaining information on the effects of the anions present during the firing. Using copper nitrate solution, an equivalent of 1.5% of copper to zinc (molar ratio) was added in aqueous form to the commercial amorphous zinc sulfide (Sylvania) followed by drying, hence yielding amorphous zinc sulfide and copper mixture (ZnS:Cu). Three samples were prepared for

firing as follows. 10 g of the ZnS:Cu was added to 1 g sodium salt^{xi} (chloride, bromide and iodide (99.8% Aldrich), the two were well mixed and placed in alumina crucibles. A minute amount of sulfur powder (99.99% Aldrich) was added to the top of the mixture in the crucible. The crucible was covered with the appropriate lid and placed in a furnace at 1000 °C and fired for a period of one hour.

After the firing procedure, the samples, which were hard solids, were ground and placed in 200 ml beakers. A 150 ml solution containing 50% water and 50% glacial acetic acid was added to the samples and brought to boiling while the sample was stirred with magnetic stirrer for a period of 10 minutes to wash off any zinc oxide covering the surface of the particles formed during firing procedure.

The samples were washed with excess water, placed in 200 ml beakers and washed with 150 ml of concentrated ammonia solution until the solution was blue and the powder samples developed a bright creamy colour, the sample that was fired using sodium chloride took 36 hours to be washed however the bromide and iodide fired samples were very difficult to wash as it took over 4 days for them to appear creamy in terms of colour appearance; an indication that the excessive copper was washed from them. The iodide salt produced a phosphor with peak emission at lower wavelength compared to the other two salts; chloride and bromide. However the ACEL emission (181 Volts and 400 Hz) of the samples were weak compared to the commercial Sylvania ACEL phosphor as demonstrated by the data in Figure 3.6.

^{xi} Phosphor precursor to flux ratio is 10:1, the 10 g quantity was chosen to suit the size of the crucibles.

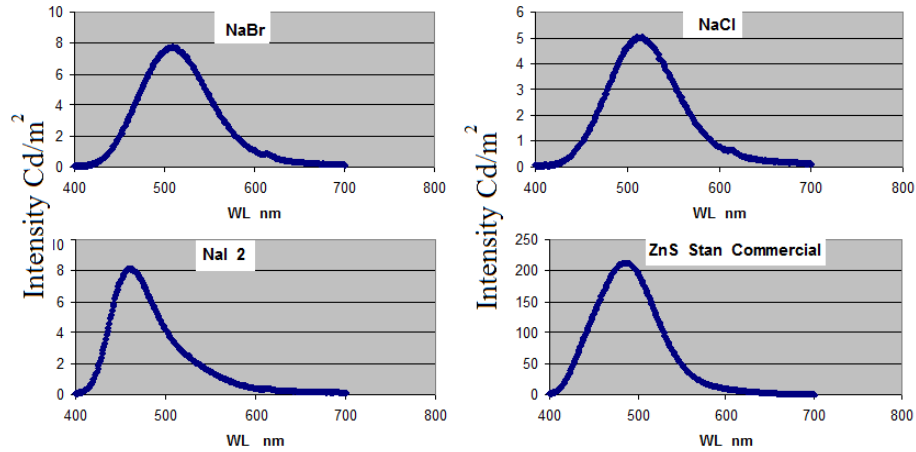


Figure 3.6: ACCEL emission of the ZnS:Cu phosphors fired using NaCl, NaI & NaBr as flux compared to the commercial zinc sulfide phosphor from Sylvania (intensity unit: $\text{Cd/m}^2 \times 10^{-4}$).

3.4.2 Firing under various amounts of NaCl as flux

These set of experiments were carried out in order to gain a better understanding of the role that the amount of flux plays during the firing of samples. As before, the amorphous zinc sulfide used during these experiments was a commercial luminescent grade ZnS from Osram-Sylvania and was doped with copper as previously described (section 3.4.1). The samples were prepared using 5 g of copper doped zinc sulfide and subsequently using 1 g, 5 g, 10 g and 15 g NaCl. The only sample that demonstrated a weak ACCEL effect was the one using 1 g of NaCl (~ 20% by weight) and the other samples did not show any ACCEL property indicating that the excessive amount of flux completely removes the doping copper during the firing.

3.5 Atmospheric conditions during firing

After the analysis was carried out on the above samples, a new set of experiments were designed to obtain an understanding of the effects of atmospheric conditions on the

synthesis of the ZnS:Cu phosphors. As mentioned earlier, all samples in the crucibles had sulfur (~ 0.1 g) added to them (just on the surface) prior to firing and the crucible was covered. This was undertaken to compensate for the possible loss of sulfur from the material during the firing procedure due to the high firing temperatures. So it became a matter of concern whether adding different quantities of sulfur to the material prior to firing would have an important effect on the quality of the prepared phosphor. Also, the effect of atmospheric oxygen during the firing procedure was an issue to investigate since at the experimental temperatures mentioned, oxygen would react with the zinc forming zinc oxide and hence reduce the total ZnS yield.

3.5.1 Firing under argon gas

Using a boat crucible and a tube furnace an experiment was designed to enable firing of the phosphor under a controlled argon atmosphere, as shown in Figure 3.7.

Using the previous copper doped zinc sulfide preparation technique (section 3.4.1) three sets of samples were produced by firing 5 g of the phosphor + 1 g of NaCl fired at 850°C for 1 hour using the set up shown in Figure 3.7. The samples differed in the amount of powder sulfur added to the surface; SAr0, SAr0.4 and SAr1 containing 0 g, 0.04 g and 1 g sulphur, respectively.

After firing, all three samples were extremely rocky and hard and had to be crushed with force and extensive grinding. It is important to note that the extensive grinding may affect the total crystal form of the material which is an important factor when considering ACEL. The samples took over 4 days to be washed by ammonia and by this time very little material was left, hence this method did not seem to be a viable method for

producing ACEL zinc sulfide particles. The samples demonstrated a weak ACEL effect. Scanning electron microscopy and x-ray powder diffraction of the materials did not indicate any difference in terms of particle size distribution, morphology or crystal structures as demonstrated by the data in Figures 3.8 and 3.9.

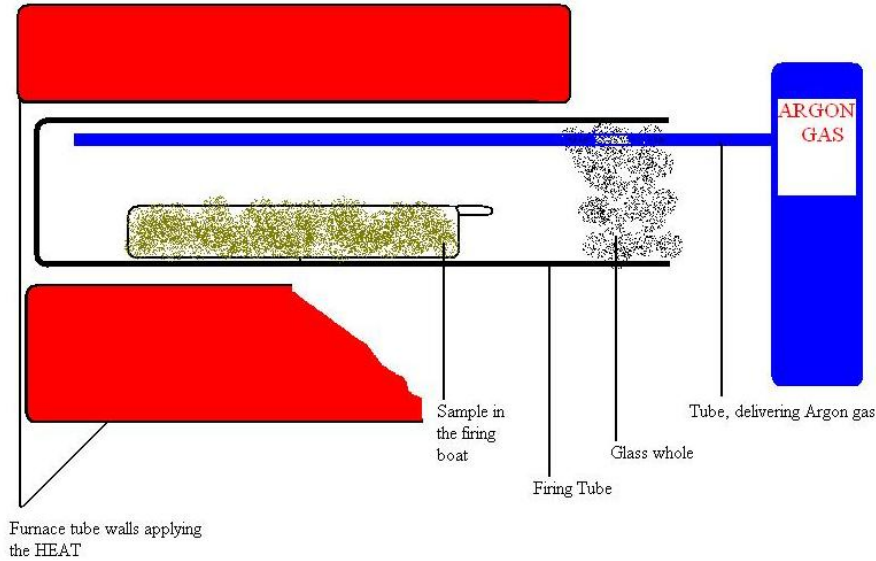


Figure 3.7: Firing of zinc sulfide in an argon controlled atmosphere.

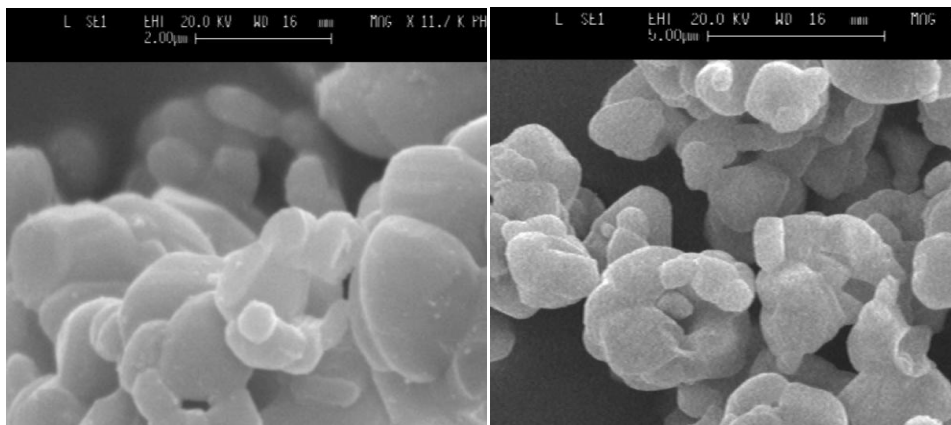


Figure 3.8: SEM analysis of the SAR0 (left) and SAR1(right) samples after firing at 850°C.

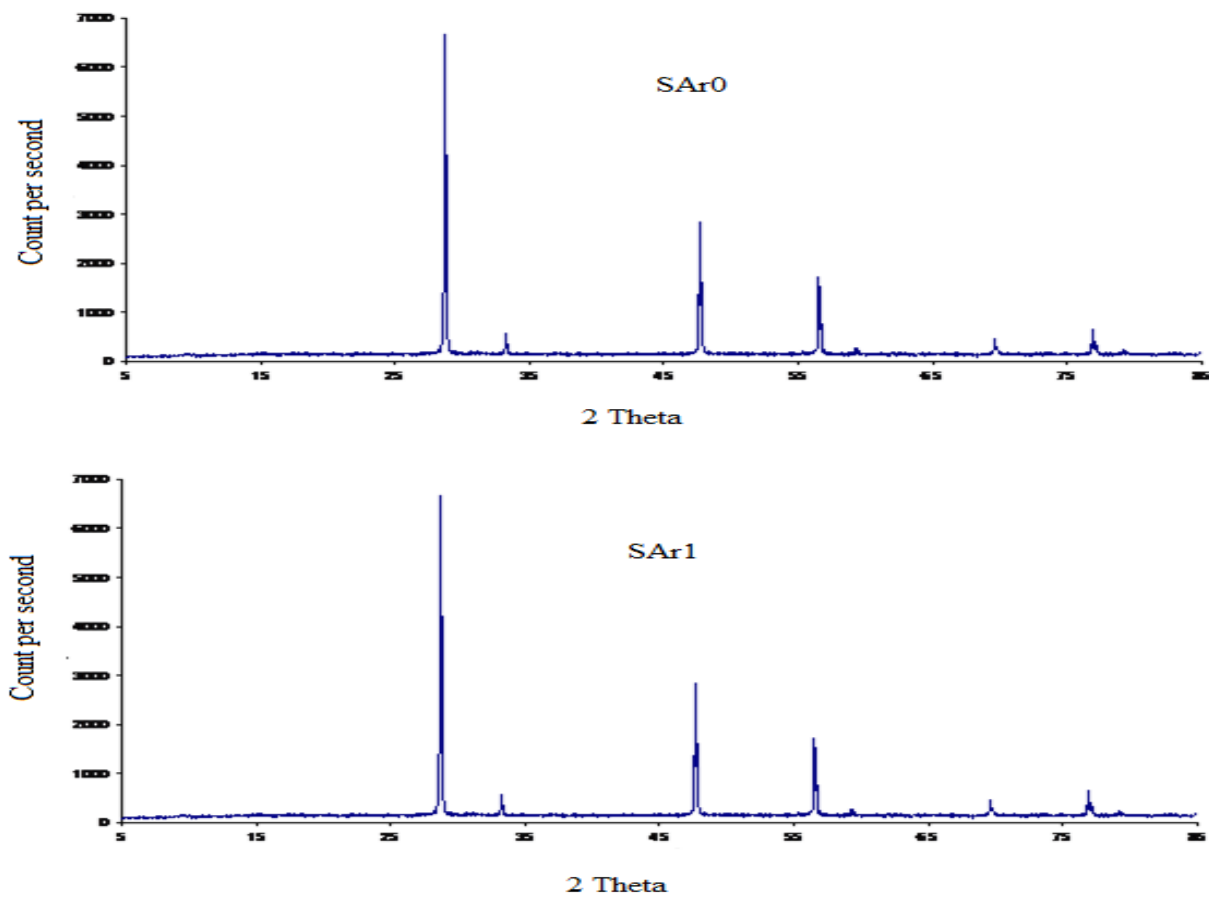


Figure 3.9: X-ray powder diffraction of SAr0 and SAr1 samples. The cubic crystal structure of the powders is unaffected by addition of sulfur.

3.5.2 Firing under hydrogen sulfide gas (H₂S)

These tests were carried out to observe the possible effects of firing samples under H₂S gas. Figure 3.10 shows the structural setup used to perform these tests:

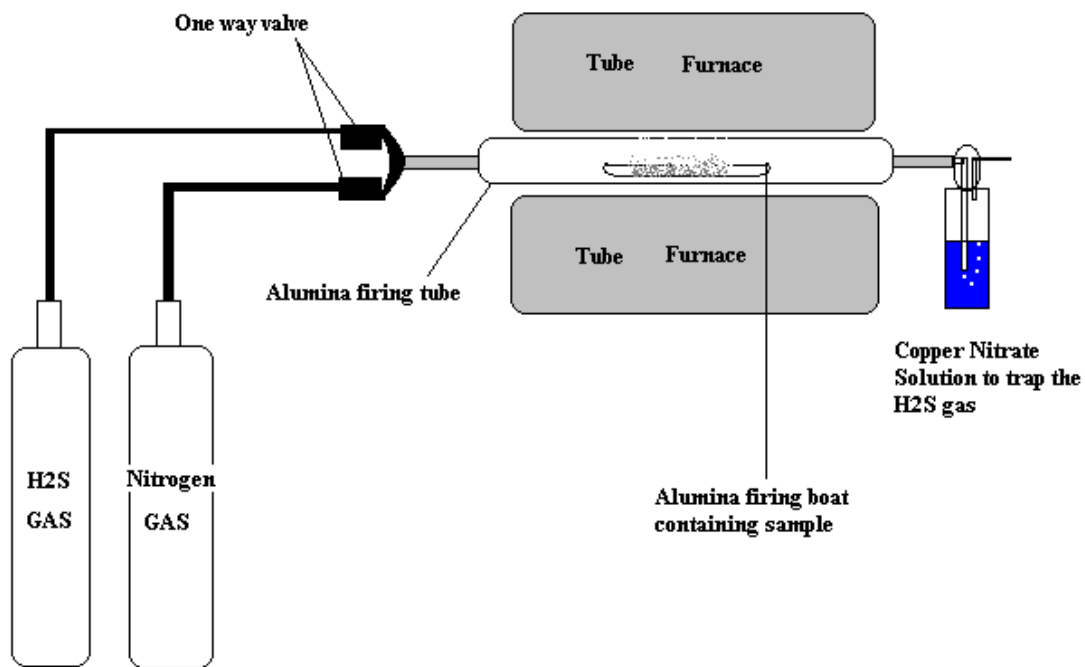


Figure 3.10: Firing of zinc sulfide under hydrogen sulfide & nitrogen controlled atmosphere.

Two identical samples were prepared as before (5 g of doped zinc sulfide and 1 g NaCl, no sulfur added) containing the copper doping. Just like firing under argon gas, the sample was placed in the firing boat for one hour before the furnace was switched off to

ensure that no oxygen was present during the firing, the setup was flushed with nitrogen prior to turning on the furnace.

One of the samples was fired at 850°C for a period of one hour and the other was fired for two hours. This procedure again produced extremely hardened solids which required extensive crushing and grinding and extensive ammonia washing. The ACEL properties of the material were extremely poor and undetectable by the Jetti spectrometer.

3.6 Enhancing the preparation steps during the firing of the materials

Commercial amorphous zinc sulfide was used to produce two stock sources for preparation of the majority of this study. They were named Source Alfa and Source Delta. They were prepared by mixing appropriate amounts of aqueous copper nitrate with an equivalent amount of zinc sulfide to obtain the desired copper to zinc molar ratio of 1.2% and 0.6% i.e 1.2 moles and 0.6 moles of copper per 100 moles of zinc. The samples were stirred for 15 minutes followed by filtration and drying in a oven at 100°C. A double firing technique was developed which produced phosphors demonstrating higher luminance. In this technique the samples were fired twice, initially fired without any flux followed by a second firing where sodium chloride was used as flux. For evaluation purposes a series of tests were carried out to compare single and double firing techniques. These samples were fired in a double covered crucible and sodium chloride was used between the two crucibles to allow the hot material to cool steadily (Figure 3.11).

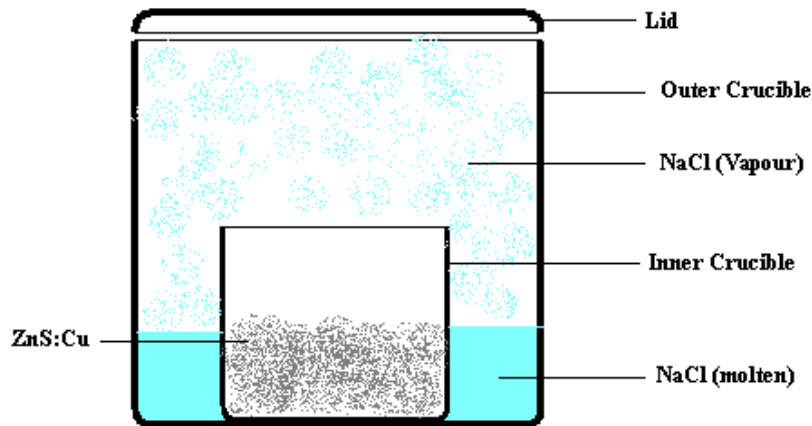


Figure 3.11: Firing of the materials in covered crucible, using NaCl bath to ensure the material is cooled steadily when removed from the furnace.

3.6.1 Single firing tests

A total of 40 g ZnS:Cu from source Alfa was used to carry out this study. The material was divided into four 10 g portions. Using 0.5 g, 2 g, 3 g and 4 g of NaCl mixed thoroughly with the material; each portion was fired at 850°C. These samples were named: AmL1, AmL2, AmL3 and AmL4, respectively. These samples were subsequently used to evaluate the double firing technique. They were analysed by SEM and XRD and their ACEL properties were investigated (figure 3.12). In terms of crystal structure and morphology all samples were similar in appearance (morphology and size).

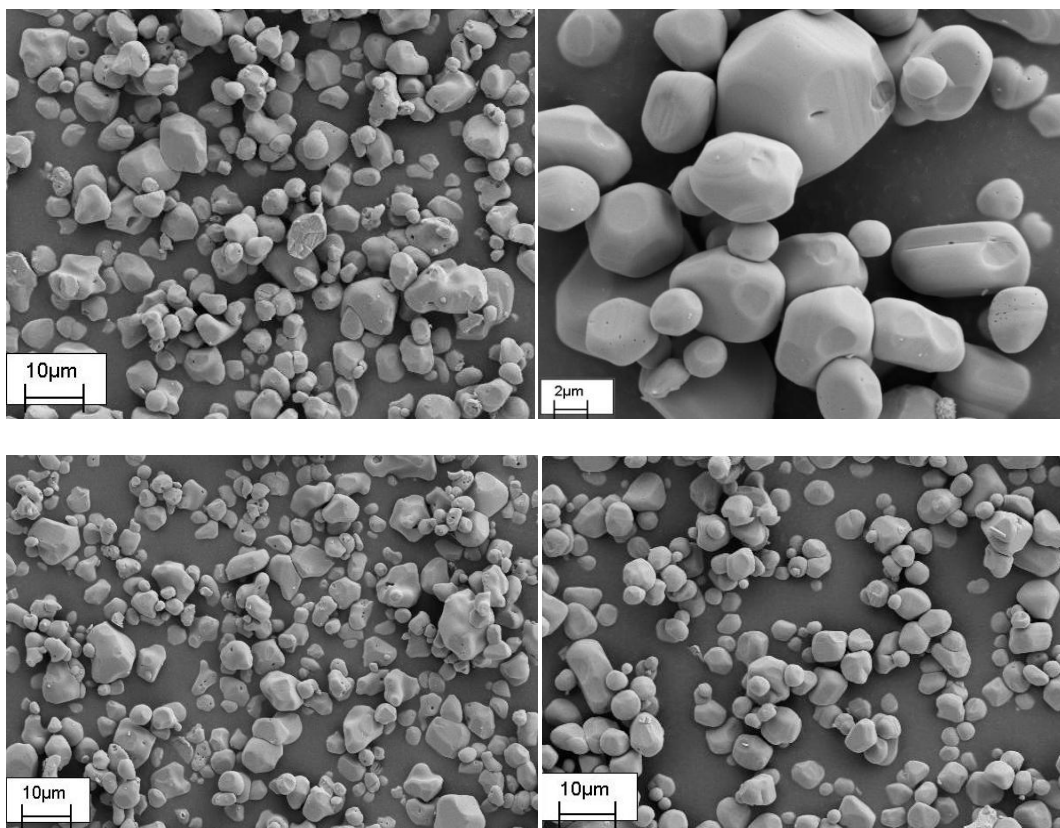


Figure 3.12: SEM analysis of samples AmL1 (bottom), AmL2 (top left) and AmL4 (top right & bottom).

3.6.2 Double firing tests

A total of 42 g ZnS:Cu from source Alfa was fired at 850°C for a period of 2 hours. After firing the top layer of the fired sample was removed (the thin top layer is exposed to air and hence contained higher zinc oxide content) and the sample was used as a source for further preparation of samples in this section. Using four equal 10 g portions of this material, four samples were prepared by firing each 10 g portion with 0.5 g, 2 g, 3 g and 4 g of NaCl mixed thoroughly with the material for a period of one hour at 850°C. These samples were then named AmF1, AmF2, AmF3 and AmF4, respectively.

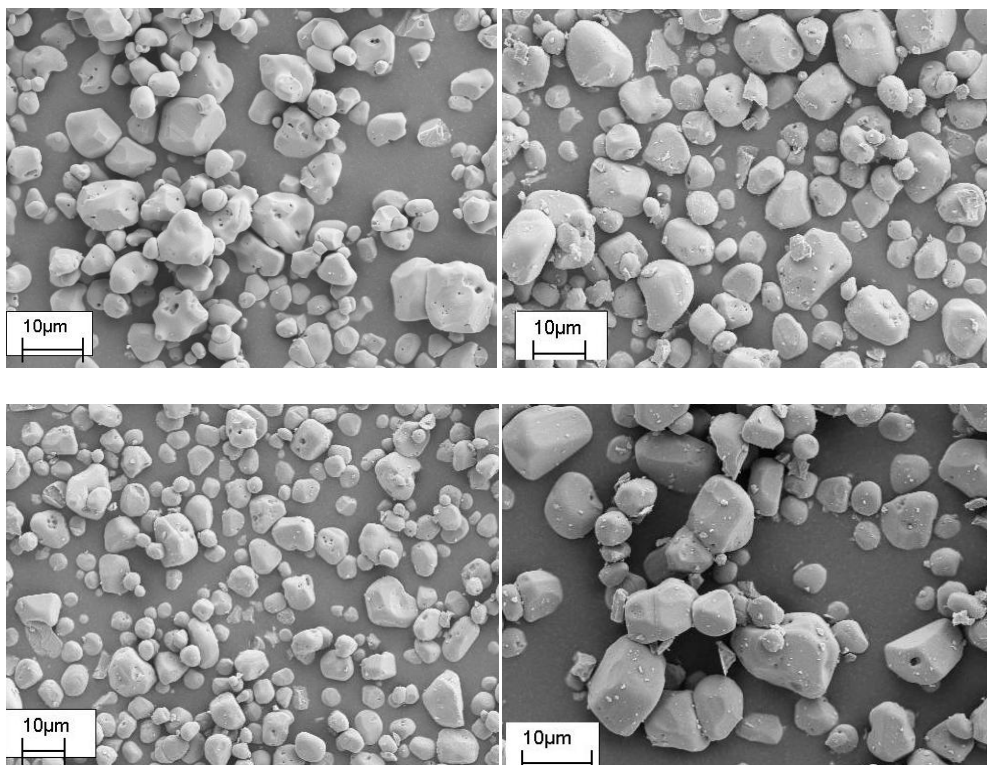


Figure 3.13: SEM analysis of samples AmF1 (top left), AmF2 (top right), AmF3 (bottom left) & AmF4 (bottom right).

Both AmL and AmF series of samples were analysed by ICP-MS to measure the copper content in each and they were compared with commercial grade Sylvania ACEL phosphor (Figure 3.15).

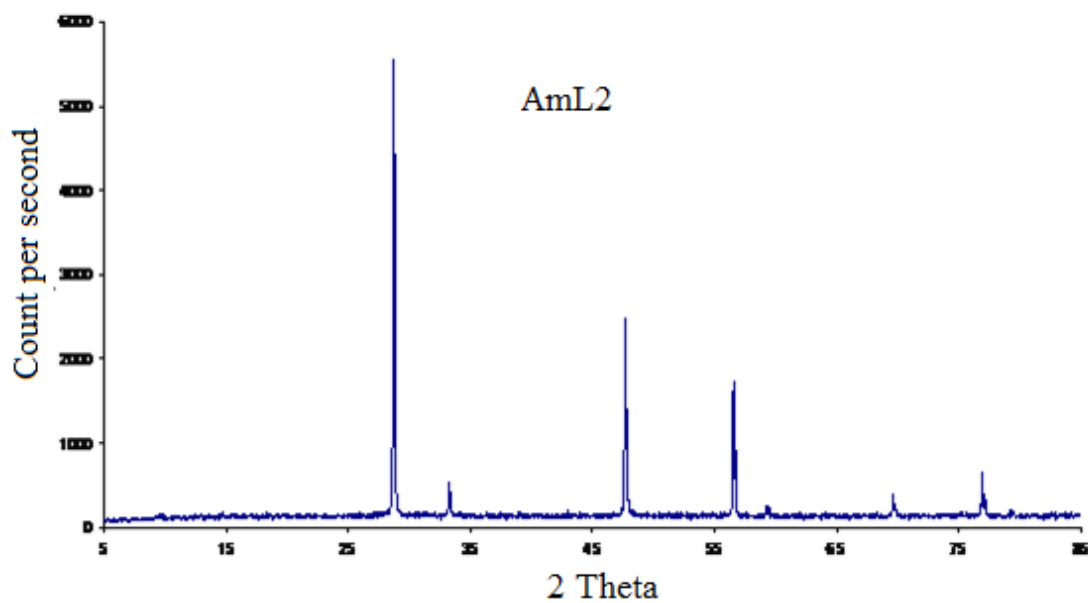
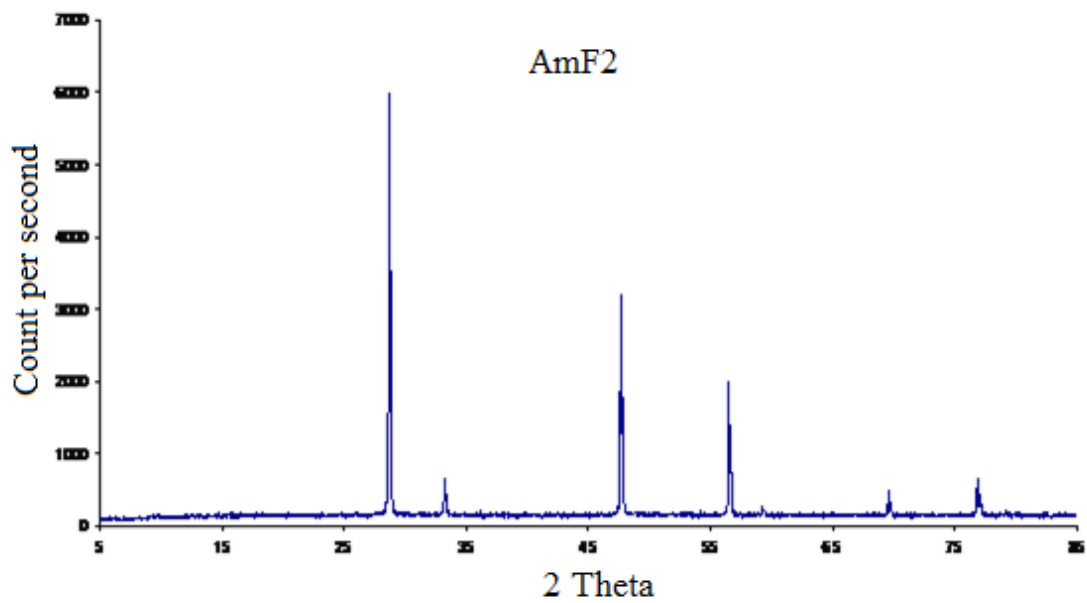


Figure 3.14: X-ray powder diffraction of AmF2 & AmL2 samples. No observable difference in crystal structure.

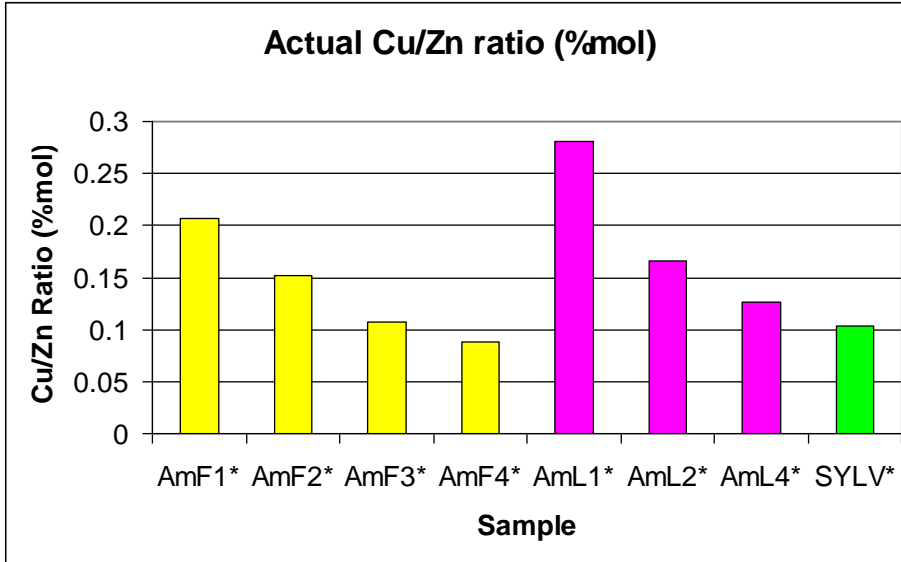


Figure 3.15: The ratio of Cu/Zn in terms of moles of copper per 100 moles of zinc based on results from ICP-MS analysis for AmF and AmL samples compared to commercial grade Sylvania ACEL ZnS:Cu phosphor.

3.6.3 Enhancing the double firing technique

These tests were designed to further assess the double firing technique of producing the phosphor materials. Considering that the material was fired in two stages it seemed vital to investigate the possible effects that the duration of firing period would have on the emission quality of the phosphor. By preparing a 0.64% Cu containing zinc sulfide, four samples were prepared using various firing time arrangements in the preparation of each sample.

Using copper nitrate (0.567 g), a 20 ml solution of copper nitrate was prepared and 46 g of amorphous Sylvania zinc sulfide was added to this solution. After filtration and drying, four portions of 10 g were selected for further analysis as follows.

T22A: 10 g sample was fired at 850°C for ½ hour followed by addition of 2% NaCl and re-fired at 850 for ½ hour. T22B: 10 g sample was fired at 850°C for ½ hour followed by addition of 20% NaCl and re-fired at 850 for 2 hour. T22C: 10 g sample was fired at 850°C for 4 hour followed by addition of 2% NaCl and re-fired at 850 for ½ hour. T22D: 10 g sample was fired at 850°C for 4 hour followed by addition of 20% NaCl and re-fired at 850 for 2 hour.

The samples were washed with ammonia and were analysed for ACEL properties using the Jeti spectroradiometer. The results are presented in Figures 3.16-18 as the samples were compared to a Sylvania's commercial ZnS:Cu ACEL phosphor.

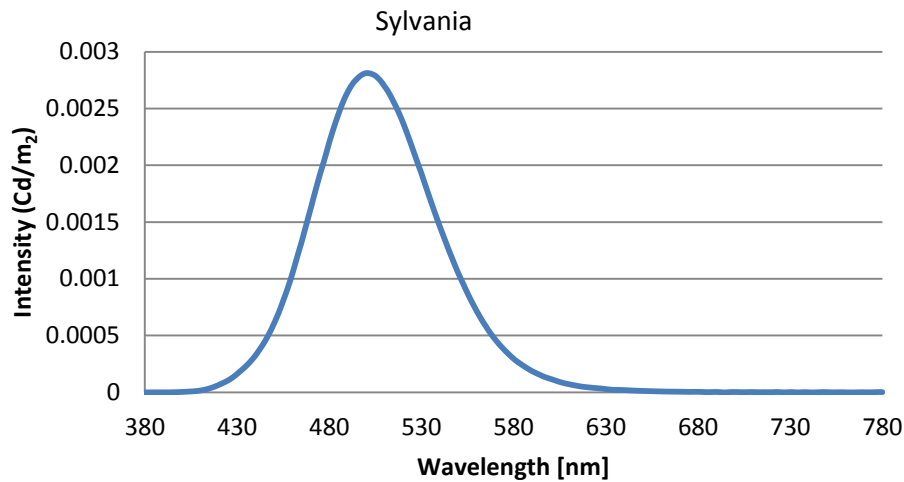


Figure 3.16: ACEL emission intensity of commercial copper doped zinc sulfide produced by Sylvania at 181 Volts and 400Hz frequency.

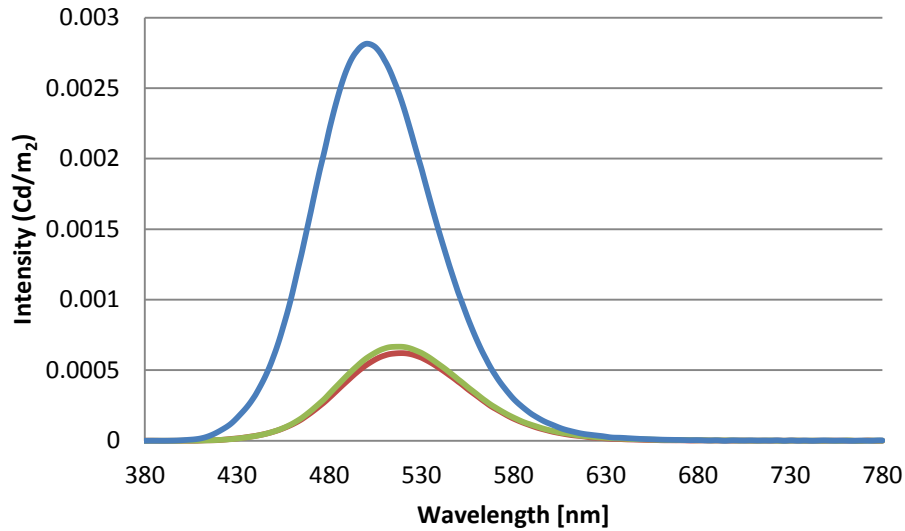


Figure 3.17: ACEL emission of T22A (red) and T22B (green) compared to commercial Sylvania phosphor at 181 volts and 400Hz frequency. No significant difference between the two samples but weak emission compared to the commercial samples.

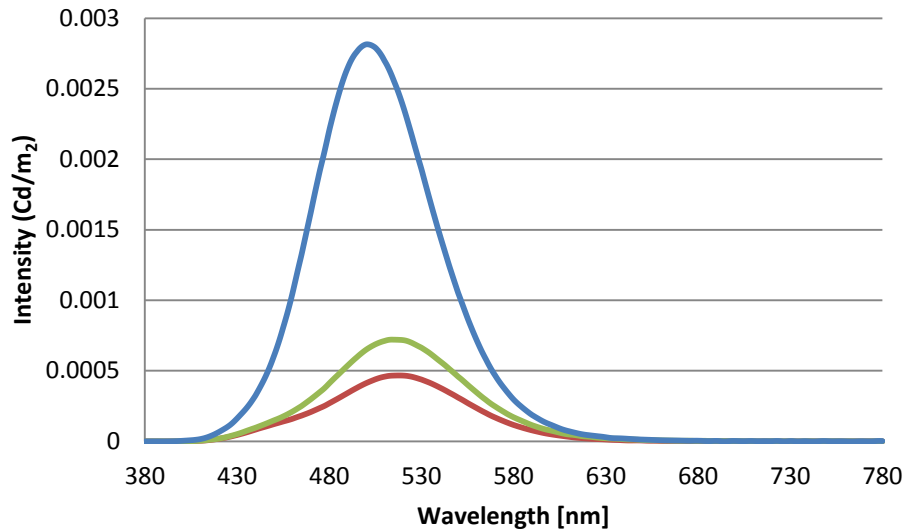


Figure 3.18: ACEL emission of T22C (Red) and T22D (green) compared to commercial Sylvania phosphor at 181 volts and 400Hz frequency. The synthesis technique of T22C seems inferior to the other T22 samples in terms of intensity output.

3.6.4 Copper content & the double firing technique

In all previous sections the general procedure of adding the copper to the zinc sulfide involved dissolving the appropriate amount of copper nitrate in 20 ml of deionised water. Then the zinc sulfide was added to this solution and stirred for a period of 15 minutes. The sample was then filtered and dried to be used as a specimen for firing.

A series of tests were carried out to study the luminescent properties of the phosphor materials made using various amounts of doping copper. Three samples were prepared by using three portions of 40 g amorphous Sylvania zinc sulfide dispersed in water followed by the addition of 0.3 g (H1), 0.15 g (H2) and 0.075 g (H3) of $\text{Cu}(\text{NO}_3)_2$, respectively to each 40 g batch of the zinc sulfide. These samples were then filtered and dried at 100°C for 24 hours as a source for further tests. Using 20 g of each of the above sources, three samples were prepared by double firing the material at 850°C for two consequent periods of 1 hour, using 20% by weight sodium chloride as the flux on the second stage of firing. Finally samples were washed with ammonia, as described previously.

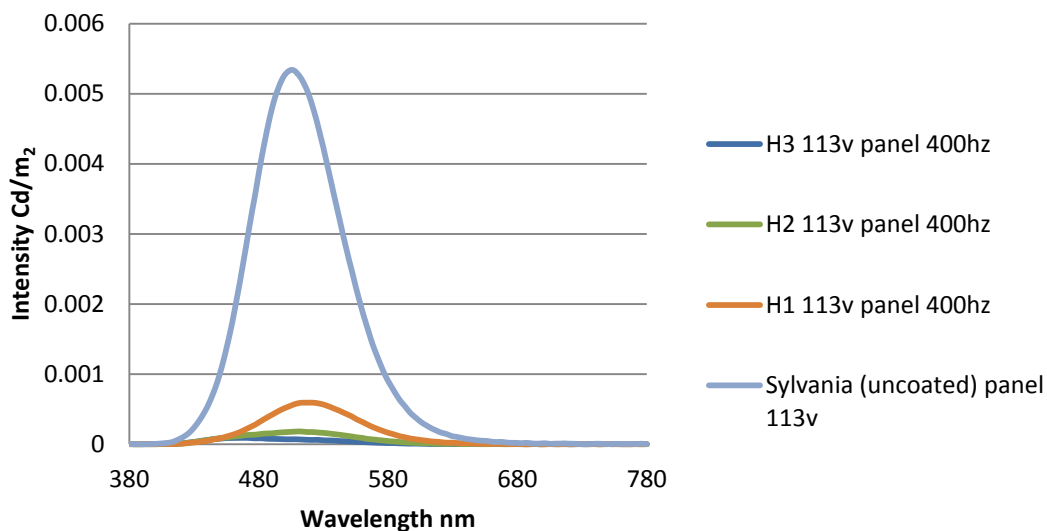


Figure 3.19: ACEL emission of the H1,2 and 3 samples compared to Sylvania phosphor at 113 volts and 400Hz.

Using the remaining 20 g of the H1, 2 and 3 samples prepared earlier, this test was carried out to investigate possible effects of converting the copper residues into copper sulfide within the amorphous zinc sulfide / copper precursor.

These samples were placed in deionised water and a mixture of hydrogen sulfide gas and nitrogen was bubbled through the water while it was stirred for a period of 15 minutes. The solution was flushed using nitrogen gas for 15 minutes. The samples were then filtered, dried and fired, respectively as described in and named H1s, H2s and H3s. It was hypothesised that this procedure would convert the well distributed copper ions throughout the zinc sulfide particles into CuS and this study in parallel to the finding from H series samples already mentioned, would produce some valuable information into the nature of the Cu atoms and its effect on the quality of the phosphor prepared. The samples were named H1S, H2S and H3S, respectively. They were then fired in the same fashion as H1, 2 and 3 were prepared and their ACEL properties were investigated

(Figure 3.20). ICP-MS analysis was carried out to measure the copper content of the samples after firing to gain an insight into how much of the initial copper diffuses into the lattice (Figure 3.21).

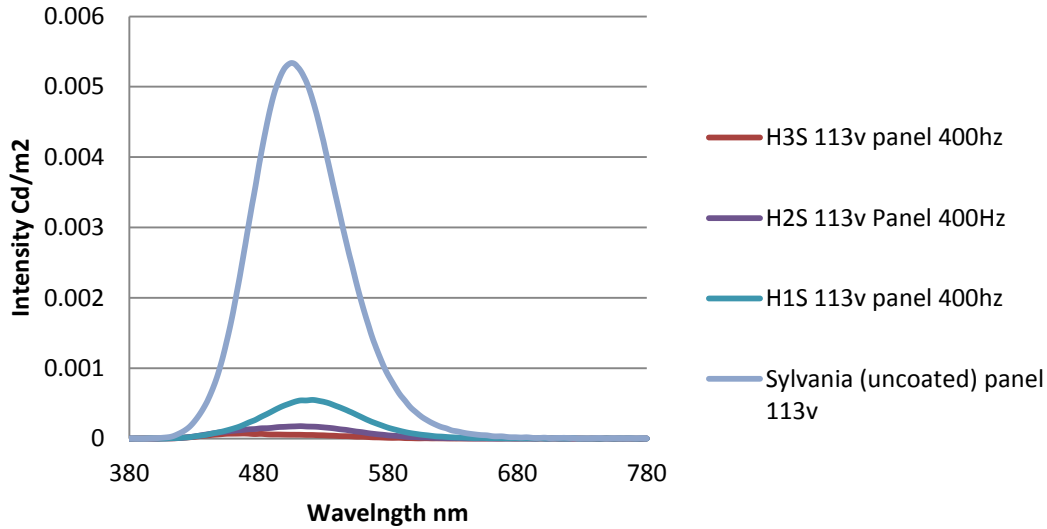


Figure 3.20: ACEL emission of the H1S,H2S and H3S samples compared to Sylvania phosphor at 113Volts and 400Hz. The H2S and H3S samples demonstrate weak emission possibly due to the low level of copper impurity present in ZnS host as illustrated in figure 6.21.

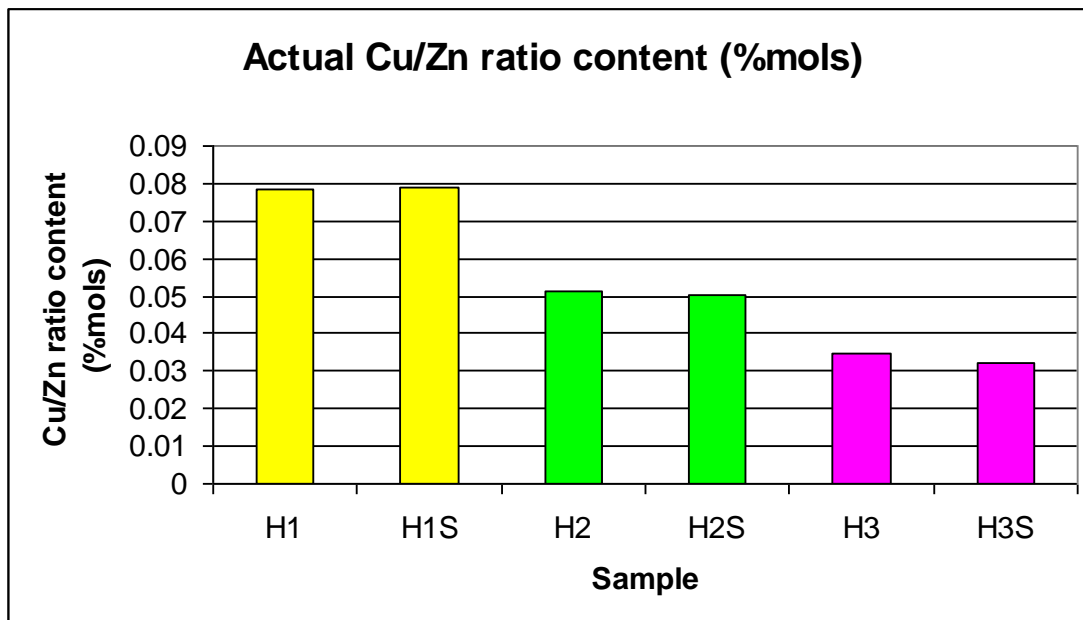


Figure 3.21: The ratio of Cu/Zn in terms of moles of copper per 100 moles of zinc, based on results from ICP-MS analysis for H series samples. H1 and H1S samples contain the highest amount of copper impurity.

3.6.5 Mixing copper doped and un-doped amorphous zinc sulfide prior to firing

Double fired samples demonstrated better emission properties compared to single fired samples. Hence the double firing technique was used to investigate a series of tests. The idea of these tests involved various random alterations to the pre-fired zinc sulfide constituents. Two samples named D1 and D2 demonstrated the best results. They were prepared in the following fashion. A source of zinc sulfide was prepared by dissolving 3.451 g of copper nitrate in 200 ml of water. Then 300 g of amorphous Sylvania zinc sulfide was added to this solution and the mixture was stirred for 15 minutes. This material was filtered and dried. This was named source DELTA containing 0.6% copper and samples D1 and D2 were prepared using this source.

D1: 20 g of source DELTA was mixed thoroughly with 5 g of pure Sylvania zinc sulfide. This mixture was fired at 850°C for a period of two hours.

After the first firing, the sample was mixed with 5 g of sodium chloride and re-fired at 850°C for one hour. The sample was then washed with ammonia for a period of 24 hours.

D2: 20 g of fired source DELTA (850°C for 1 hour) was mixed thoroughly with 5 g of source DELTA. This mixture was fired at 850°C for a period of two hours.

After the first firing, the sample was mixed with 5g of sodium chloride and re-fired at 850°C for one hour. The sample was the washed with ammonia for a period of 24 hours

Panels were prepared from these materials and the ACEL property of the panels are shown in Figure 3.22 where D1 sample is compared to the Sylvania ACEL ZnS:Cu phosphor; in Figure 3.23 D1 and D2 are compared against each other. The D1 and D2 particles were analysed by x-ray powder diffraction confirming a cubic crystal structure. Scanning electron microscopy of the materials demonstrates a non-uniform size distribution ranging from 1 to 30 micrometer particles as presented in Figures 3.24 and 3.25.

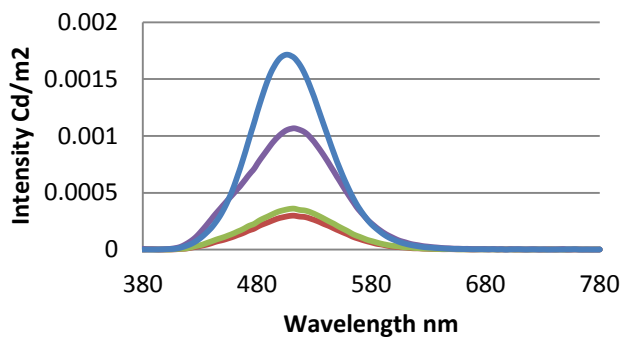


Figure 3.22: *D1 (red: 113v, green 123v, purple 181v) sample compared to Sylvania (blue 181v) using 400 Hz frequency. This sample is a close match (66.66%) to commercial samples.*

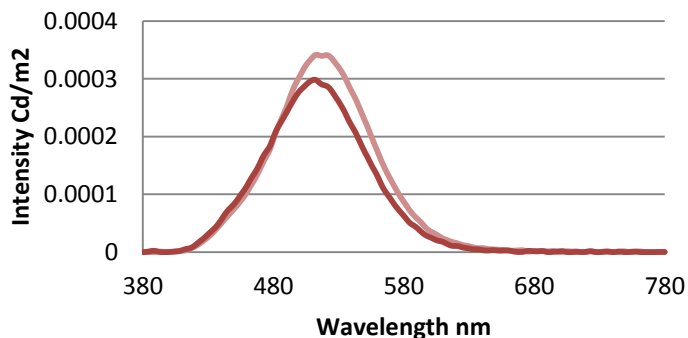


Figure 3.23: *D1 sample (red) compared to D2 (pink) using 113v driving voltage and 400Hz frequency.*

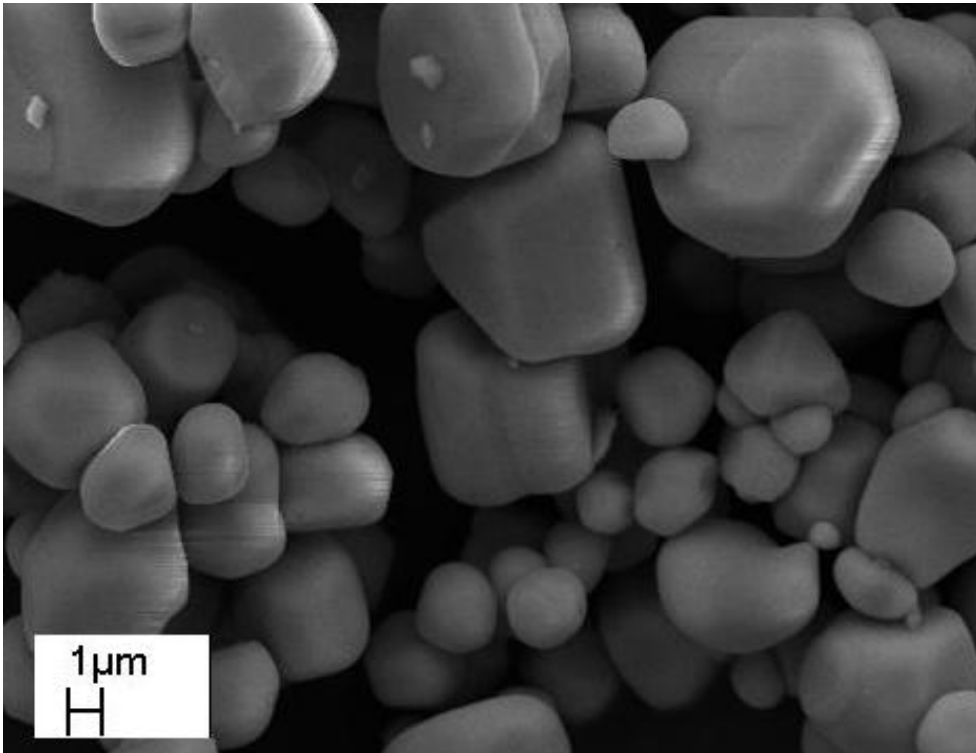


Figure 3.24: SEM analysis of D1 samples. Particle's sizes range from 1-10 microns.

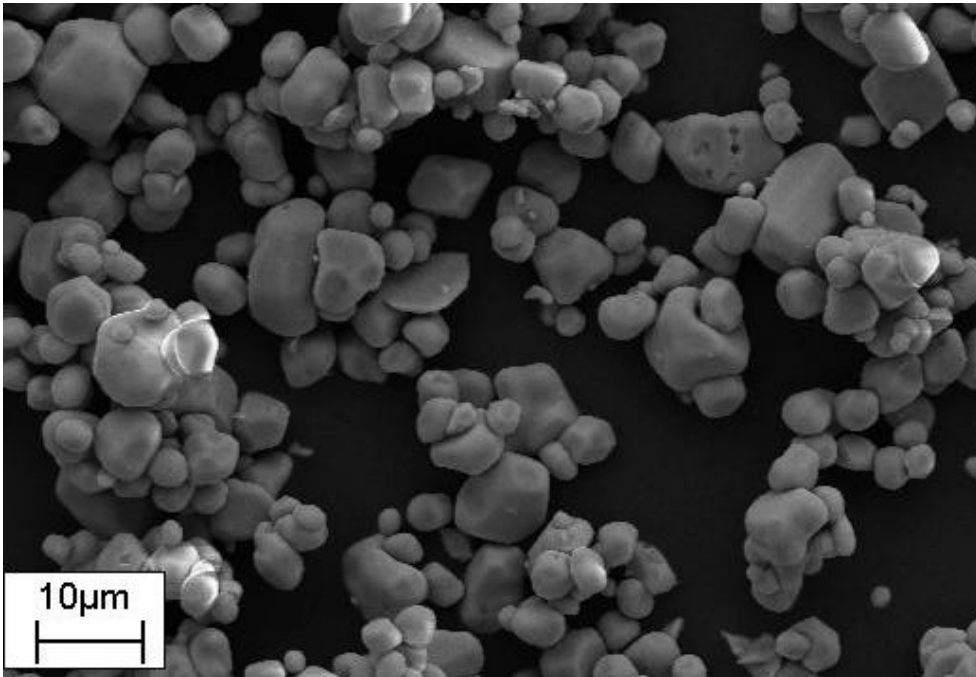


Figure 3.25: SEM analysis of D2 samples. Particle's sizes range from 1-10 microns.

Using a screen printing machine (courtesy of Brunel University) two panels were made using Sylvania ACEL ZnS:Cu and D1 sample. The screens were analysed using scanning electron microscopy as demonstrated in Figures 3.26 and 3.27. The Sylvania made phosphor particles, due to their more uniform size distribution, form a uniform surface that takes maximum advantage of the space while the D1 samples are not packed into a uniform layer.

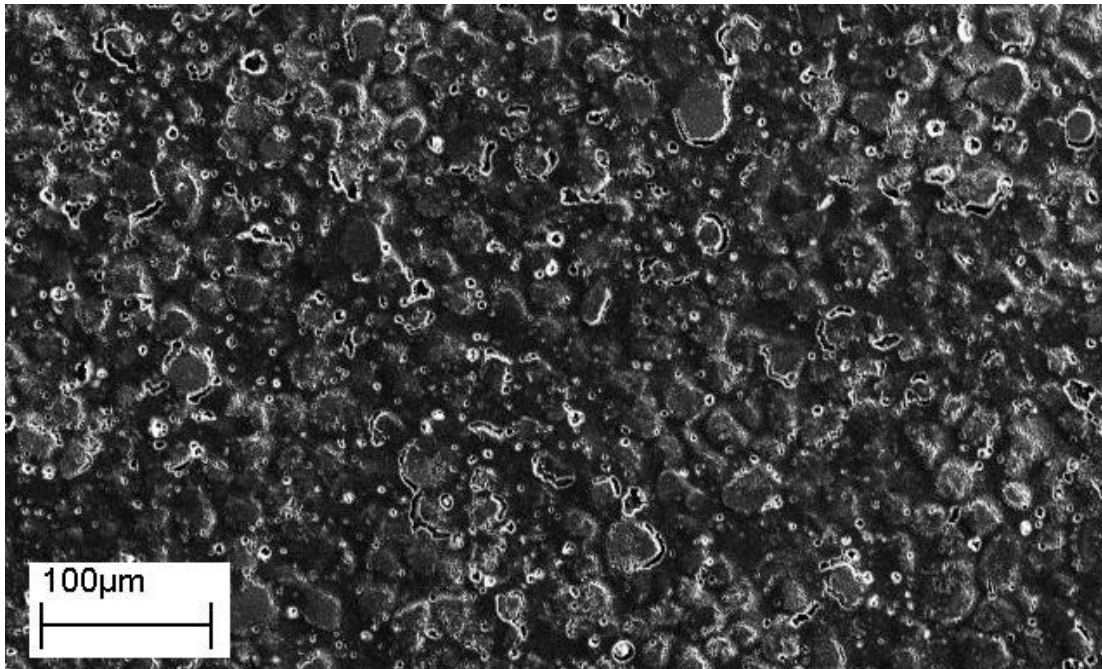


Figure 3.26: Surface of panel prepared by the D1 phosphor. D1 samples due to their smaller size (~5 microns) demonstrate closer packing along with agglomerations when screen printed.

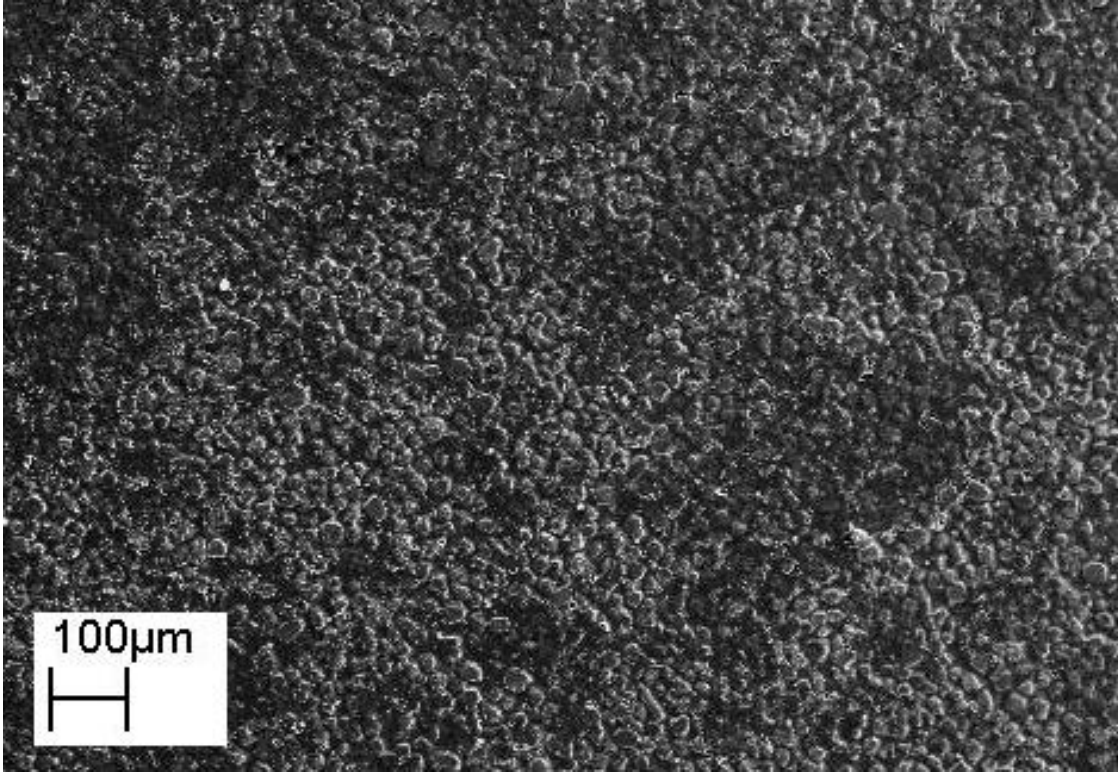


Figure 3.27: Surface of panel prepared by the Sylvania phosphor. The larger size of these particles (~30 microns) seems to create a more homogenous film when screen printed.

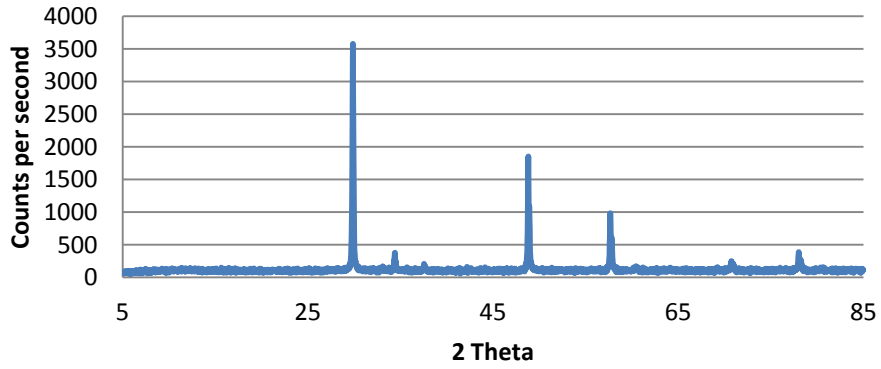


Figure 3.28: X-ray powder diffraction of the D1 sample demonstrating cubic crystal structure.

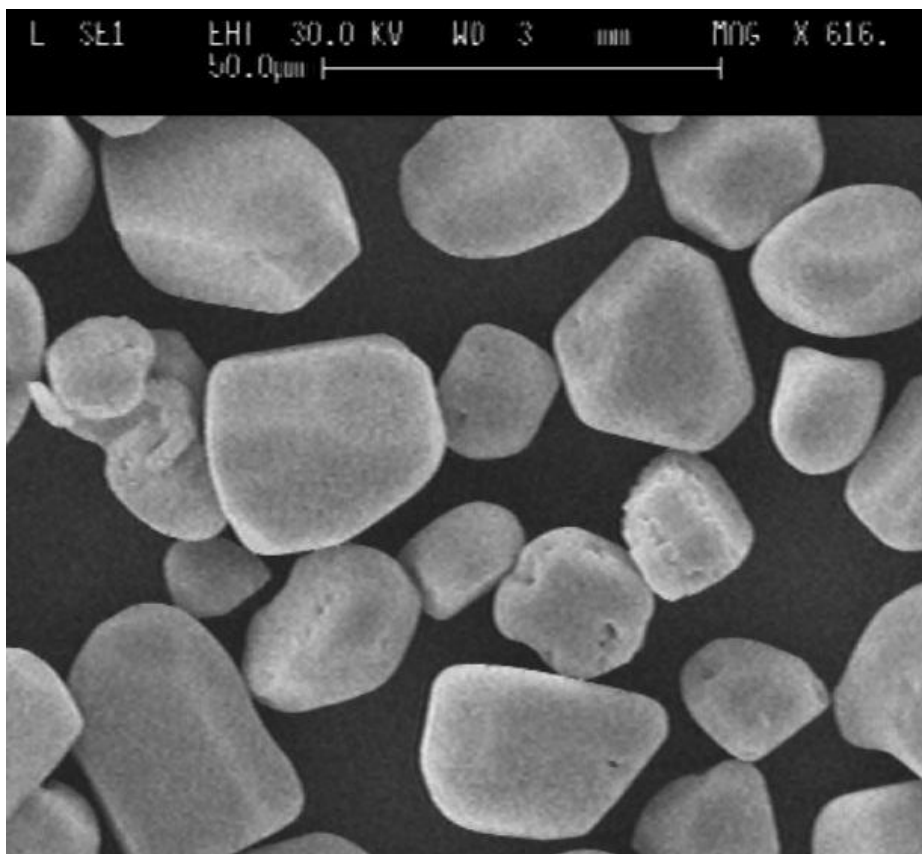


Figure 3.29: Scanning electron microscopy of Sylvania particles.

3.7 Discussion

The effect of firing conditions and procedures on the quality of phosphor materials produced is a rather complex issue to discuss. This is mainly because no specific mechanism for AC electroluminescent emission has ever been proposed with absolute certainty. As discussed earlier there are many hypotheses as to how this phenomenon occurs but the uncertainty makes it difficult to explain why particular synthetic routes yield materials different in terms of emission quality, considering that the materials are

constituted of zinc, sulfur and copper with cubic or hexagonal crystal structure. Hence further elaboration on this topic would require a detailed examination of the orientation of the lattice within each crystal structure as will be discussed in Chapter 7.

During the firing steps taken in synthesising these materials from the one micron precursor zinc sulfide particles, it is possible to end up producing larger particles resulting from the fusion of the precursors. As a result, particles will be formed which may have some constituent having their planes formed at different angles to the planes of other constituents within the particle. This is simply referred to as particles having fault in their crystal structure. So far it can be argued that aside from the luminescent centres, the direction of the crystal planes play a vital role in the phenomenon of ACEL.

3.8 Key observations

- The synthesis of zinc sulfide powders containing copper impurity should be conducted so that the copper is well distributed within the zinc sulfide crystal lattice.
- Firing the material under conditions where air/gas flow occurs at surface of the sample would lead to excessive loss of sulfur and hence rocky material is produced requiring extensive grinding
- Double firing of the phosphors where at first stage the doping impurity is introduced and at the second stage the flux is implemented produces brighter materials.
- Adding undoped amorphous zinc sulfide to fired/unfired copper doped zinc sulfide enhances the electroluminescent properties of the phosphor particles.
- Smaller particles tend to agglomerate when used for panel preparation compared to larger particles which tend to create a more homogenous film. Hence larger particles emission suffers less interference.

Chapter 4 : Thermal quenching of commercial AC-EL zinc sulfide phosphors

4.1 Introduction

The ZnS:Cu phosphors, co-doped with other activators such as Cl⁻ and Br⁻ exhibit electroluminescence (EL) under relatively low AC voltages; roughly two orders of magnitude smaller than is required for DC EL (Chapter 1). A feature of the ZnS:Cu phosphors is that copper has a very low solubility in zinc sulfide, and forms conducting Cu_xS precipitates in the zinc sulfide host above Cu concentrations of the order of 400–500 ppm. During the synthesis of the phosphors, when the phosphors are heated at temperatures above 850 °C, these precipitates form as the host crystals cool and transform into the cubic sphalerite phase⁶⁹.

The location of the copper atoms within the host lattice appears to be the fundamental factor in the mechanism of AC-electroluminescence. The crystal structure of zinc sulfide is composed of skeletal matrix of zinc and sulfur atoms and the precise location of the copper atoms within the crystal seems to directly affect the efficiency and the emission wavelength of the phosphor⁶⁷.

The electroluminescent emission spectra of ZnS:Cu.X (X = Cl, Br, I) ACEL phosphor powders exhibit blue-green emission. The spectra can be de-convoluted into four separate components. Primarily it is the amplitude of each component that changes with AC frequency, ranging from the blue region of the spectrum to the green region. Further investigation of this concept is undertaken to show how the EL spectra change after

annealing the phosphors as a function of temperatures followed by rapid quenching in liquid nitrogen.

A series of experiments were designed to alter the location or geometry, but not the actual amount of the copper atoms within the zinc sulfide lattice. In these tests, Sylvania made commercial ACEL zinc sulfide phosphor was heated to different temperatures and cooled very rapidly by placing in a crucible containing liquid nitrogen. A standard series of samples were tested in parallel by cooling the phosphor slowly in air rather than using rapid cooling in liquid nitrogen. Figure 4.1 shows the setup used to carry out these tests.

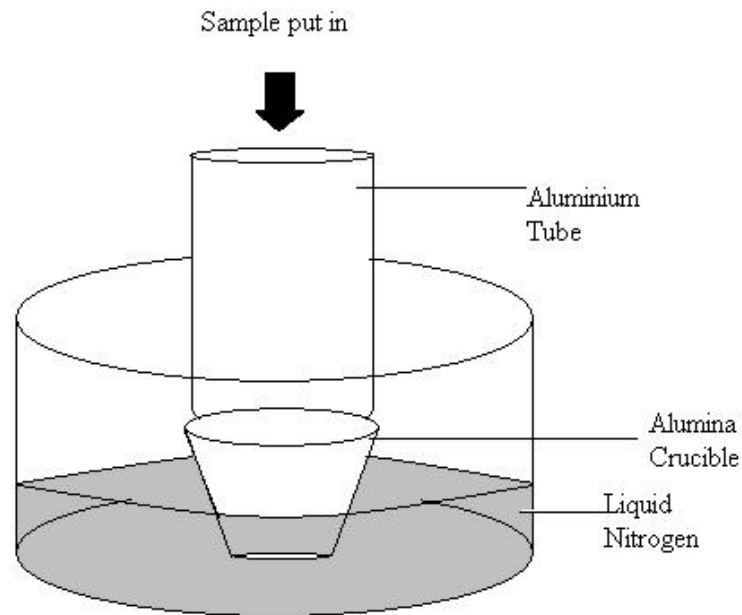


Figure 4.1 Instant cooling of samples with liquid nitrogen.

4.2 Quenching of the uncoated commercial samples

At one occasion during this research, in an attempt to create smaller particles by sudden cooling of heated (up to 200°C) commercial particles, an unexpected phenomenon was observed where they luminescent property of the material was altered by permanent shift of the emission wavelength toward green emission. To investigate this issue using commercially available Sylvania made ACEL coated^{xii} and uncoated phosphors as the source for sample preparation the following samples were prepared.

Using the uncoated source, 4 samples of 20 g were treated by subsequently heating them at temperatures of 200, 300, 400 and 500°C for 6 min. The samples were then placed directly in to the crucible containing liquid nitrogen. Each sample was recovered and placed in oven at 100°C until dry. The samples were designated GU200N, GU300N, GU400N and GU500N.

A repeat of the above procedure was carried out without liquid nitrogen cooling; the samples were, instead, cooled slowly in air. These were to be used as standard for comparison. They were designated GU200S, GU300S, GU400S and GU500S.

4.3 Quenching of the coated commercial samples

Phosphors are usually coated to extend their life-time by protecting them from atmospheric moisture. The coating material, usually aluminium oxide, encapsulates the phosphor particles creating a barrier between the lattice and the surrounding atmospheric

^{xii} Aluminium oxide is used to coat these phosphors to give them further protection against moisture.

conditions. Thus the coated samples could be used as controls for the tests in section 4.2. So, using identical phosphors from Sylvania, but coated, a repeat of the experimental procedure in section 4.2 was carried out. These samples prepared from the coated Sylvania phosphor source were designated as GC200N, GC300N, GC400N and GC500N; these samples were thermally shocked with liquid nitrogen. The coated samples designated GC200S, GC300S, GC400S & GC500S were cooled slowly in atmosphere.

4.4 Multiple thermal quenching of the uncoated samples

Considering the findings from the analysis of the samples thermally shocked at 500°C where the emission wavelength was shifted toward green it was important to investigate the possible effects that repeated thermal quenching would impose on the host lattice and hence the emission properties of the phosphor. Therefore, using the uncoated sample, 20g of the material was heated at 500°C and thermally shocked using the techniques described earlier, however the heating and cooling procedure was repeated up to four times and based on the number of repetitions the samples were identified by designating them as GU500R2, R3 and R4 to indicate how many times they were heated and rapidly cooled.

4.5 Time related thermal quenching of the samples

In all of the above experiments the period of time for which the sample was heated at the designated temperature was 360 seconds. It was hypothesized that during the heating procedure the copper atoms/holes, which form the core of the luminescent centres, might undergo a form of migration through the lattice due to high vibrational energy within the lattice. The sudden change in surrounding temperature i.e. sudden cooling with liquid nitrogen would stabilise the copper atoms/holes at new locations within the zinc sulfide lattice from their original position. This would imply that the longer the heating time, the more distant the copper atoms would relocate to their new positions and hence form different luminescent centre geometries and alter the emission properties of the phosphor. So, choosing the 500°C heating temperature and the uncoated phosphor source, a series of tests were carried out whereby the material was heated for periods of 20, 40 and 60 minutes and then thermally shocked via liquid nitrogen. These samples were designated as GU500T20N, GU500T40N and GU500T60N, respectively.

4.6 Results

4.6.1 Peak emission

ACEL panels made from the thermally shocked samples were analysed by an AC drive providing 400 Hz frequency and the EL emissions were analysed at 113 and 180 V, respectively. These experiments were conducted to ensure that the voltage of the drive had no effect on the peak emission spectra of the EL panels made from these samples. The dominant wavelength of the emission (i.e. the peak of the emission band) is the factor which was analysed for the purpose of this work. However, the driving voltage does affect the emission spectra of the material (as shown in the data in Figure 4.2).

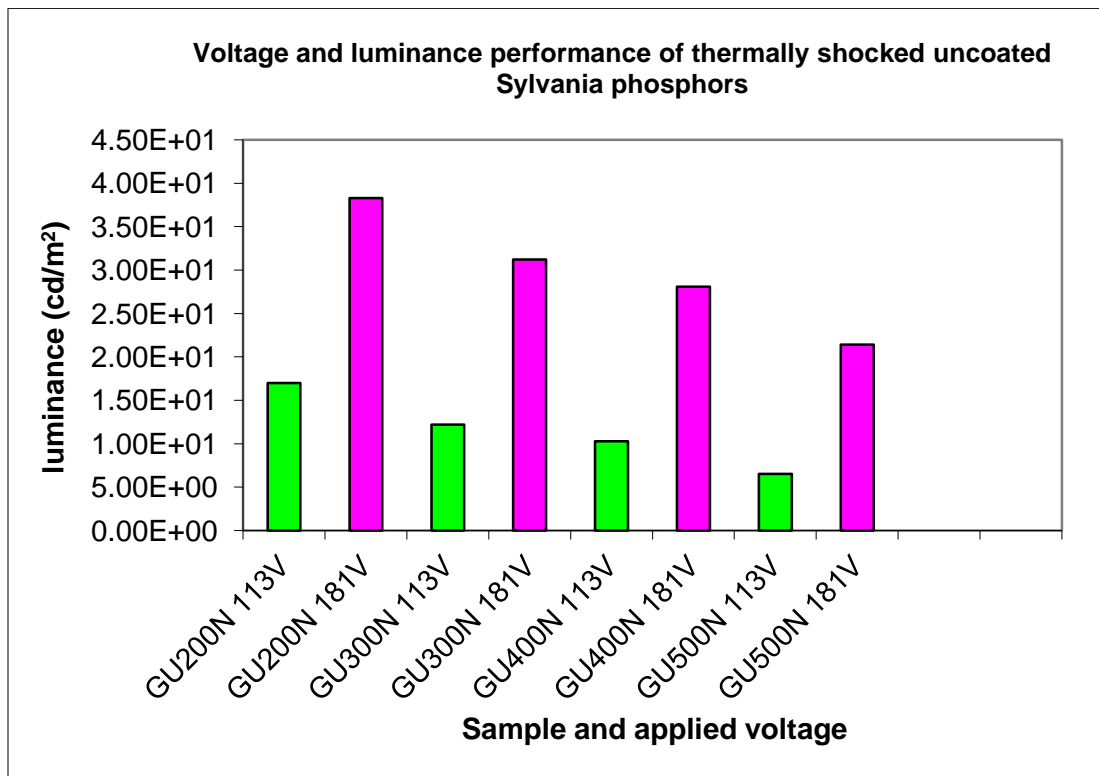


Figure 4.2: The relationship between luminance and the associated driving voltage (113V and 181V) of the nitrogen shock treated samples at 400Hz frequency. Thermal shocking reduces the overall emission of the phosphors.

However, as demonstrated in the data in Figure 4.3, it can be observed that the dominant wavelegh of the EL emission has shifted towards the green region of the spectrum (higher wavelength), indicating that the heat shock treatment does affect the material in a way that the emission properties of the material is consequently affected.



Figure 4.3: Dominant emission wavelength of the nitrogen shock treated samples at (113V and 181V) under 400Hz frequency compared to that of an untreated sample. Dominant wavelength is shifted toward a longer wavelength.

4.6.2 ACEL emission spectrum of thermal shock treated and untreated uncoated phosphors

The emission spectra of the prepared samples were obtained, using standard panels made of the samples, by a jeti spectroradiometer. Figure 4.4 displays the data obtained for heat shock treated, as described, and standard uncoated Sylvania samples that were allowed to cool steadily after being heated.

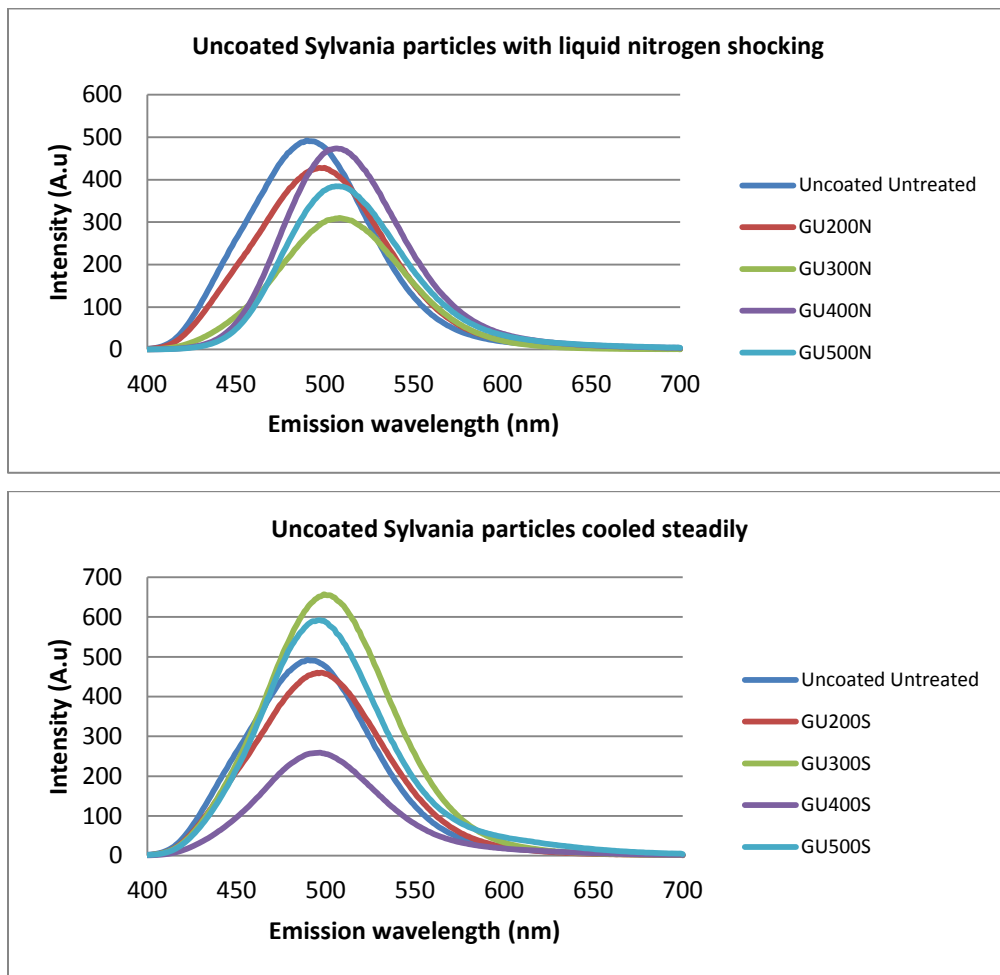


Figure 4.4: ACEL emission spectrum of uncoated samples (liquid nitrogen shocked and cooled steadily) at 181V and 400Hz. Quenched samples demonstrate both change to spectrum and intensity while slowly cooled samples only demonstrate reduction in emission intensity.

4.6.3 ACEL emission spectrum of thermal shock treated and untreated coated phosphors

Here the tests carried out in section 4.6.2 were repeated, but using coated Sylvania samples instead. These results are presented in Figure 4.5.

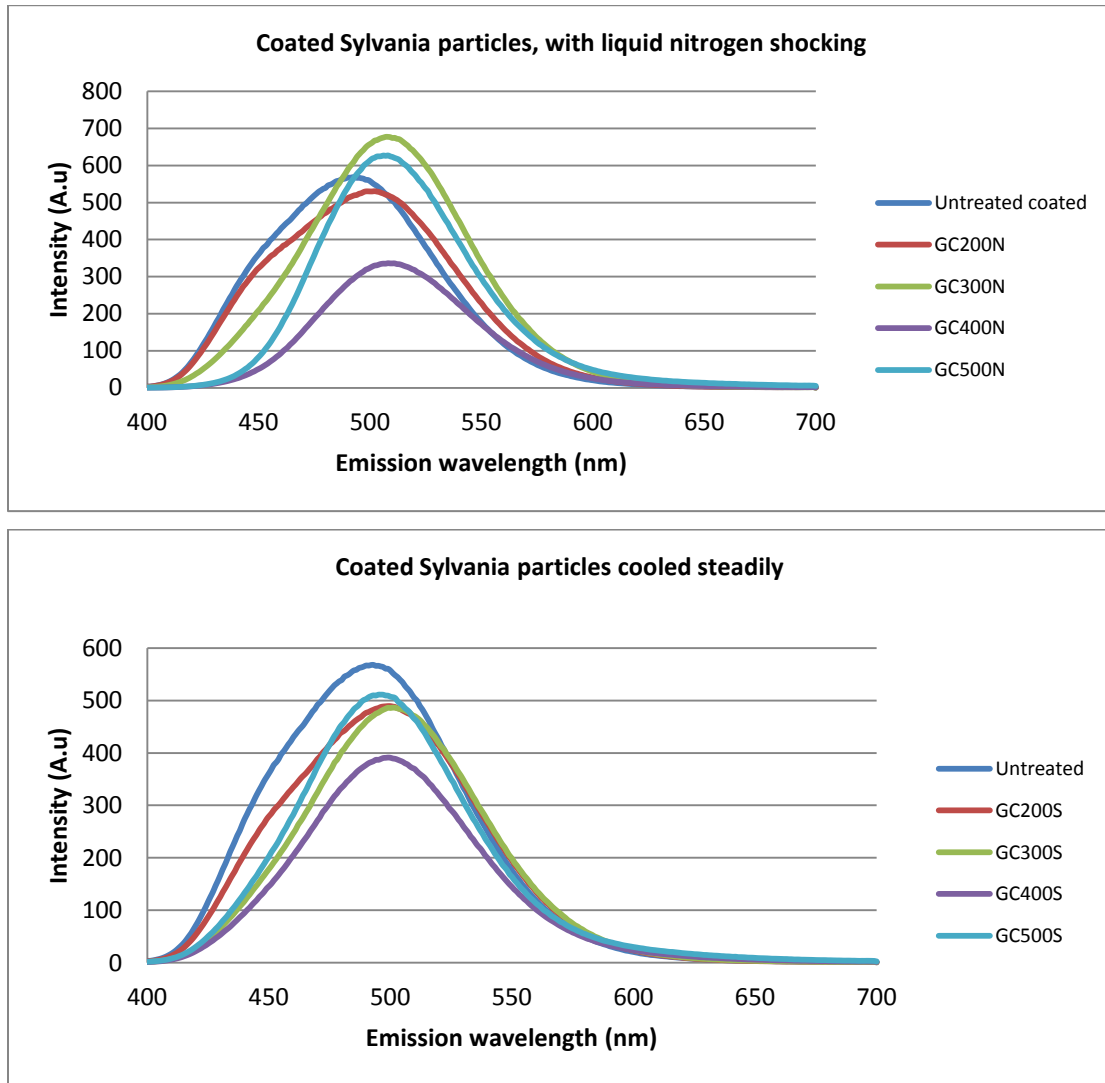


Figure 4.5: ACEL emission spectrum of coated samples (liquid nitrogen shocked and cooled steadily) at 181V and 400Hz. Quenched samples demonstrate both change to spectrum and intensity whileslowly cooled samples only demonstrate redustion in emission intensity.

4.6.4 Emission properties of samples under multiple thermal quenching

The data in Figures 4.6 and 4.7 show the emission properties of samples which were heat shock treated multiple times. These findings clearly suggest the shift in dominant emission peak occurs only after the first firing and subsequent firing only affects the emission efficiency of the material.

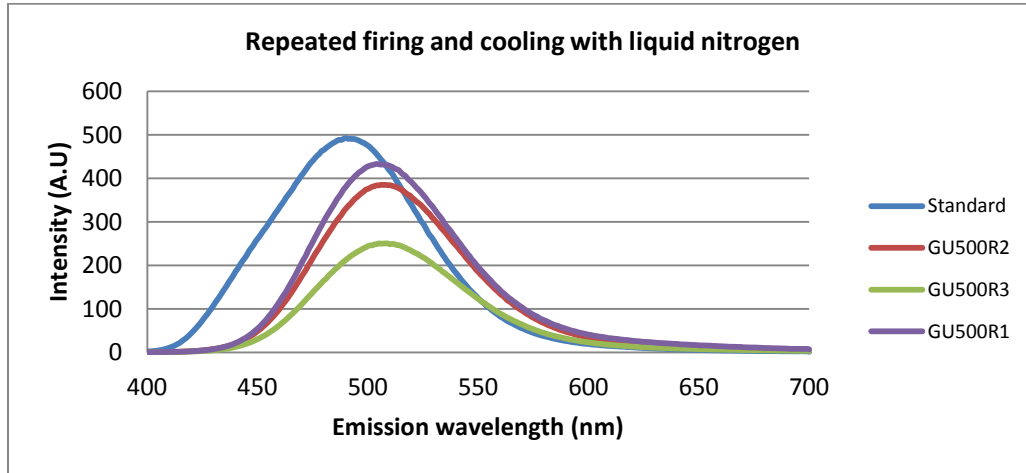


Figure 4.6: ACEL emission spectrum of uncoated samples repeatedly (3 times) heated to 500°C and rapidly cooled by liquid nitrogen shocked at 181V and 400 Hz. Repeated firing does not alter the dominant wavelength but reduces the intensity of emission.

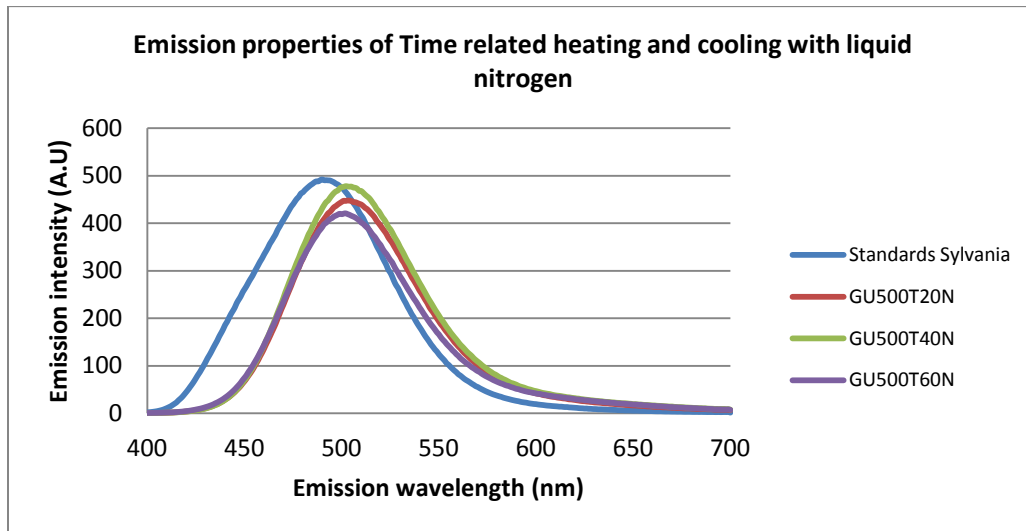


Figure 4.7: ACEL emission spectrum of uncoated samples heated to 500°C for 20, 40 and 60 minutes and rapidly cooled by liquid nitrogen at 181V and 400 Hz. Extended heating time does not alter the amount of dominant wavelength shift but reduces the intensity.

4.7 X-ray powder diffraction (XRD) analysis of the samples

4.7.1 Basic X-ray analysis

The uncoated and coated samples were analysed using x-ray powder diffraction to investigate possible structural changes as a result of the LN shocking procedure. The main focus of investigation was a possible shift of the main peaks associated with the zinc sulfide crystal lattice as an indicator of alteration in crystal structure.

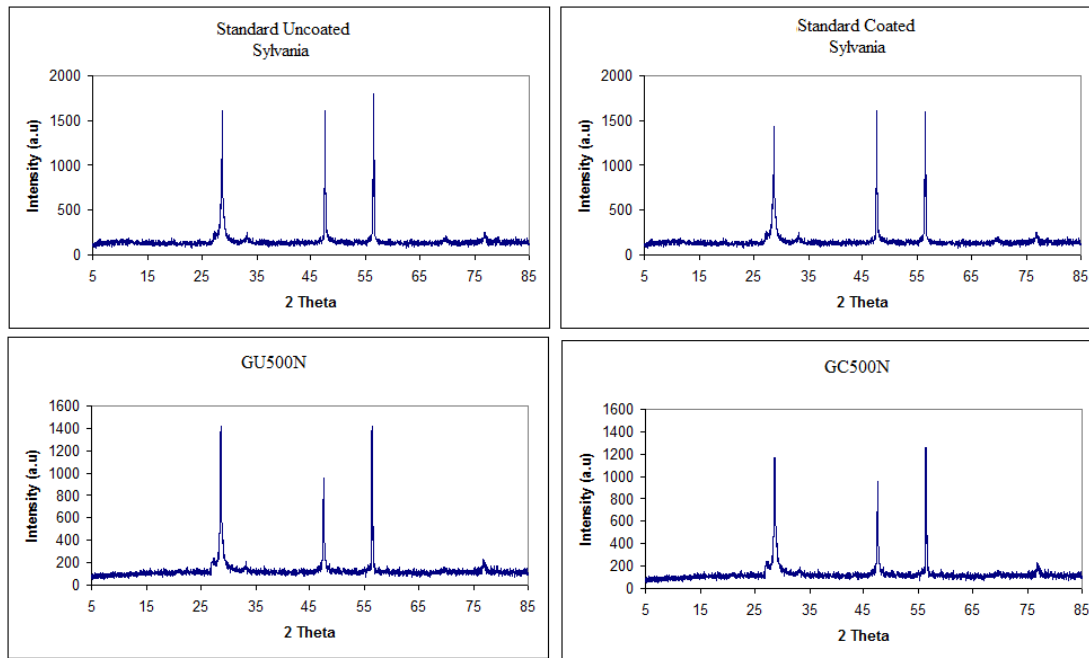


Figure 4.8: XRD analysis of coated and uncoated Sylvania phosphors treated at 500°C followed by nitrogen shocking compared to untreated standard sample. The cubic crystal structure of these samples is unaffected.

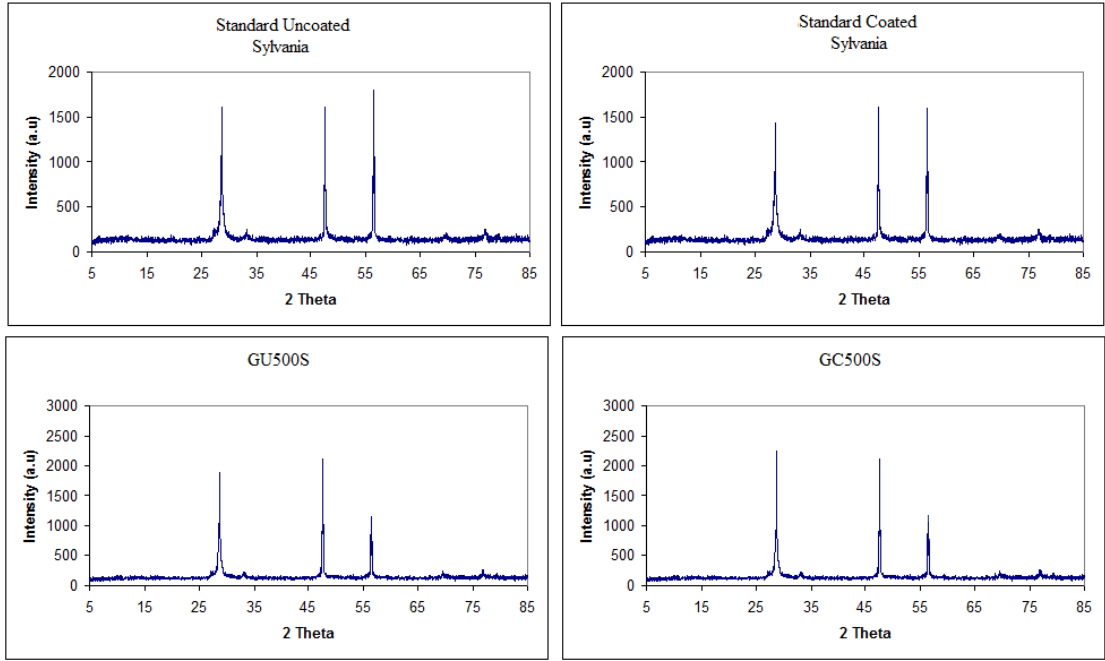


Figure 4.9: XRD analysis of coated and uncoated Sylvania phosphors treated at 500°C and cooled steadily compared to untreated standard sample. The cubic crystal structure of these samples is unaffected.

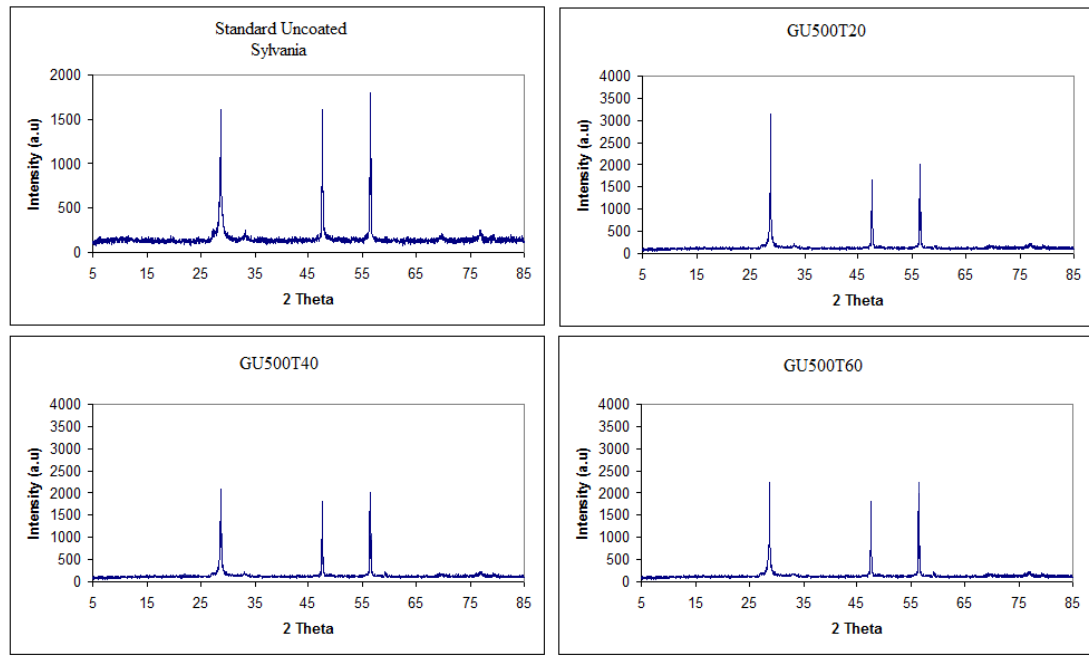


Figure 4.10: XRD analysis of uncoated Sylvania phosphors heated at 500°C for 20, 40 and 60 minutes and cooled by liquid nitrogen compared to untreated standard sample. The cubic crystal structure of these samples is unaffected.

4.7.2 The crystal structure of quenched and in-field electroluminescent phosphors investigated by synchrotron x-rays

As stated earlier, the commonly used phosphors for ACEL give blue-green emissions that can be de-convoluted into multiple components, two in the blue region of the spectrum and the others in the green region⁷⁰. The blue emission has been assigned to a blue copper transition originating from a copper centre that is surrounded tetrahedrally by three sulfide ions and a vacant sulfide site in the zinc sulfide lattice (where Zn^{2+} is replaced by copper in a lattice site). The green emission has been assigned to a similar copper site but instead of a sulfur vacancy there is a chloride ion that makes up the tetrahedral coordination. It has long been recognised that disorder (stacking faults) needs to be introduced into the crystal structure of the material and maximum use of the disorder should be made in order to produce a bright EL phosphor⁷¹. Understanding the ACEL mechanism should lead to improved phosphors that offer higher device efficiency and in this section experiments were carried out to make a comparison between the quenched (GU400N) and un-quenched (GU400S) phosphors using synchrotron radiation x-ray powder diffraction (XRPD) ($\lambda=0.828692\text{\AA}$) and x-ray absorption spectroscopy to further understand the luminescent centers.

4.7.2.1 In field x-ray analysis of phosphors

Powder ACEL panels were prepared on indium tin oxide coated PET as the transparent electrode substrate. The substrate was screen printed with a phosphor layer that comprised of un-encapsulated ZnS:Cu ACEL phosphor powder (Sylvania) and ethyl cellulose binder dissolved in a hexanol solution (Sigma Aldrich, UK) and dried in an

oven at 130°C for 10 minutes. Orgacon ([PEDOT/PSS], Agfa Materials, UK) was screen printed to form the non-transparent electrode after drying in an oven at 130°C for 10 minutes. Conductive aluminium tape was attached to each electrode and the light output of the panel measured by the Jetti specbos 1201 spectrometer as 48.3 cdm^{-2} at 150V RMS and 2 kHz. The panel was tested at 113 V and 400 Hz for the XRPD measurement. Powder samples were mounted into 0.7 mm capillary tubes and data collected using the BL-I11 line at the Diamond Light Source⁷². Extended X-Ray Absorption Fine Structure (EXAFS) measurements were conducted in air at room temperature, using the KMC2 graded double-crystal monochromator of the electron storage ring at BESSY-II in Berlin. Spectra were recorded at the Zn-K-edge, using an ionization chamber in transmission mode. The maximum flux of the beam line at an energy of 8.5 KeV is on the order of 10^{10} photons/sec. The XRPD data for the samples is presented in Figure 4.11. The XAS analysis of the samples does not indicate a major alteration of the crystallographic structure between the two samples (Figure 4.12). However, the data indicate that the electronic structure has altered due to a change in Zn K edge shape. The XRPD data of the sample under an electric field is presented in Figure 4.13.

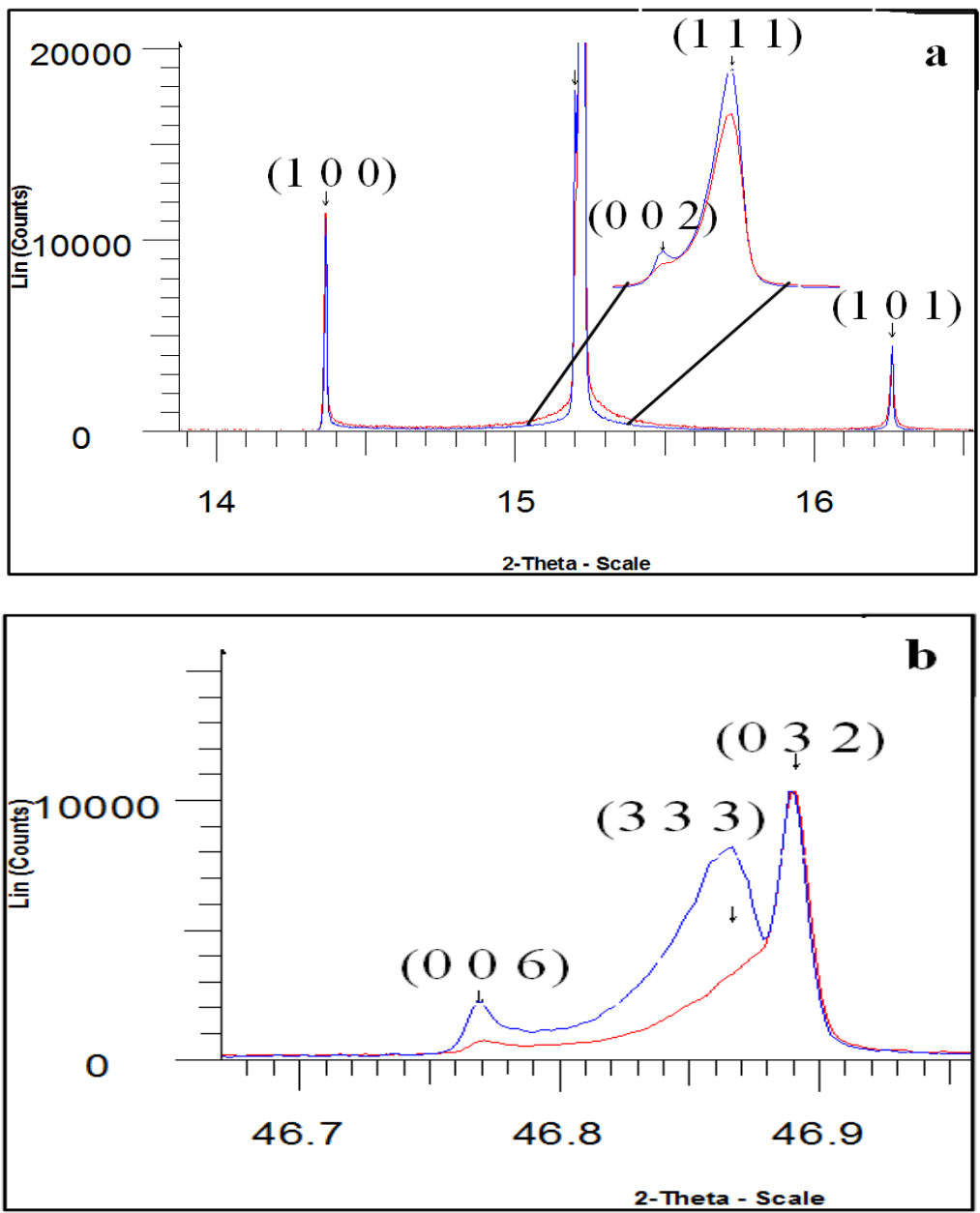


Figure 4.11: XRPD of the ACEL phosphors (GU400S-blue and GU400N-red line). The cubic (333) lattice parameter seems to be reduced extensively.

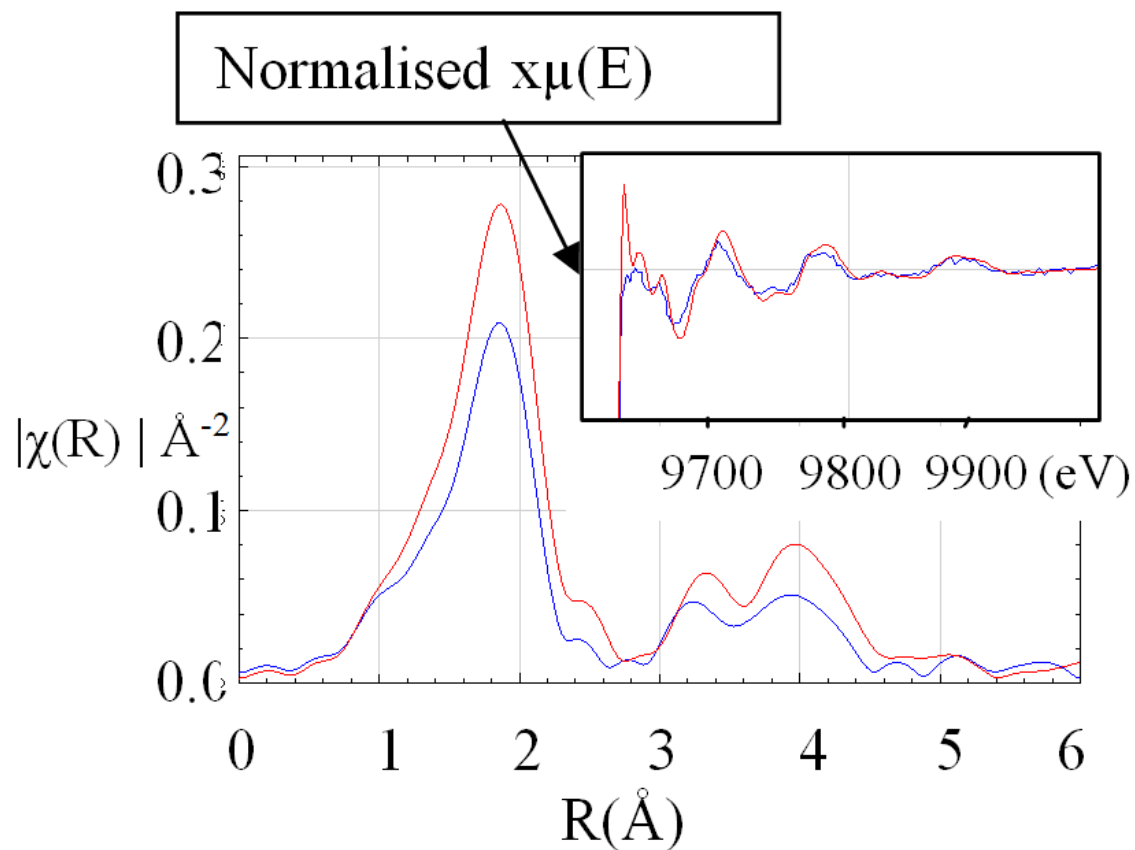


Figure 4.12: XAS data in R and E (inset scale). The Zn K-edge XAS data do not allow for an easy understanding of the subtle crystallographic differences between quenched and non-quenched specimens. However, the data indicate that the electronic structure has altered due to changes in Zn K-edge shape.

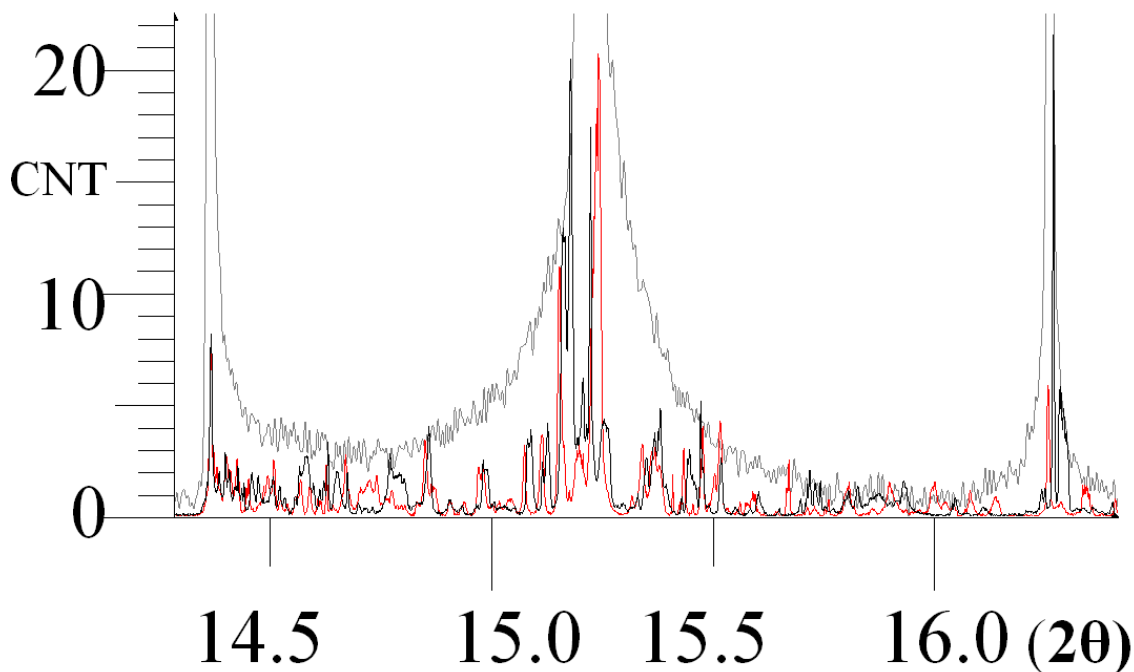


Figure 4.13: Expansion of XRPD pattern of EL phosphor deposited in the EL panel. The orange line is 'off' and the black line shows the panel in operation. The top grey line shows the broad powder pattern observed in a capillary. All the peaks do shift when the field is applied.

4.7.2.2 X-ray analysis of the phosphor materials under controlled thermal conditions

X-ray powder diffraction analysis of quenched and untreated standard Sylvania phosphors were carried out using the Beamline I11 of the Diamond synchrotron. Capillary tube sample holders were used to ensure each analysis was performed using the same quantity of material and rule out the effects arising from different thermal expansion factors of the sample holder and the sample itself. The source of heat during the analysis was the hot air flow technique employed at Beamline I11. These tests were carried out to investigate the effect of the temperature and quenching on the crystallographic configuration of the samples. The equipment at Diamond allowed the

sample to be heated up to 400°C while being analysed. Using the uncoated standard Sylvania phosphors, x-ray powder diffraction analysis was carried out at room temperature, 100°C, 200°C and 400°C. The diffraction pattern was analysed in order to evaluate any displacement of the crystal plane peaks. The quenched sample (heated to 400°C and cooled rapidly) was compared to a standard sample for analysis of the intensity of peaks associated with various cubic or hexagonal crystal planes. The change in temperature seems to be shifting the peaks of almost all the planes to the left but only to a slight degree. This can be seen by careful analysis of the data, as presented in Figures 4.14 and 4.15.

Figures 4.16 and 4.17 demonstrate the alteration in intensity of the peaks related to certain crystal planes after quenching the uncoated sample at 400°C.

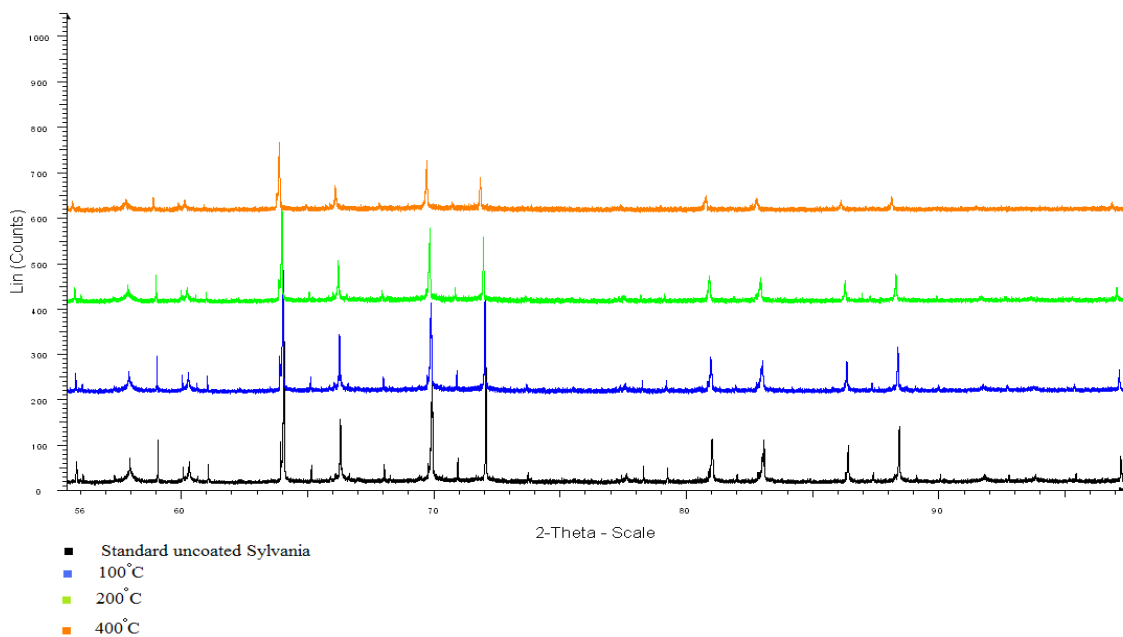
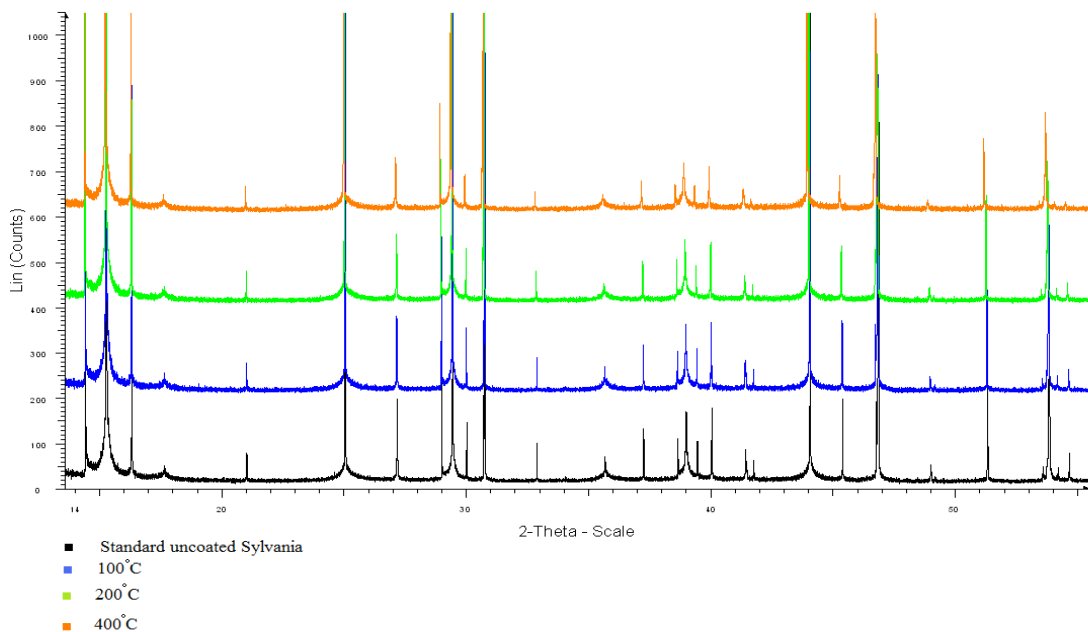
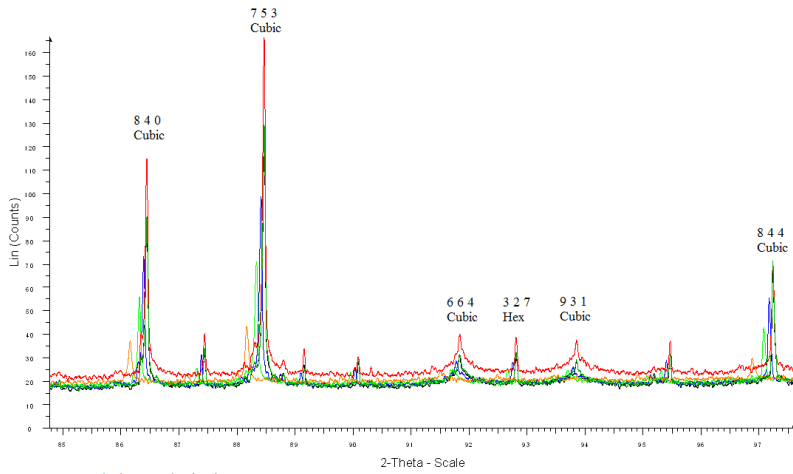
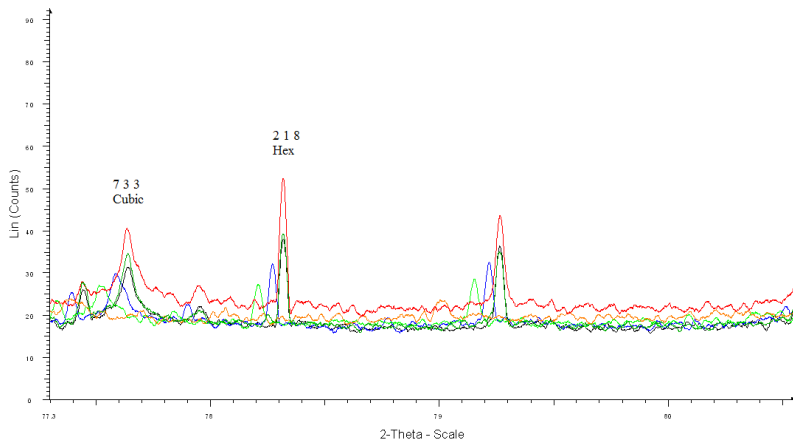
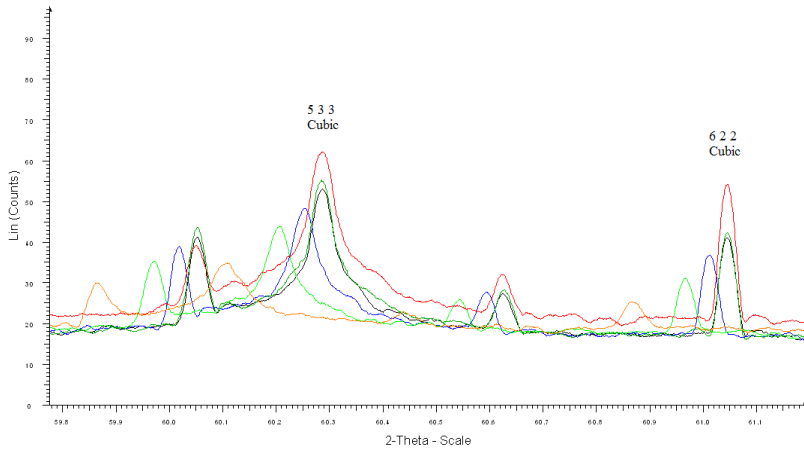


Figure 4.14: X-ray powder diffraction analysis of uncoated Sylvania phosphors at room temperature, 100°C, 200°C and 400°C. All peaks are shifted to the left when analysis is carried out at higher temperatures.



- Standard uncoated Sylvania
- 100°C
- 200°C
- 400°C
- Heated to 400°C and cooled slowly
- Heated to 400°C and quenched

Figure 4.15: X-ray powder diffraction analysis of uncoated Sylvania phosphors at room temperature, 100°C, 200°C and 400°C compared to quenched and steadily cooled samples, demonstrating the crystal planes shifting when the sample is heated.

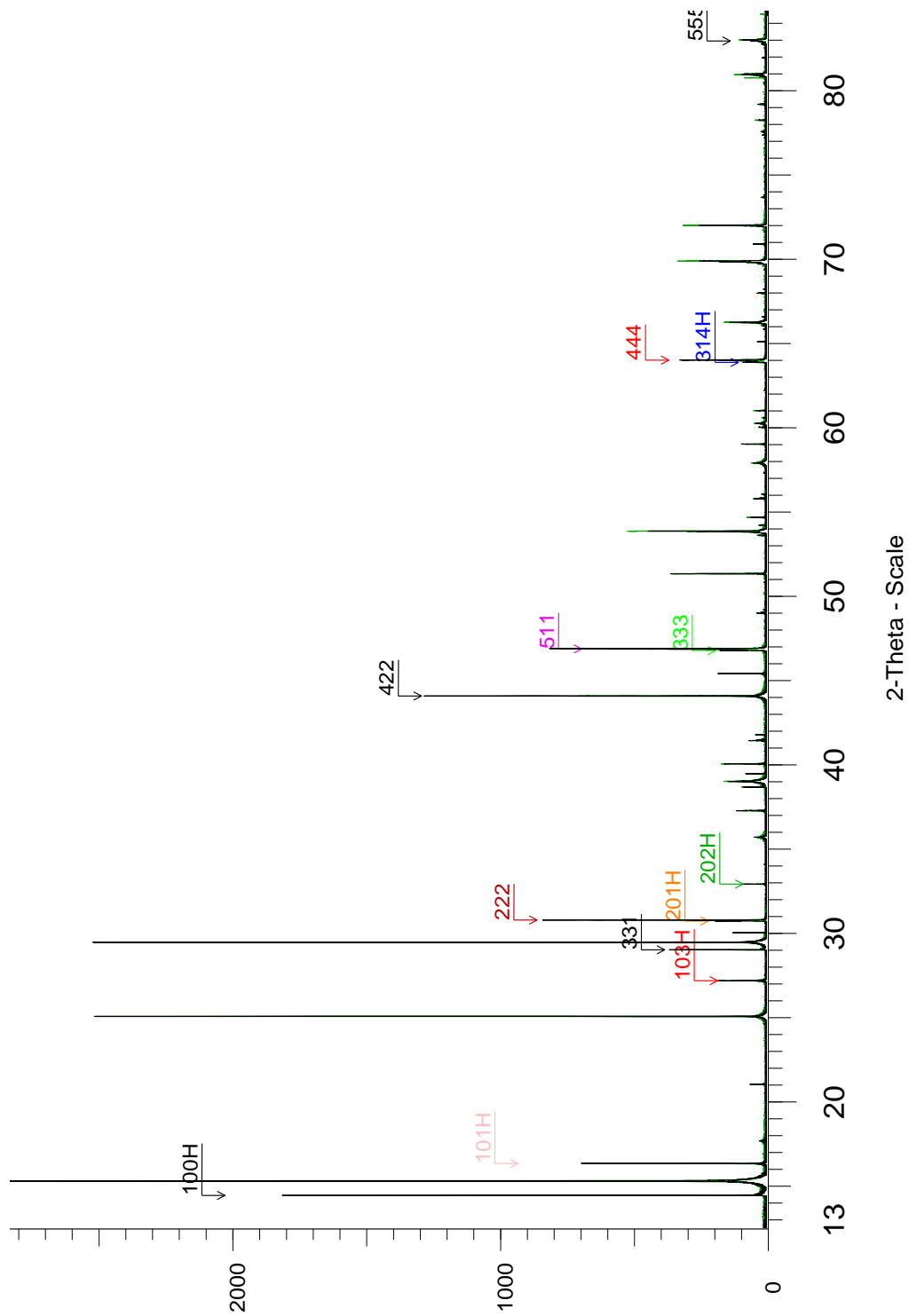
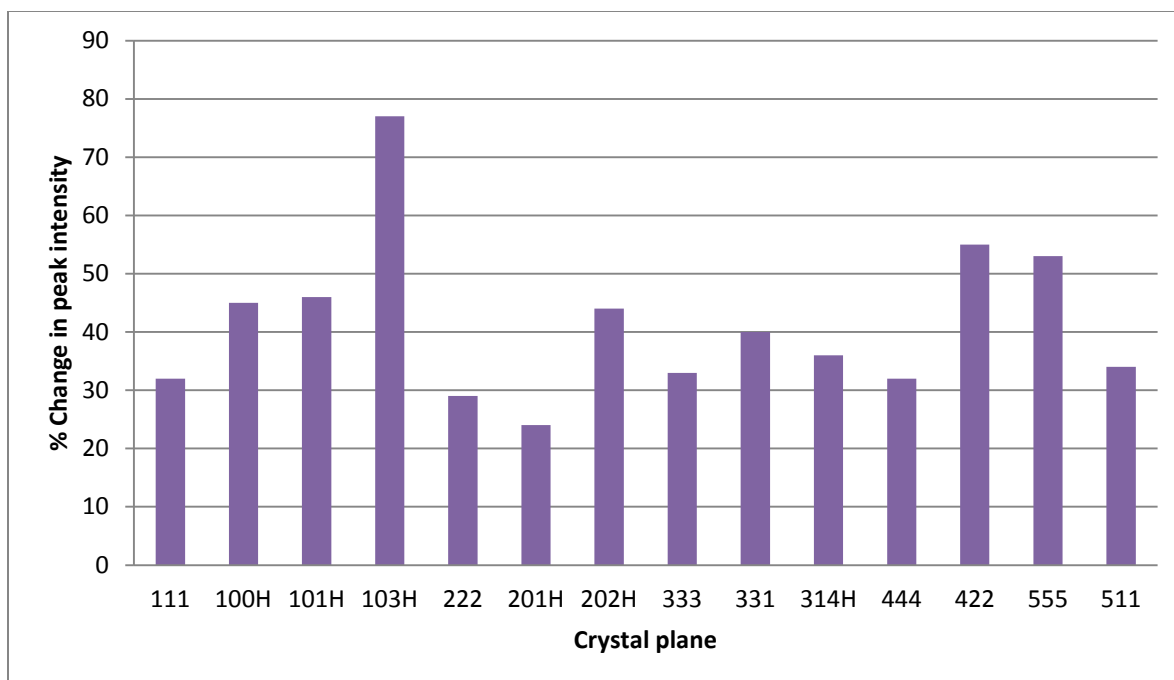


Figure 4.16: Alternation in intensity of peaks related to certain crystal planes after quenching the uncoated Sylvania sample at 400°C.



Plane	111	100H	101H	103H	222	201H	202H	333	331	314H	444	422	555	511
Standard	17725	1818	697	181	840	192	86	175	366	89	325	1284	60	678
Quenched	5834	824	325	139	249	47	38	58	146	32	104	707	32	235
%	32	45	46	77	29	24	44	33	40	36	32	55	53	34

Figure 4.17: Demonstration of the percentage change in peak intensity of the crystal planes after the standard uncoated Sylvania phosphor is quenched at 400°C. H prefix indicates crystal planes related to hexagonal crystal form, otherwise cubic. Various peaks are reduced in an irregular fashion.

4.8 Discussion

The results obtained from thermal quenching analysis clearly indicate that the quenching of the material alters its electroluminescent properties along with photoluminescent properties as reported elsewhere⁷³. However the XRD analysis of the sample does not indicate any observable change in terms of the crystal structure of the material. This would suggest that the quenching is only affecting the luminescent centres within the lattice. It is also clear that the importance of the temperature at which the sample is quenched is significant within the range of about 200-300°C. The results also clearly demonstrate that the emission intensity of the samples is decreased as a result of the thermal quenching procedure, which again indicates that the luminescent centres are directly affected by the thermal quenching process.

However, it can also be argued that certain luminescent centres, particularly those emitting at lower wavelengths are deteriorated by thermal quenching while those emitting at longer wavelength are not. This would lead to the changes observed in the dominant wavelength and lower emission intensity observed from this study. It seems from this study that the blue centres are hence vulnerable to the thermal quenching procedure carried out due to the role that the interstitial Cu^+ species play in this mechanism. The interstitial Cu^+ is not as stable in its location within the lattice compared to a substitutional Cu^+ and hence a thermal shock is prone to effect its location or association with its surrounding element. The green emission centre, however, seems unaffected. A comparison between the quenched and un-quenched phosphors using XRPD ($\lambda=0.828692\text{\AA}$) and x-ray absorption spectroscopy (XAS) have been undertaken. The XRPD results (Figure 4.11 a) shows that the expected highly faulted structure is observed

with excellent resolution out to 150° {or to the (12 2 2)} of the Sphalerite phase. The quenched sample compared to the reference sample shows a large change in peak ratios between 46.7° and 46.9° , thought to correspond to the Wurtzite $(0' 0 6), (0' 3' 2)$ and Sphalerite $(3 3 3)/(5 1 1)$ peaks. Hence a large proportion of this diffraction is lost from the material upon rapid quenching but not when the material is allowed to cool slowly (the heated sample showed reversible thermal expansion). Figure 4.11 shows the separation of the sphalerite (1 1 1) and wurtzite (0 0 2) diffraction lines with very broad diffraction intensity shown whereby diffraction intensity is observed between the three peaks. In Figure 4.11b the region between 46.7° and 46.9° is shown which corresponds to the wurtzite and sphalerite lines indicated. On quenching the sphalerite intensity (333) is dramatically reduced. The Zn K edge XAS data (Figure 4.12) does not allow for an easy understanding of the subtle crystallographic differences between quenched and unheated specimens. However it gives an indication that the electronic structure has altered due to changes in Zn K-edge shape. These findings are further discussed in Chapter 7.

4.9 Key observations

- Thermal quenching of zinc sulfide phosphors doped with copper alters the peak emission of the material by ~10nm toward the green as a result of blue emission reduction.
- The overall emission property of the materials is reduced after thermal quenching.
- Repeated quenching will not result in further peak emission shifting but will continue to reduce the overall emission intensity.
- XAS analysis indicates that quenching does alter the electronic environment of zinc atoms within the crystal.
- XRPD analysis of the thermally quenched samples indicate that the overall crystal structure of the material does not change, however various crystallographic planes ,both hexagonal and cubic, of the material demonstrate lower intensity when evaluated by XRPD.
- XRPD analysis of an ACEL panel under electric field demonstrates shifting of the crystal planes indicating that the field imposes strains on the crystal planes.

Chapter 5 : Copper diffusion in to zinc sulfide lattice

5.1 Introduction

As discussed in Chapter 4, the copper ions which act as the activator in the zinc sulfide lattice form the luminescent centres responsible for the emission properties of these materials. It is assumed that the Cu atoms are distributed within the zinc sulfide lattice evenly and at very low concentration compared to the Zn atoms. However, there are multiple approaches in terms of synthesizing these materials. This study was carried out to gain an insight into where the Cu atoms are located within each crystal and at what concentration ratios compared to the initial quantity. The core of the study involved digesting commercial Sylvania EL phosphor materials using *aqua regia* (50:50 mixture v/v solution of nitric and hydrochloric acid) and analysing the solution for evaluation of the copper content. Also a study was carried out to map the distribution of the Cu species within the lattice by multiple stage digestion of commercial ZnS:Cu particles.

5.2 Preparation of the samples designed for copper content analysis via ICP-MS

The ICP-MS was calibrated using standard solutions of zinc and copper with exact amount of *aqua regia* present in samples to be analysed. The samples to be analysed were prepared using the following standard procedure. 10 g of ACEL zinc sulfide phosphor sample was dissolved in 10 ml of *aqua regia* and left to settle for 24 hours. After the samples were totally dissolved, 22 ml of deionised water was added to bring the total volume to 32 ml. Since the *aqua regia* solution creates gas (nitrosyl chloride), this was done to prevent the formation of gas which would affect the precision volumetric measurement of the solution by Gilson pipettes. This solution was then diluted tenfold (in volume) using deionised water. The final dilution was used for the ICP-MS analysis. Data obtained from the ICP-MS studies were used to calculate the concentration of copper and zinc for each sample and were used to calculate the actual Cu/Zn % molar ratio in the prepared samples. Using the ratios of copper to zinc, rather than the actual values obtained, makes the interpretation of the obtained data easier.

5.3 Copper content analysis

A series of experiments were designed to gain an insight into the quantity of copper present in the samples produced. ICP-MS was used for this purpose. It was apparent that the actual flux content, length of time used in the firing and the firing temperature had a direct impact on the copper levels in the lattice and hence these experiments were designed so that all the above factors could be monitored during the analysis. A set of newly prepared samples were prepared for this experiment.

5.3.1 Firing period and copper diffusion into the lattice

As part of this research a technique was developed for producing ZnS:Cu materials whereby brighter EL phosphors were produced in comparison to the conventional technique initially used during this research. This involved a double firing procedure where the precursor materials; zinc sulfide and the doping copper were originally fired without any flux i.e. sodium chloride and hence only contained the doping element Cu and ZnS, and then it was re-fired together with the sodium chloride flux. The period of the initial firing is important in terms of luminance property of the phosphor, so using ICP-MS analysis the effect of the initial firing period was investigated to gain an insight into the level of copper diffusion into the lattice in relation to the period of initial firing. A set of tests were designed for this purpose: **Am** samples were prepared using a sample with initial copper content of 1.2 moles of copper per 100 moles of zinc (1.2% molar ratio) which was initially fired for a periods of 45 min and 2 hours and a second series of

samples; **D** sample with initial copper content of 0.6% molar ratio with initial firing periods of 20, 40, 60 and 80 min.

5.3.1.1 Initial copper content of 1.2%

A solution of CuNO_3 was prepared and added to a quantity of commercial grade zinc sulfide from Sylvania (Figure 5.1) to prepare a precursor containing 1.2% molar ratio of Cu to Zn after drying, this was named source alfa.

Am1: 20 g of source alfa was fired at 850°C for a period of 45 min. Then it was cooled in air and mixed with 20% weight of sodium chloride flux and re-fired at 850°C for a period of 1 hr.

Am2: 20g of source alfa was fired at 850°C for a period of 2 hours. Then it was cooled and mixed with 20% weight of sodium chloride flux and re-fired at 850°C for a period of 1 hr.

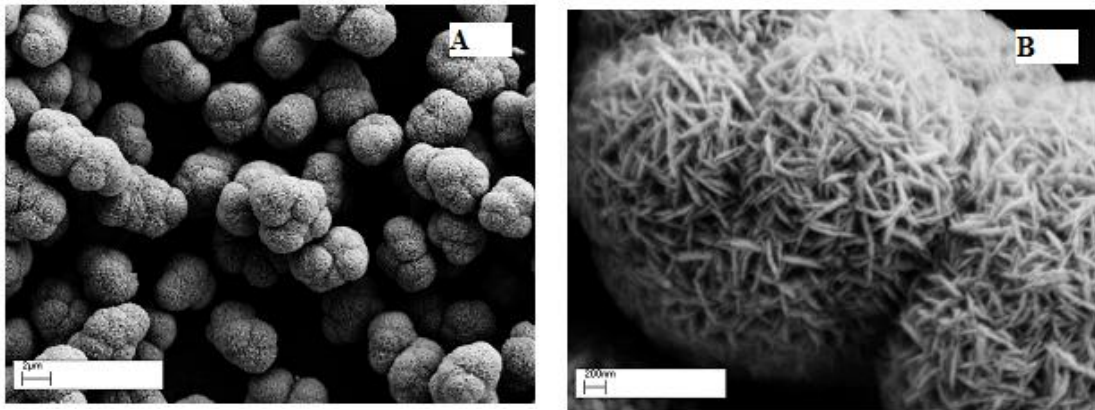


Figure 5.1: Sylvania zinc sulfide particles. The particles are composed of nanorods that agglomerate to form the 1.5 micrometer particles.

The samples were prepared for ICP-MS analysis as described; the data obtained are presented in Table 5.1. The ICP-MS provides data in the form of mg/l and hence these data had to be converted to moles and a plot of the actual Cu/Zn molar ratio is presented in Figure 5.2 and shown in Table 5.1.

Sample	Cu(mg/ml)	Zn (mg/ml)
Am1	0.377	251
Am2	0.362	254

Table 5.1: The amount of Cu and Zn found in Am1 and Am2 samples based on the ICP-MS results.

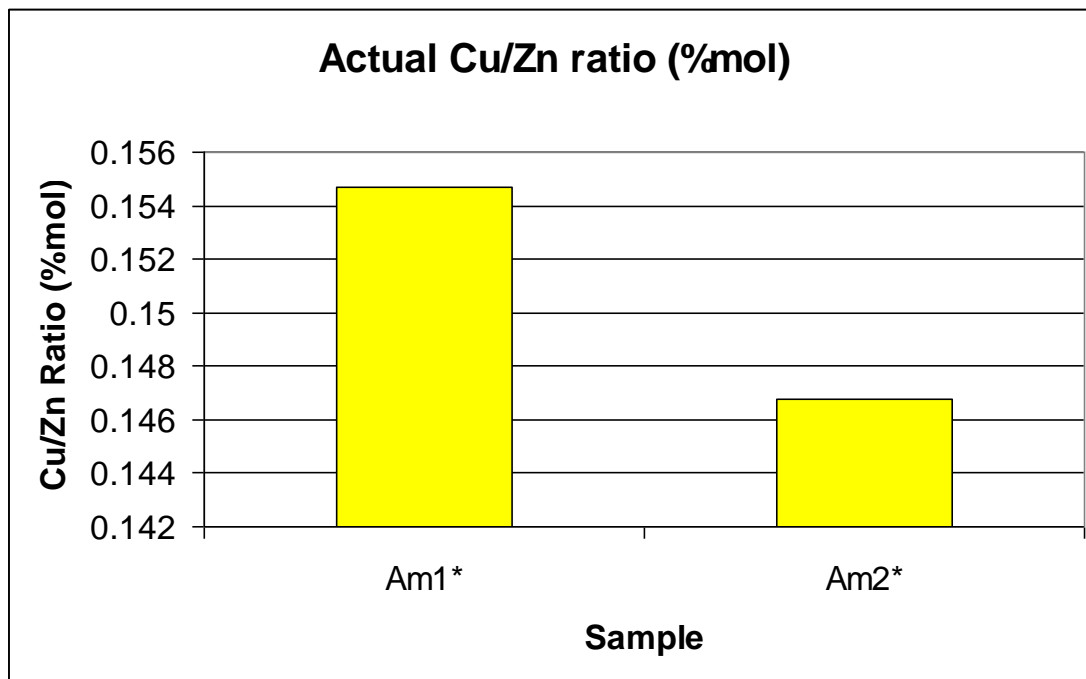


Figure 5.2: The ratio of Cu/Zn in terms of moles of copper per 100 moles of zinc (% molar) based on results from ICP-MS analysis.

5.3.1.2 Analysis of samples containing 0.6% copper

Four samples were prepared for this analysis: D20, 40, 60 and 80 samples which contained 0.6% molar ratio of the doping element.

Four separate 20 g portions of source Delta^{xiii} were fired for periods of 20, 40, 60 and 80 minutes at 850°C and after cooling were ground and re-fired at 850°C with 20% by weight of sodium chloride for a period of 1 hr.

The samples were prepared for ICP-MS analysis as described in section 5.2. The ICP-MS provides data in the form of mg/l and hence these data had to be converted to moles and a plot of the actual Cu/Zn molar ratio is presented in Figure 5.3 and the data in Table 5.2.

Sample	(Cu) Concentration (mg/l)	(Zn) Concentration (mg/l)
D20	0.251	240
D40	0.300	281
D60	0.238	248
D80	0.239	267

Table 5.2: The amount of Cu and Zn found in D20-80 samples based on the ICP-MS results.

^{xiii} Delta: Commercial grade ZnS from Sylvania was added to CuNO₃ Solution and then dried. The material contained 0.6% molar ratio of Cu to Zn.

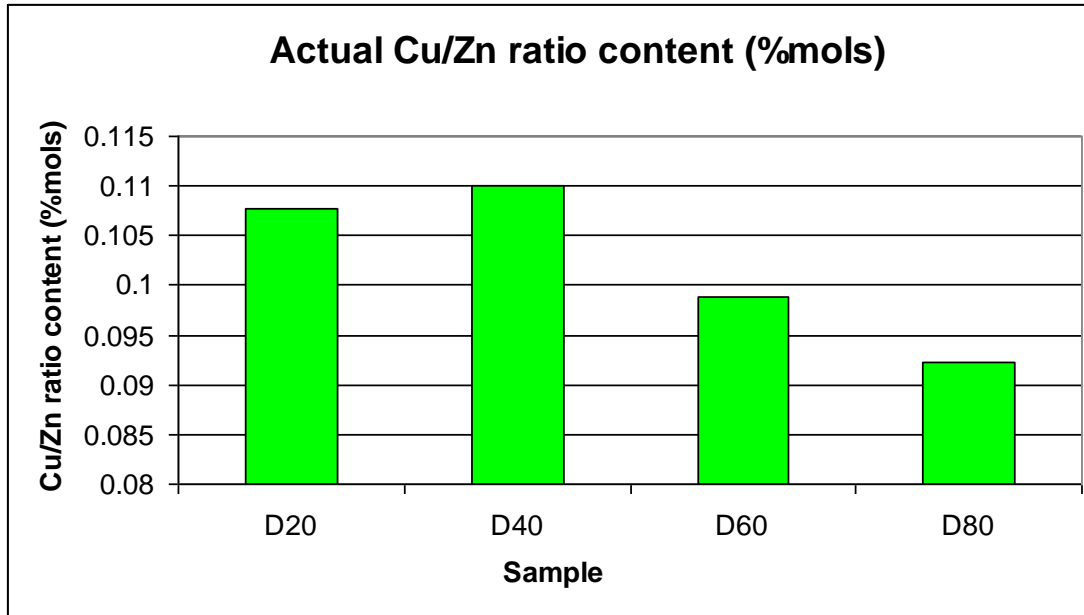


Figure 5.3: The ratio of Cu/Zn in terms of molar % based on results from ICP-MS analyses for D20-80 samples. D40 samples contain the highest level of copper impurity.

5.3.2 Firing temperature and copper diffusion into the lattice

These tests were carried out to study the effect of firing temperature on copper diffusion. The firing temperatures were chosen to investigate the cubic and hexagonal crystal structures of the zinc sulfide lattice which are formed at different temperatures. Four samples were prepared using separate 20 g of source Delta containing 0.6 moles of copper per 100 moles of zinc (0.6% molar ration initial copper content). The samples were fired at 850, 950, 1050 and 1150 °C for 1 hour. The samples were washed in 200 ml solution of 1:1 (v/v) ammonia/water for a period of 24 hours. The samples were designated as AMT850, AMT950, AMT1050 and AMT 1150, respectively.

The results obtained from ICP-MS analyses are presented in Table 5.3 and the ratio of copper to zinc in these samples is shown in Figure 5.4.

Sample	Cu Concentration (mg/l)	Zn Concentration (mg/l)
AMT 850	0.055	230
AMT950	0.064	273
AMT1050	0.035	233
AMT1150	0.039	263

Table 5.3: Cu and Zn concentration of AMT samples based on the ICP-MS results.

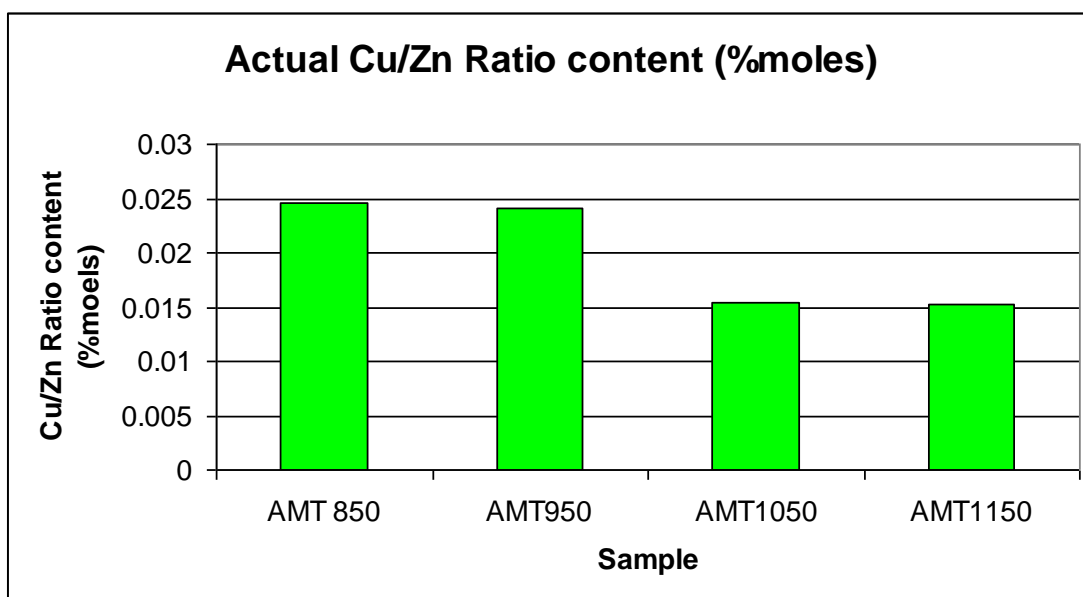


Figure 5.4: The ratio of Cu/Zn in terms of moles of copper per 100 moles of zinc (molar %) based on results from ICP-MS analysis for AMT samples. Hexagonal crystal structures contain less copper impurity compared to the cubic structure.

5.4 Flux content and copper diffusion in single and double fired samples

These experiments were carried out to gain an insight into the effect that the flux has on the diffusion of copper atoms in or out of the zinc sulfide lattice during the firing. Considering that this experiment was carried out with samples prepared via double firing and single firing techniques, it seemed an opportunity to compare both techniques (single

and double firing) against each other in parallel to the study of the effect of the flux content. Hence a series of samples were prepared to provide the appropriate data for analysis and were compared to commercially available Sylvania uncoated ACEL phosphor. These were designated AML & AMF series.

5.4.1 Single firing preparation (AML)

AML samples were prepared using single firing procedure as follows.

Three separate 20 g portions of source Alfa (1.2% initial copper content) were fired together with 5%, 20% and 40% sodium chloride by weight at 850°C for a period of 1 hour. The samples were washed in 200 ml solution of 1:1 (v/v) ammonia / water for a period of 24 hours. They were designated as: AML1 (5% flux), AML2 (20% flux) and AML4 (40% flux).

5.4.2 Double firing preparation (AMF)

AMF samples were prepared using the double firing technique as follows.

A 90 g sample from source Alfa was fired at 850°C for a period of 1 hr. After cooling in air, the sample was ground and divided into four portions of 20 g and each portion was fired with 5%, 20%, 30% and 40% sodium chloride at 850°C for a period of 1 hour. The samples were designated AMF1 (5% flux), AMF2 (20% flux), AMF3 (30% flux) and AMF4 (40% flux).

The ICP-MS analysis results and molar ratio of the Cu/Zn are presented in Table 5.4 and Figure 5.5.

Sample	Cu(mg/ml)	Zn (mg/ml)
AmF1*	0.513	256
AmF2*	0.387	262
AmF3*	0.270	259
AmF4*	0.221	258
AmL1*	0.718	263
AmL2*	0.410	254
AmL4*	0.321	261
SYLV*	0.266	265

Table 5.4: The amount of Cu and Zn found in AmF and AmL samples based on the ICP-MS results.

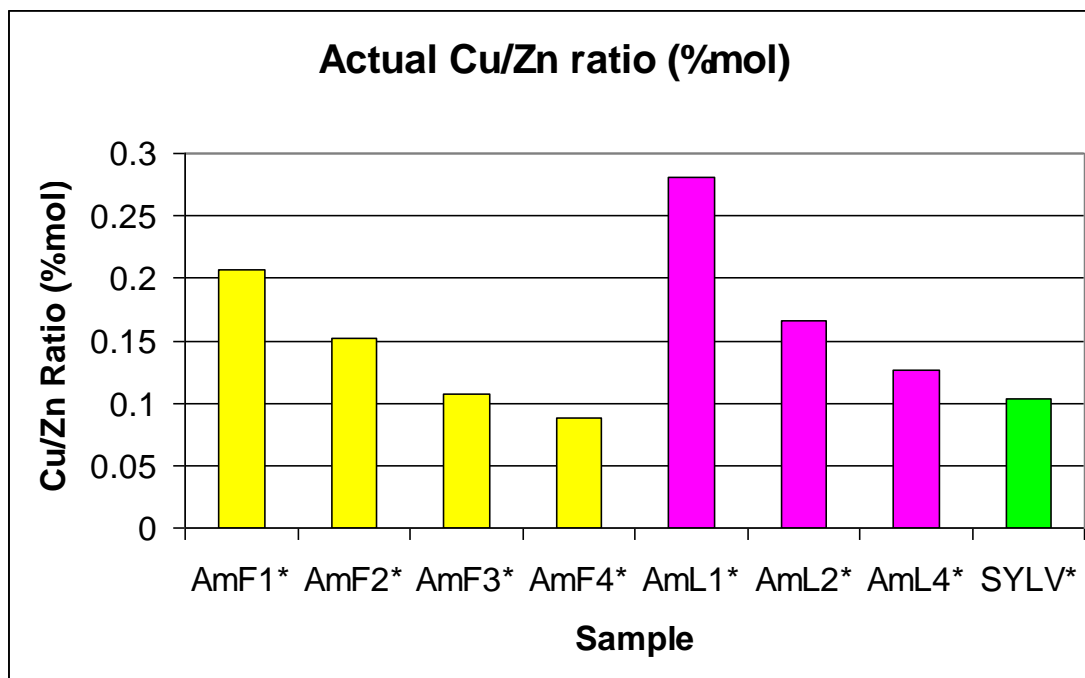


Figure 5.5: The ratio of Cu/Zn in terms of moles of copper per 100 moles of zinc (molar %) based on results from ICP-MS analysis for AmF and AmL samples compared to commercial grade ACEL ZnS:Cu phosphor produced by Sylvania.

5.5 Initial copper content's effect on the final amount of copper present in the lattice

To investigate how the initial amount of copper added to zinc sulfide affects the actual copper content after synthesis a set of three samples (H1, 2 and 3) were prepared each containing different amounts of copper nitrate prior to any firing procedure. After addition of the appropriate copper nitrate (Aq) to these samples, they were then subsequently divided into two sections, one section being exposed to hydrogen sulfide gas based on the theoretical hypothesis that the exposure might have an impact on the state of the copper atoms (by forming copper sulfide) on the amorphous zinc sulfide particles prior to firing which may subsequently have an effect on the diffusion of the copper into the lattice. In this way additional information could be gathered on the complexity of the copper diffusion process considering that it was believed that the highly reactive hydrogen sulfide gas may indeed change the state of the copper and hence its diffusion properties. The samples were prepared as follows.

Three separate 40 g samples of zinc sulfide particles produced by Sylvania (H1,2 and 3) were placed in 20 ml solutions of copper nitrate, containing *H1*: 0.389%, *H2*: 0.194% and *H3*: 0.097% molar ratio of copper to zinc. The samples were then washed with water, filtered and dried.

These samples were each divided into two 20 g portions and one part was exposed to hydrogen sulfide (H₂S) gas for a period of 15 minutes, the samples were designated as H1S, H2S and H3S, respectively while the portions that were not exposed to H₂S gas were named H1, H2 and H3, respectively. The prepared samples were then fired initially

at 850°C for 1 hour, cooled and ground followed by addition of 20% (w/w) sodium chloride flux, they were then re-fired at 850°C for a period of 1 hour. Subsequently, the samples were washed using ammonia.

Sample	[Cu] (mg/l)	[Zn] (mg/l)
H1	0.165	216
H1S	0.192	251
H2	0.138	276
H2S	0.114	234
H3	0.089	266
H3S	0.080	255

Table 5.5: Concentration of Cu and Zn found in AmF and AmL samples based on ICP-MS analysis.

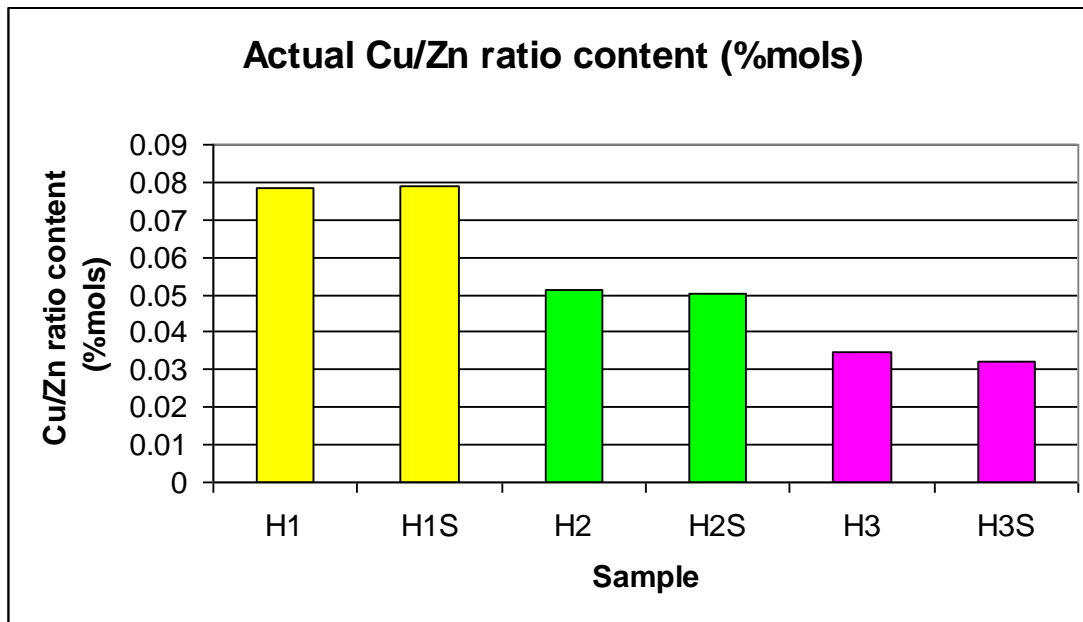


Figure 5.6: The ratio of Cu/Zn in terms of moles of copper per 100 moles of zinc (molar%) based on results from ICP-MS analysis for H series samples. H1 series have the highest copper impurity.

5.6 Copper distribution within the lattice

This test was a novel approach carried out to produce information with regards to the distribution of the doping copper atoms within the zinc sulfide host lattice. The initial steps of the test were designed to find a suitable concentration of *aqua regia* which was to be used as the digesting solution since pure *aqua regia* would digest the phosphor very rapidly. Figure 5.7 shows the mechanism by which this technique is hypothesised to occur.

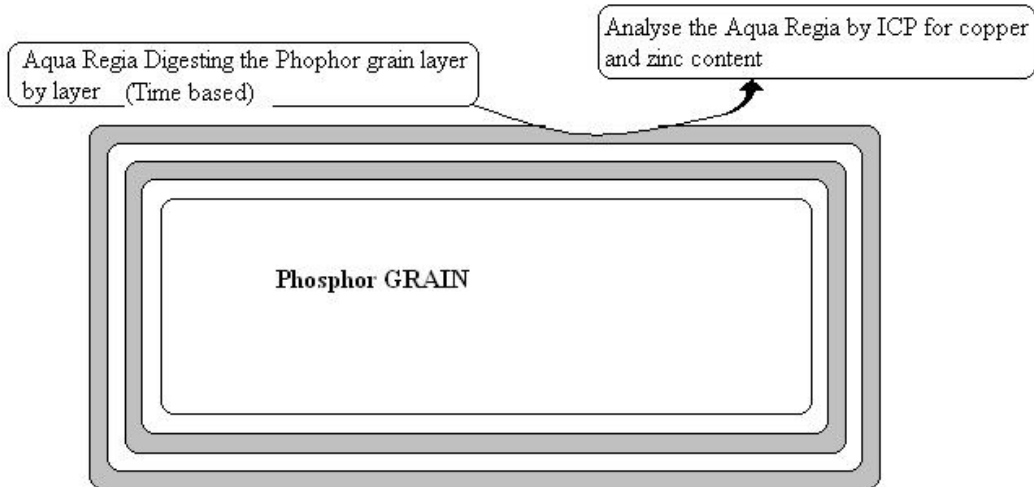


Figure 5.7: Layer by layer digestion of the phosphor particle.

The longer the phosphor is exposed to the digesting solution, the more surface material is digested hence the phosphor is digested layer by layer. Samples are taken from the digesting solution at specific time intervals and examined by ICP-MS for copper and zinc content. Plotting the $\{[Cu (mg/l)] / [Zn (mg/l)]\}$ against time would give a clear indication of whether the copper atoms are distributed evenly all over the host lattice or if they

mainly reside on the surface layers. Figure 5.8 shows the possible outcome of the plot and relevant interpretation of the results.

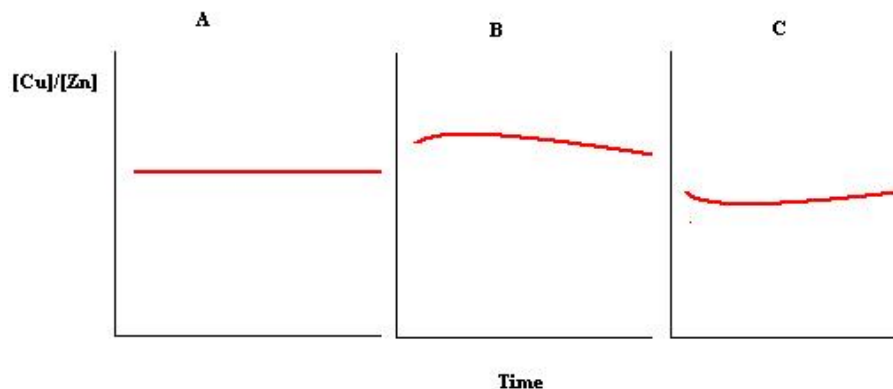


Figure 5.8: Proposed interpretation of the findings from layer by layer digestion of the Sylvania samples. A: even distribution of the copper all over the lattice, B: copper distribution in the outer layers of the lattice, and C: copper distribution in the inner layers of the lattice.

5.6.1 Finding the right concentration of *aqua regia* as the digesting solution and performing the digestion

Hydrochloric acid (20 ml) was added to nitric acid (15 ml) in a pre-acid washed beaker and left to stand for 10 min. This was to be used as the standard ratio of hydrochloric acid to nitric acid for *aqua regia* preparations of this experiment.

From the above recipe, various dilutions (v/v) were prepared to be used for digesting ACEL zinc sulfide particles produced by Sylvania. They were as follows:

1. 10% solution
2. 20% solution
3. 30% solution
4. 40% solution

The experiment was carried out using a total of 30 ml from the above dilutions to digest 1 g of Sylvania ACEL phosphor over a period of time. The phosphor was stirred in the solution via a magnetic stirrer. Before taking 1 ml samples from the solution at consecutive 30s time intervals, the stirrer was switched off for 5 seconds. Figure 5.9 is a schematic of the procedures used.

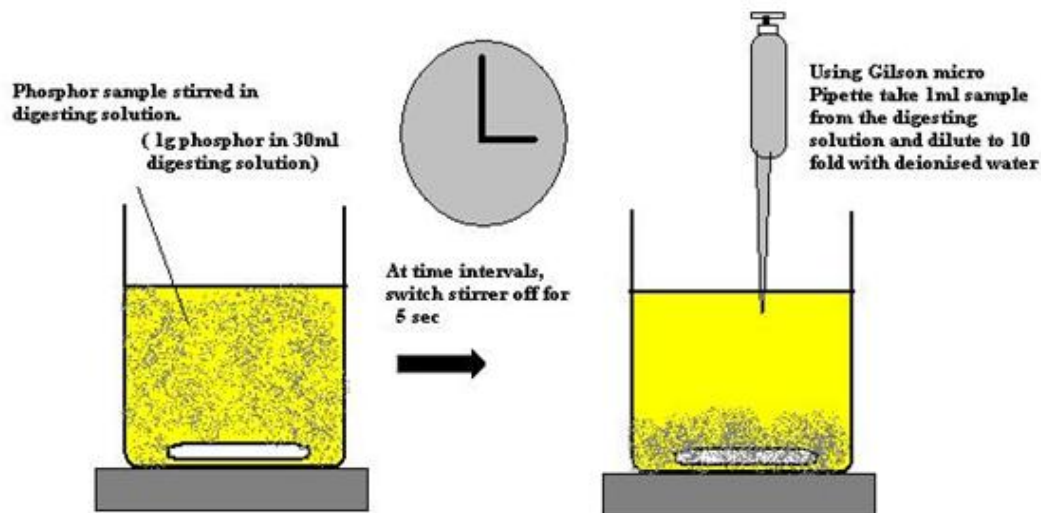


Figure 5.9: The setup of the phosphor and digesting solution.

The samples were then analysed by ICP-MS to quantify the copper and zinc content. The results were then plotted as stated earlier against time. Using the Horiba made particle size analyser the phosphors were tested to observe possible changes in the overall size of the particles.

During the initial tests carried out to find the optimum concentration of the digesting solution, it was observed that the 30% (v/v) diluted *aqua regia* solution produced the most reliable results. Below 30%, the phosphor seemed to be digested at an extremely slow rate and it was not possible to obtain consistent results. However above 30% the digestion process was vigorous as the particles would very quickly get digested away. So only the data using 30% dilution factor were considered and the experiment was repeated to ensure consistency of the results. The data obtained were plotted against time in terms of Cu/Zn ratio and are presented in Figure 5.10. Also at certain time intervals (60, 120 and 180 seconds after addition of the phosphor to the digestion solution), samples were taken for SEM surface analysis (Figures 5.11 and 5.12). These results clearly indicate that the surface of the phosphor is digested away with time.

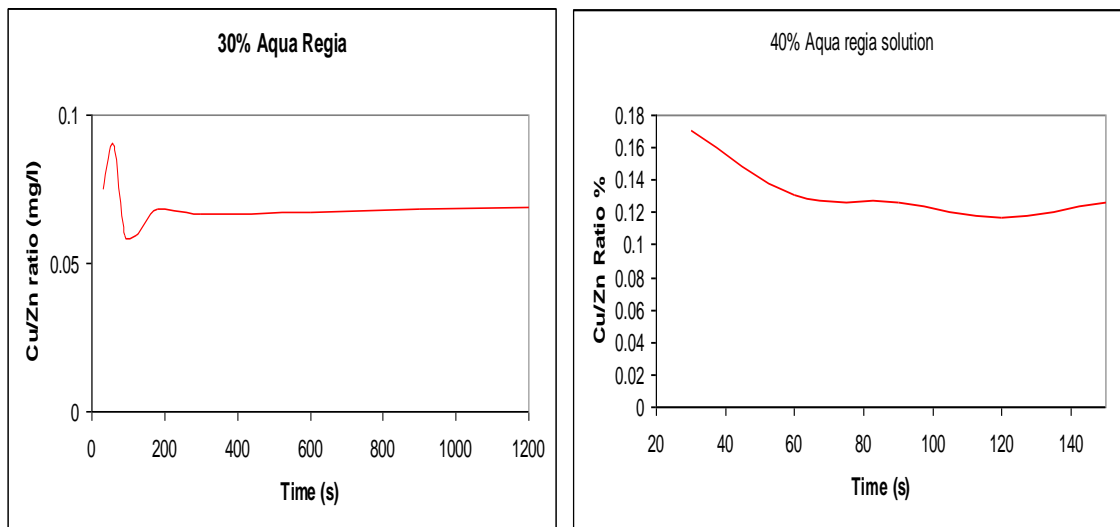


Figure 5.10: Plot of $\{[Cu\ mg/l]/[Zn\ mg/l]\}$ against time (s) for 30% and 40% digesting solution concentrations.

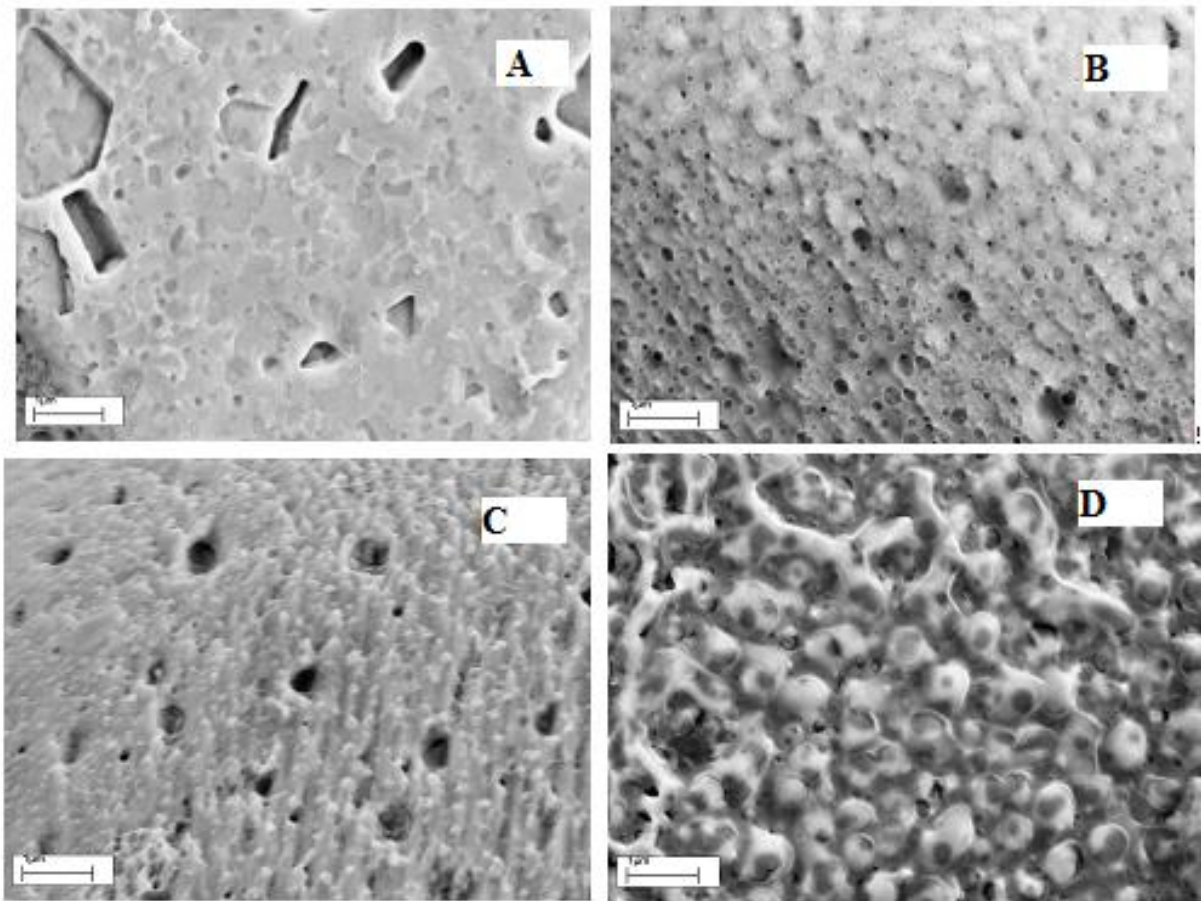


Figure 5.11: *Effect of digestion on the surface of the Sylvania phosphor particles. A: Untreated, B: 60 seconds, C: 120 seconds, D 180 seconds*

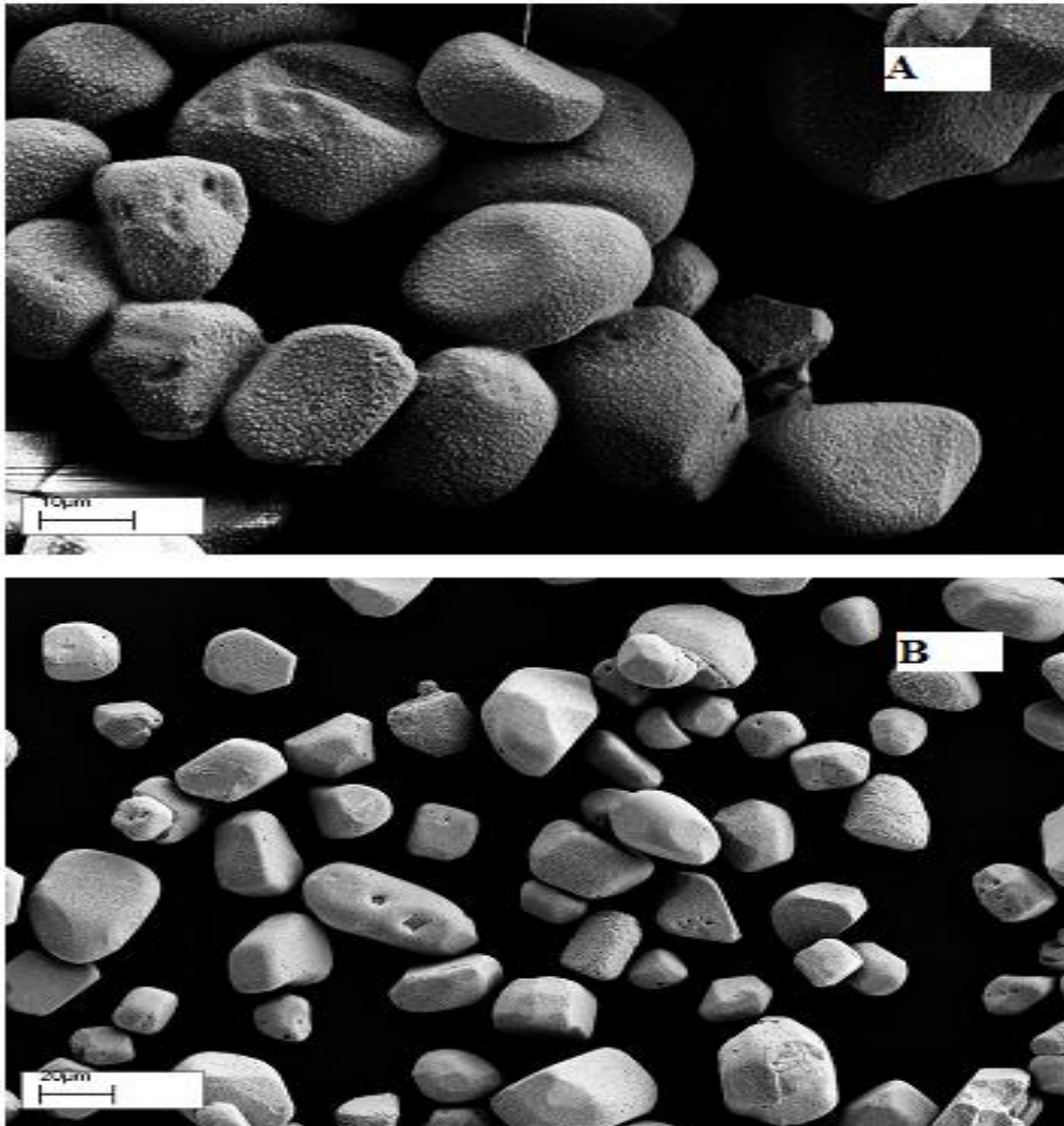


Figure 5.12: Effect of digestion on the surface of Sylvania phosphor particles. A: after 5 minutes treatment B: untreated sample.

Cross section of the particle and copper distribution

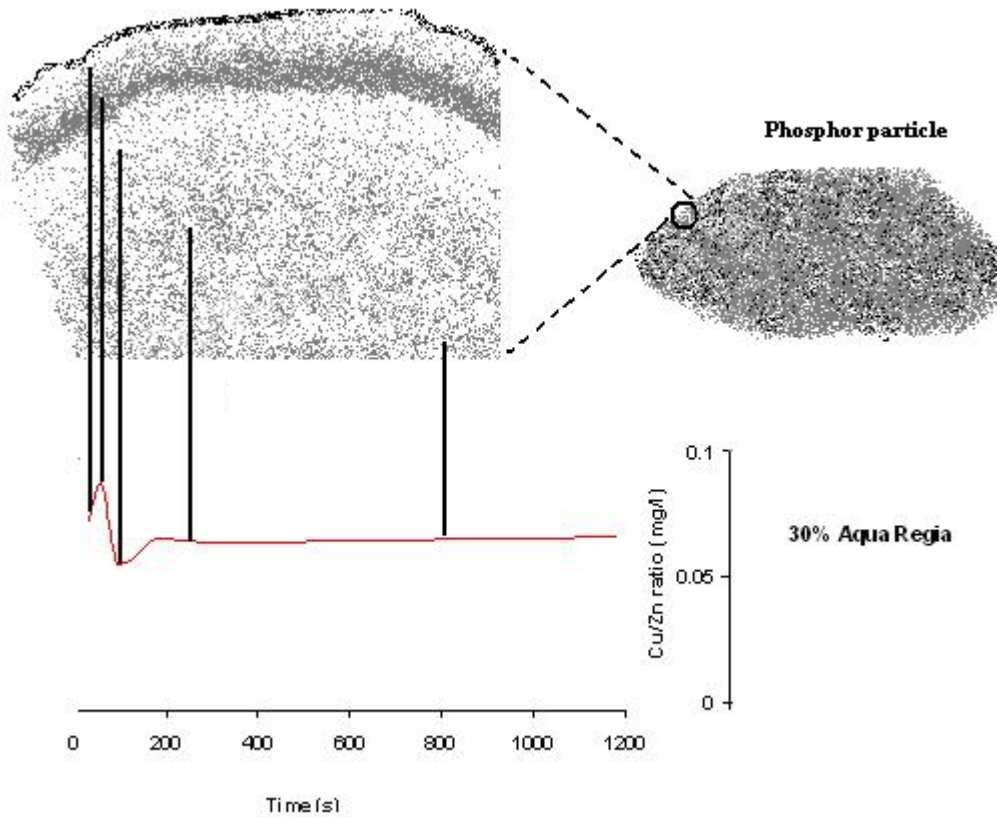


Figure 5.13: Proposed mapping of the copper distribution within the zinc sulfide particles. It seems the surface of the phosphors contain higher ratio of copper to zinc (molar ratio) compared to the inner core layers.

The observations clearly indicate that the doping copper atoms are primarily located within the outer layer of the particles. Based on the finding it can be proposed that a copper rich band is located within the surface of the particle while the rest of the lattice would contain a less, but constant level of copper (Figure 5.13).

5.7 Discussion

As shown in Figure 5.1 the unfired zinc sulfide particles obtained from Sylvania are composed of nano rod shaped particles which agglomerate to form the sphere like particles that were used during the tests. Due to this structure and the cavities present, an extensive surface area is achieved. When the particles are immersed in a copper nitrate solution followed by drying, the copper atoms are distributed evenly throughout the zinc sulfide matrix. However during the firing and the subsequent ammonia washing procedure an excessive amount of copper is removed from the material. Considering that the copper atoms form the luminescent centres, as discussed earlier, it is vital to ensure that the firing procedure during the synthesis is optimised to ensure sufficient copper remains to produce efficient phosphor material.

Analysis of samples Am1 and 2 indicate that the more prolonged the initial firing procedure, the more copper atoms are eliminated from the final material. This is again confirmed from D20-80 samples where lower initial copper content was used and it appears that after 40 minute firing more copper seems to leave the lattice.

At the same time the firing temperature, aside from effecting the crystal structure of the material (cubic or hexagonal), seems to be directly involved in the amount of copper that remains within the lattice; results obtained from AMT 850-1150 samples indicate this. In chapter 8 the findings of these experiments will be discussed further.

5.8 Key observations

- The actual amount of copper remaining within the zinc sulfide lattice is ~ 10% lower than the copper added to the material prior to firing.
- Presence of the flux at the first stage of firing the material will enhance the loss of copper from the material.
- Commercial samples contain 1% molar ratio of copper to zinc ratio which is less compared to some other samples prepared e.g. Amf1 & AmL1, yet they demonstrate better emission properties (chapter 4) indicating that copper content alone cannot be a determining factor of emission property.
- During the firing procedure the doping copper tends to leave the zinc sulfide host and hence particles demonstrate higher copper content at the surface layers compared to inner layers of the particles.

Chapter 6 : Effect of electric field and frequency on the emission properties of the ACEL panels

6.1 Introduction

The electric field across the electrodes is the driving force behind the process of electroluminescence and hence understanding the interaction of the field with the phosphor and dielectric particles would provide valuable knowledge which may lead to the fundamental understanding of the process at the atomic level. In some early attempts by Lvova⁷⁴ to investigate the Destriau effect in respect of its associated kinetics, he considered the kinetics of electroluminescence from a single standpoint. The process was described by considering a system of transport equations for a crystal phosphor with three systems of levels in forbidden band: levels of luminescent centres, shallow electron traps and deep donors. In principle, their approach tried to explain the nature of the field distribution in a given crystal in a mathematical model. A basic physical description of a system of levels and their associated centres when charged through absorption of energy from an external field is fundamental to their approach of understanding the process. This is all assuming that the luminescent centre is neutral before excitation and it is ionised by excitation, surrendering an electron to the conduction band and becoming positively charged. A considerable simplification of the general system of transport equations is achieved by making a general and experimentally justified assumption about the Destriau effect; the electroluminescence process occurs in two stages where a high field region is established in a phosphor crystal grain and during its excitation, charges (holes and electrons) drift in an electric field in the interior of the crystal.

This part of the research involved analysing and studying multiple properties and characteristics of ACEL panels such as the size of the gap between the two electrodes, the frequency and the voltage across the panel in a practical manner rather than using assumptions or extensive theoretical evaluation.

6.1 Driving voltage and luminance

Using the optimum combination of phosphor to oil ratio (chapter 3) an ACEL panel was made and the relationship between voltage and luminance using Sylvania uncoated ACEL ZnS:Cu phosphor was investigated. The panels were prepared as described in and the results are presented in Figure 6.1.

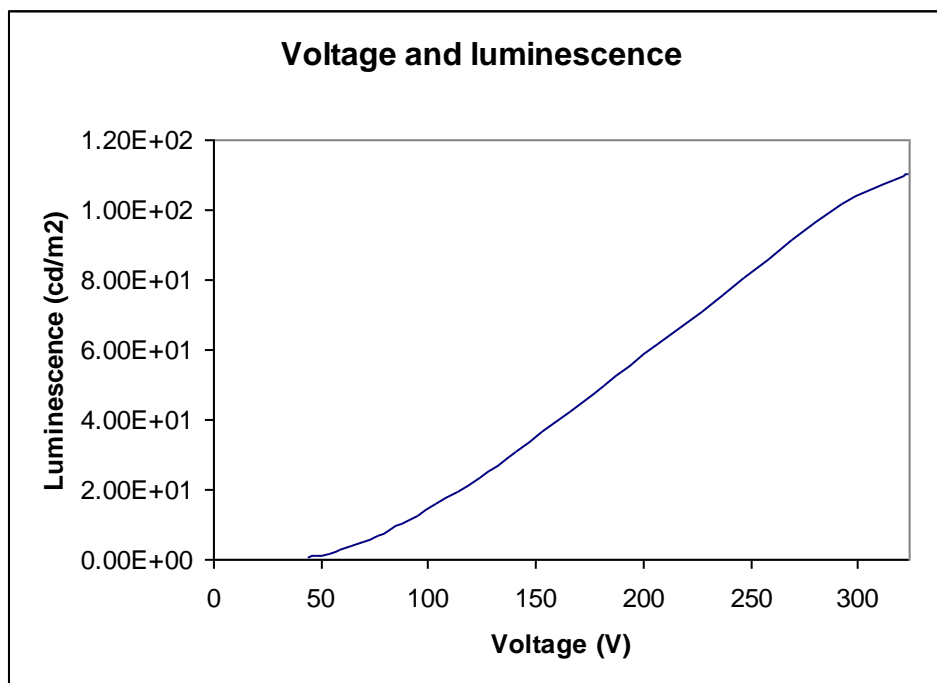


Figure 6.1: Plotting luminance of the panel against the driving voltage at 400Hz frequency

The following models (6.1-3) were proposed for the relationship between voltage & luminance and TSP^{xiv} software was used for statistically analysing the models.

$$lum = a.volt + d \quad (6.1)$$

$$lum = a.volt \quad (6.2)$$

$$lum = a.volt^\alpha \quad (6.3)$$

The statistical analysis results of the above models are presented in the appendix A1.

6.2 Electroluminescence decay at 181 volts

ACEL panels loose efficiency over time, hence it would be ideal to investigate the emission decay over a period of time. The Sylvania sample was tested for the effect of time on luminescence decay at 181Volts and 400 Hz. Figure 6.2 shows the degradation of the phosphor emission over time.

^{xiv} TSPTM is statistical analysis software for the estimation and simulation of econometric models. It is a world-wide standard for econometric estimation. TSP stands for "Time Series Processor". TSP was originally developed primarily by economists however there is nothing in its design limiting it to economic time series. Any data consisting of repeated observations of the same variable for different units may be analyzed with TSP.

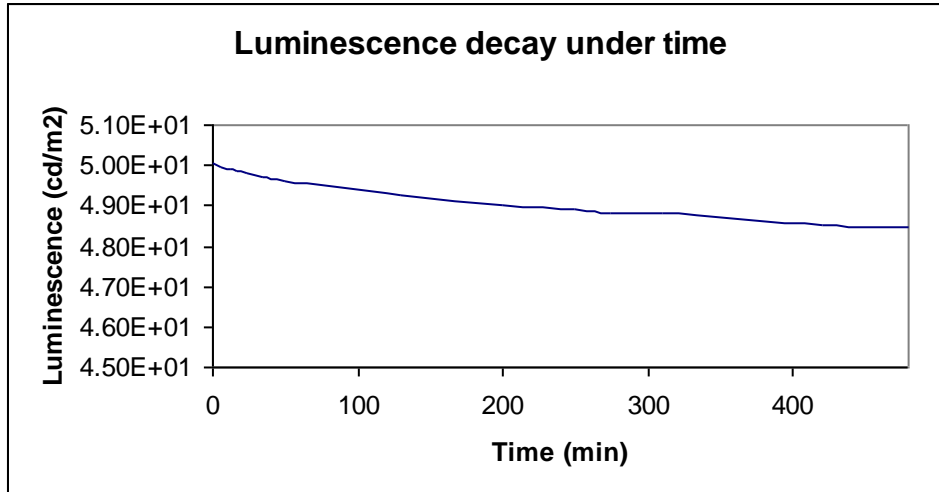


Figure 6.2: Luminance decay over a period of 500min, 181V and 400Hz.

The following mathematical models were investigated in respect of the data presented in Figure 6.2:

$$lum = a.time + d \quad (6.4)$$

$$lum = a.time^d \quad (6.5)$$

$$lum = e^{a.time+d} \quad (6.6)$$

The statistical analysis results of the above models are presented in the appendix A2.

6.3 Creating a direct relationship between emission intensity, voltage and frequency

To achieve an accurate relationship which would define the relationship of driving voltage and frequency in one whole equation, a series of tests were carried out were a panel made using uncoated Sylvania phosphor, as described. Then emission intensity of the phosphor under driving voltage of 70 to 226 volts & frequency of 100Hz to 400Hz was measured These data were then assessed using TSP software to estimate the most

accurate relationship that could be achieved to define a relationship between the three factors of luminescence, voltage and frequency. The proposed model, equation 6.7, and its statistical analysis results are presented below and the statistical analysis of the model is presented in appendix A3.

$$lum = f(freq.volt.etc...)$$

$$lum = A.(freq)^\alpha .(volt)^\beta$$

$$\ln lum = \ln A + (\alpha.\ln freq) + (\beta.\ln volt) \quad (6.7)$$

6.4 Luminescence decay under high driving frequency

It is well observed that under high drive frequency, the dominant wavelength emission of the phosphor tends to shift toward the shorter wavelengths of the spectrum while the phosphor demonstrates swifter electroluminescence decay. Using sample preparation techniques described earlier, ranges of driving frequencies were examined at 206 volts driving voltage. The panels were tested at 1, 10, 20 and 30 kHz. Figure 6.3 shows the effect of various frequencies on the decay of luminescence efficiency over time.

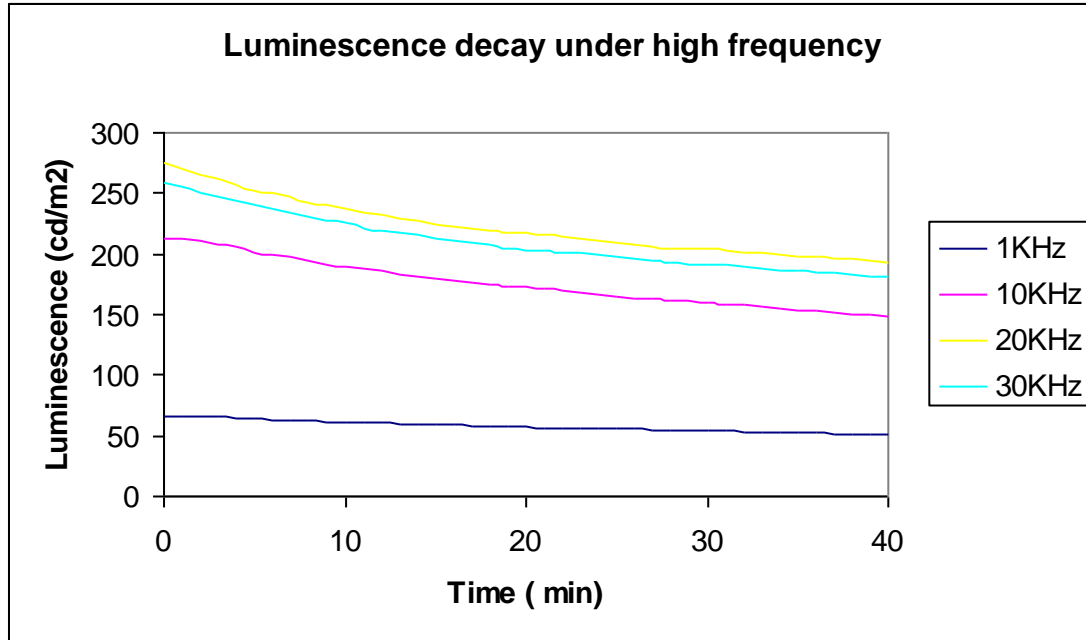


Figure 6.3: Effect of various frequencies on the luminescence over time.

These data were examined using different mathematical models to investigate the relationship between electroluminescence decay and frequency of the alternate current and the models were assessed using TSP software for statistical accuracy.

The general form of the model is $y = e^{f(t)}$ where y is the luminance, t is time and $f(t)$ can be demonstrated in different forms, among them we try the three following forms: $f(t) = B*t$, $f(t) = B*t + C$, $f(t) = A*t^2 + B*t + C$ & the linear form of the above general model by applying log function is: $\ln Y = f(t)$. Three regression models were used:

$$\ln Y = B*t \quad (6.8a)$$

$$\ln Y = B*t + C \quad (6.8b)$$

$$\ln Y = A*t^2 + B*t + C \quad (6.8c)$$

Using Ordinary Least Square (OLS) regression method to estimate the parameters A, B, and C for each of the data series gives the following tabulated results for each model as presented in appendix A4.

From this set of analysis equation 6.8c seems to be the most accurate estimate. Table 6.1 shows the estimated values of each variable in equation (7.8c) according to the frequency of the AC current.

Freq	A	B	C
1Khz	4.194795	-0.00835	0.000047
10Khz	5.369996	-0.01311	0.000103
20Khz	5.60626	-0.01483	0.000166
30Khz	5.550541	-0.01445	0.000147

Table 6.1: Estimated values of each variable in relation to the frequency of the AC current based on the model three.

6.5 Interference in the electric field

The electric field is affected when dielectric materials are placed in the direction of the field. Assuming the effect upon the field would supposedly have an effect on the electroluminescence process of the phosphor particles, a series of tests were designed and carried out to observe whether this effect would be significant or negligible on the electroluminescent emission of ACEL panles.

Using commercially available uncoated ACEL phosphor from Sylvania some samples were prepared by mixing the commercial phosphor with barium titanate and strontium titanate as shown in Table 6.2.

Sample	% Dielectric (by weight)	Preparation (Commercial Sylvania Phosphor + dielectric material)
S6	37.5%	0.1g Sylvania + 0.06g strontium titanate
S4	25.0%	0.12g Sylvania + 0.04g strontium titanate
S2	12.5%	0.14g Sylvania + 0.02g strontium titanate
B6	37.5%	0.1g Sylvania + 0.06g barium titanate
B4	25.0%	0.12g Sylvania + 0.04g barium titanate
B2	12.5%	0.14g Sylvania + 0.02g barium titanate

Table 6.2: Preparation of sample with added dielectric material quantities.

These samples were then mixed with 0.8 g (1/3 total weight) linseed oil to be used for preparation of ACEL panel for electroluminescent intensity measurement. The samples were then tested under various voltages across the plates, 123 to 207 volts. The electroluminescence intensity and dominant wavelengths of emission were measured.

Through the technique described earlier, using TSP software and the data gathered various models were tested for accuracy to define the relationship between luminescence and driving voltage.

Of the many models tested the most accurate estimate were equation (6.2) & (6.3), however equation (6.2) seems most accurate where $lum = a.Volt$. The determination coefficient value of each of the two proposed formulas for each sample and the calculated parameter (a) are presented in appendix A5 & figure 6.4.

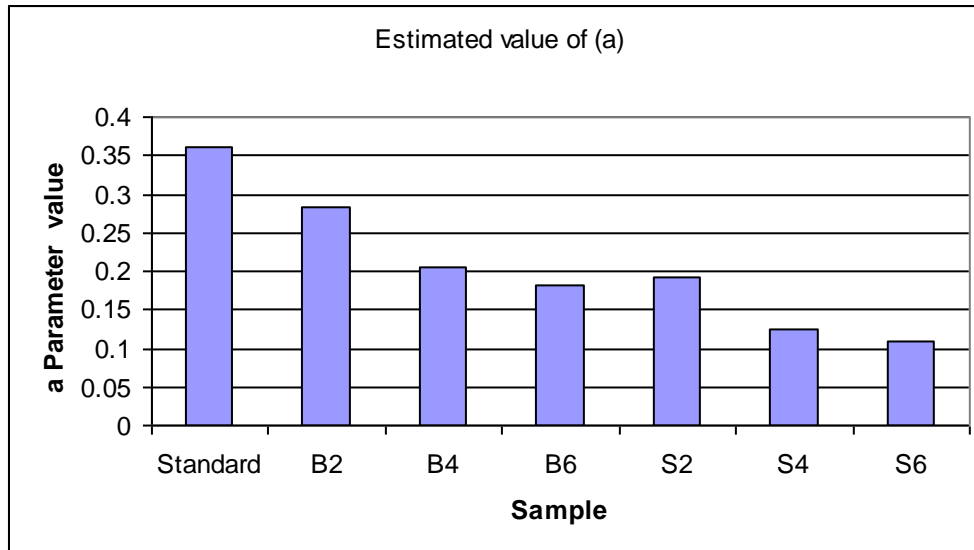


Figure 6.4: Graphical presentation of the parameter a based on the dielectric used and the quantity of it. Both dielectrics reduce the parameter ' a ' however, strontium titanate seems to be reducing the compared to barium titanate.

6.6 Luminescence studies of D1 sample under various voltages and frequencies

Considering that one of the most successful samples prepared using an in house technique was the D1 sample, this sample was chosen for further investigations. Panels were prepared using D1 phosphor. However, considering that particles in this sample were much smaller than the commercially available Sylvania phosphors, they were used for analysis of the effects of spacing between the two electrodes. The panel preparation in this case involved using standard 12 micron and 24 micron spacer sheets between the electrodes; panels were prepared with either of the two spacers present between the two electrodes. Using TSP software and statistical modelling the results gained from the D1 sample, prepared using the 12 micron spacer, were tested to generate a possible formula relating voltage and frequency together and estimate the possible constants that would be present in the formula.

6.6.1 Voltage and frequency studies of D1 samples

The panel was prepared as stated earlier. Using driving frequency values of between 50 to 20 kHz and driving voltage in the range of from as little as 28 to ~200 volts, an extended series of data of electroluminescence intensity were gathered (above ten thousand readings) with respect of driving voltage and frequency.

For example; using a static 10 kHz frequency, the panel was tested for electroluminescence intensity in a range of driving voltage values from 28 to 199 volts. This generated a set of electroluminescence intensity values which could be plotted against the appropriate voltage. These were then classed as the 10 KHz series. This test was carried out over a whole range of frequency values, as stated earlier.

Using the TSP software, these data were then used to create a relationship between electroluminescence intensity and driving voltage for each frequency series. Two of the most accurate proposed mathematical equation models for the D1 sample tested at 150Hz frequency with 12 micron spacer along with accuracy estimation of the relevant formula, are presented in appendix A6.

Equation 6.3 was chosen since the majority of the frequency series showed much more accuracy for this model. Appendix A6 shows the calculated determination coefficient values for 12 micron spacer samples using the model using different frequencies. The data gathered using the 23 micron spacer was treated exactly in the same manner to produce the results of analysis. The analysis showed, that as expected, these set of data also followed the same pattern as for equation 6.3.

The calculated parameters of each frequency series tested are presented in Table 7.13a and b. In order to measure the parameters in the equation, taking the natural logarithm of both sides of the equation, the formula had to be treated as follows:

$$lum = a.Volt^\alpha \text{ Is rewritten as } \ln lum = \ln a + \alpha.\ln Volt$$

The parameters measured were $\ln a$ and α . The calculated values at each frequency are presented in Table 7.13a-b for each of the two 12 and 23 micron spacer tests.

6.6.2 Creating a relationship between the voltage and frequency

The data gained in previous sections were used to find the relationship between the frequency and the two calculated parameters ($\ln a$ and α). The following mathematical models (equation 6.9-12) were proposed and statistically tested to find the most accurate fitting of the formula to the data obtained.

The proposed models for the relationship between α and frequency and their statistical accuracy testing for the 12 micron spacer tests are presented in Table A7. Based on this observation equation (6.11) was chosen as the most accurate model from the sets.

$$\alpha = \rho.freq + m \quad (6.9)$$

$$\alpha = \rho.freq^\beta \quad (6.10)$$

$$\alpha = freq^\beta \quad (6.11)$$

$$\alpha = \rho.freq^\beta \quad (6.12)$$

The proposed models (equation 6.13 & 6.14) for the relationship between $\ln a$ and frequency and their statistical accuracy was tested.

$$\ln a = \lambda \cdot freq \quad (7.13)$$

$$\ln a = \lambda \cdot \ln freq \text{ or } a = freq^\lambda \quad (7.14)$$

Equation 6.14 was chosen as the most accurate model. To drive an overall formula relating voltage and frequency and decay of luminance over time considering the following relationships which have been demonstrated to be most accurate we can make the following conclusion:

$$lum = a \cdot volt^\alpha$$

$$a = freq^\lambda$$

$$\alpha = freq^\beta$$

$$lum = freq^\lambda \cdot volt^{freq^\beta} \quad (6.15)$$

Using the general data obtained from various panels made with D1 phosphor, the above model was tested for accuracy in practice and it failed to show results close to the practical values obtained. The model was also developed for the 23 micron spacer data sets and again it was not producing any results close to the practical data gained.

6.7 Crystal structure and luminescence efficiency

Using the phosphors AMT850 and AMT1050 (Chapter 3) panels were prepared as described earlier to investigate how the crystal structure of the ACEL phosphor may have an effect on the luminescence efficiency of the phosphor in relation to the driving voltage while investigating the luminescence decay rate for each sample.

6.7.1 Voltage and frequency effect

Using driving frequencies of 400, 1000 and 10 kHz the samples were tested under a range of driving voltage from 113 up to 263 volts. The data obtained were analysed using TSP software and proposed models defining the relationship between driving voltage and luminescence efficiency were statistically tested for both AMT850 and AMT 1050. These findings are presented in Figures 6.5 & 6.6 and the statistical analysis of the fits is presented in appendix A8 & A9.

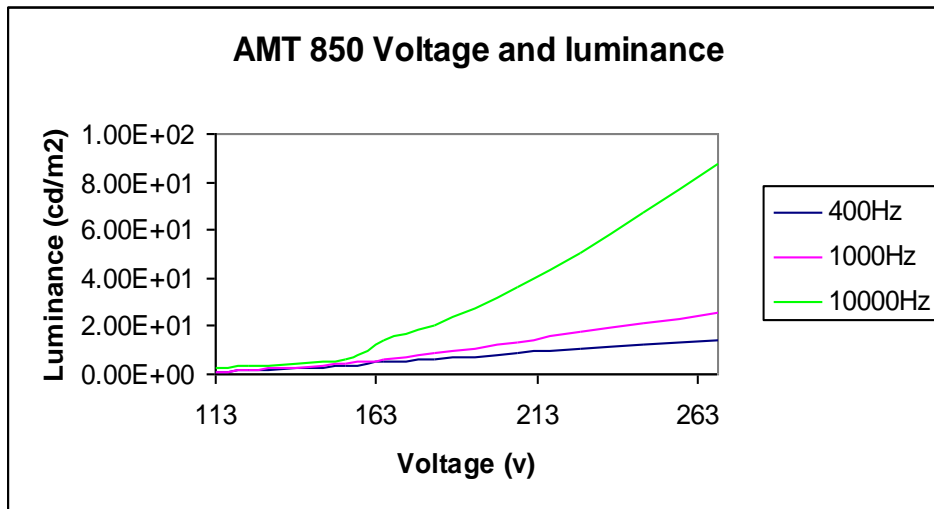


Figure 6.5: Relationship between driving voltage and luminance at various frequencies using AMT850 zinc sulfide phosphors which are fired at 850°C with a cubic crystal structure.

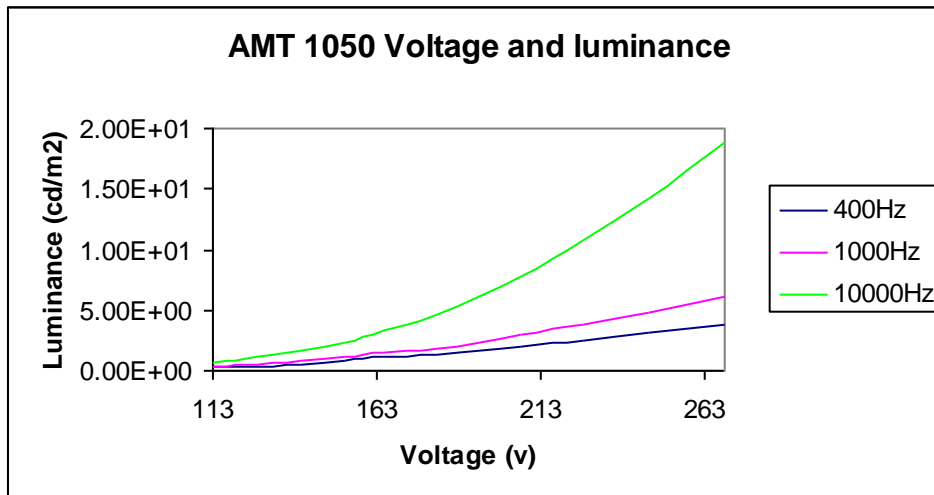


Figure 6.6: Relationship between driving voltage and luminance at various frequencies using AMT1050 ZnS phosphors which are fired at 1050°C with a hexagonal crystal structure.

Based on these results Table 6.3 a-b demonstrates the calculated values of a and α , considering $lum = a.volt^\alpha$ being the most accurate model.

AMT850 (a)

Freq (Hz)	a	α
400	5.852E-6	2.64588
1000	8.8878E-8	3.51652
10000	3.21641E-9	4.32682

AMT1050 (b)

Freq (Hz)	a	α
400	1.3897E-7	3.08106
1000	6.07196E-8	3.31015
10000	6.46282E-9	3.91549

Table 6.3: Estimation of the parameters (a & α) considering the equation 7.3 for AMT850 and AMT1050 samples.

6.7.2 Electroluminescence intensity decay at high frequencies

Identical panels were prepared as described using AMT850 and AMT 1050 samples. Using driving frequency of 15 and 20 kHz, at 206volts Luminescence decay over time for AMT 850 and AMT 1050 samples were measured. The data were tested accordingly by the TSP software to find the most accurate relationship defining the decay rate. The proposed model (equation 6.16) for these data and its statistical analysis are presented in appendix A10.

$$\ln lum = at^2 + bt + c \quad (6.16)$$

Based on this analysis the hexagonal crystals parameters a and b demonstrate different values compared to the cubic structure.

6.8 Discussion

In defining a relationship between the luminance of a panel and the applied voltage, when using commercial Sylvania samples, the most accurate model was equation 6.2. Hence the constant 'a' can be regarded as a factor relating directly to the property of the phosphor material. However when sample D1 was investigated equation 6.2 seemed to be inaccurate and instead equation 6.3 was a more accurate form of defining the relationship. This can only be explained through the difference in the particle size of the two phosphors. The commercial sample had an average particle size of ~20 microns while the D1's average size range was ~5 microns, thereby suggesting that perhaps the particle size itself was a major factor when considering the luminance of these particles against the voltage applied. The electric field is the driving force behind AC-electroluminescence and hence it can be argued that the interaction of the electric field with the particles is different when different particle sizes are considered. At the same time the particle size distribution in these materials can never be homogenous hence causing an error factor when defining a mathematical relationship for their EL properties.

6.9 Key observations

- The relationship between luminance and the driving voltage can be varied depending on other factors such as particle size or dielectric materials in the panel.
- No overall mathematical relationship can be considered for ACEL zinc sulfide phosphor panels since multiple factors such as the electric field, driving voltage, degradation of the phosphor at high frequencies and even the nature and quantity of dielectric present impose significant effects on the emission process.
- Hexagonal and cubic structures do follow a similar mathematical pattern when voltage and luminance are investigated however; the parameters that effect the relationship are varied between the two crystal structures.

Chapter 7 Discussion

7.1 Thermal quenching analysis

The results obtained from thermal quenching analysis clearly indicate that the quenching of the material alters its photo-luminescent and electroluminescent properties. However the XRD analysis of the sample does not indicate any observable change in terms of the crystal structure of the material. This would suggest that the quenching is only affecting the luminescent centres within the lattice. It is also clear that the importance of the temperature at which the sample is quenched is significant within the range of about 200-300°C. The results also clearly demonstrate that the emission intensity of the samples is decreased as a result of the thermal quenching procedure, which again indicates that the luminescent centres are directly affected by the thermal quenching process.

However, it can also be argued that certain luminescent centres, particularly those emitting at lower wavelengths are deteriorated by thermal quenching while those emitting at longer wavelength are not. This would lead to the changes observed in the dominant wavelength and lower emission intensity observed from this study.

All previous studies have been carried out with emphasis on photo-luminescent properties of the green and blue Cu centres. These centres are formed by the activator (Cu) and the co-activator (Cl) when introduced at nearly equal concentrations. The luminescent transition takes place from the co-activator to the activator pairs which have different intra-pair distances. The activator level in green centres is much deeper than

those levels involved in the edge emission. Before being excited, Cu is mono-valent while after excitation it becomes divalent. The induced absorption band due to Cu^{+2} band has been shown to be the cause of the green emission⁷⁵.

A model for the blue Cu luminescent centre has been proposed which states that the centre is formed by association of substitutional Cu^+ and an interstitial Cu^+ ⁷⁶. The green Cu centre shows no spectral shift, indicating that it is due to an intra-centre transition. To date, the initial state of the transition, however, remains unclear.

It seems from this study that the blue centres are vulnerable to the thermal quenching procedure carried out due to the role that the interstitial Cu^+ species play in this mechanism. The interstitial Cu^+ is not as stable in its location within the lattice compared to a substitutional Cu^+ and hence a thermal shock is prone to affect its location or association with its surrounding element. The green emission centre, however, seems unaffected.

Repeated thermal quenching of the same sample does not affect a further shift in the dominant wavelength, however it does effect the brightness efficiency of the material, indicating that the damage caused to the interstitial Cu^+ positions occurs mostly in the first treatment and further thermal quenching only effects the brightness of the material which is due to multiple heating treatment of the sample only. It can be concluded that the repeated firing of the material tends to destroy the majority of the emission sites hence reducing the amount of the overall lighting output from the emission.

7.2 Copper diffusion into the lattice

As shown in Figure 5.1 the unfired zinc sulfide particles obtained from Sylvania are composed of nanorod shaped particles which agglomerate to form the sphere like particles that were used during the research. Due to this structure and the cavities present, an extensive surface area is achieved. When the particles are immersed in a copper nitrate solution followed by drying, the copper atoms are distributed evenly throughout the zinc sulfide matrix. However during the firing and the subsequent ammonia washing procedure an excessive amount of copper is removed from the material. Considering that the copper atoms form the luminescent centres, as discussed earlier, it is vital to ensure that the firing procedure during the synthesis is optimised to ensure sufficient copper remains to produce efficient phosphor material.

Analysis of samples Am1 and 2 indicate that the more prolonged the initial firing procedure, the more copper atoms are eliminated from the final material. This is again confirmed from D20-80 samples where lower initial copper content was used and it appears that after 40 minute firing more copper seems to leave the lattice.

At the same time the firing temperature, aside from affecting the crystal structure of the material (cubic or hexagonal), seems to be directly involved in the amount of copper that remains within the lattice; results obtained from AMT 850-1150 samples indicate this. However, considering the fact that these particular samples were prepared using a single firing step which is conventionally used during the ZnS:Cu synthesis we can assume that the actual copper to zinc ratio in the double stage firing technique is lower than samples

prepared via single firing procedure. AmF and AmL sample series were prepared to observe the difference in final copper content depending on the firing technique applied and the findings were compared against commercial grade Sylvania phosphor which is of prime quality in terms of luminescence efficiency.

The results presented in Figure 5.5 indicate that AmL samples, which were prepared via a single firing technique, contain higher copper levels compared to AmF double firing prepared samples. However when compared to commercial grade Sylvania ACEL phosphor, using 30- 40% sodium chloride flux achieves a final copper content near the levels found in commercial materials. All the data obtained from each set of experiments indicates that, irrespective of the amount of copper initially added to the sample, after firing a considerable amount of the copper leaves the lattice and is washed off in the subsequent steps. The H1S and H1, together with the other H replicate samples, clearly indicate that even exposing the material to the reactive H_2S gas does not make any difference in terms of the final copper content. More specifically, the zinc sulfide crystal structure can accommodate only a certain number of copper atoms within it.

The most interesting observation in this study was the novel attempt to create a map of copper distribution within the zinc sulfide lattice. As demonstrated in Figure 5.10 the results obtained from using a 30% *aqua regia* solution were ideal for this analysis, while the 40% solution was too concentrated and hence the phosphor was digested too quickly to create a map of the copper distribution. Figure 5.11 shows the effect of the digestion on the surface of the particles clearly indicating that the surface is slowly etched away.

Overall, from the data in Figure 5.13 it can be concluded that during the firing of the materials, most of copper atoms interact and bind with each other and diffuse out of the zinc sulfide lattice while the zinc sulfide crystallises. However during this process, smaller quantities of copper atoms are left in the lattice and, as explained earlier in Chapter 5, form interstitial or substitutional copper sites within the lattice. The surface of the particles contains most of the copper content while the rest of the copper is equally distributed within the lattice. This outer layer copper localisation may play a key role in the process of ACEL; which would require further tests to be carried out to prove this hypothesis. As argued earlier, the thermal shocking of the samples caused a shift in the dominant wavelength of the material and it can be hypothesized that the outer layer copper atoms are more sensitive to the sudden thermal shocking compared to the ones localised within the inner layers.

7.3 Efficient zinc sulfide phosphor particles

The effect of firing conditions and procedures on the quality of phosphor materials produced is a rather complex issue to discuss. This is mainly because no specific mechanism for AC electroluminescent emission has ever been proposed. As discussed earlier there are many hypotheses as to how this phenomena occurs but the uncertainty makes it difficult to explain why particular synthetic routes yield materials different in terms of emission quality, considering that the materials are constituted of zinc, sulfur and copper with cubic or hexagonal crystal structure. Hence further elaboration on this topic would require a detailed examination of the orientation of the lattice within each

crystal structure. One of the most recent studies on the crystal structure of the ACEL zinc sulfide particle was carried out by the Wolfson Centre for Material Processing at Brunel University⁷⁷ where in an innovative approach using hydrochloric acid, phosphor particles were etched to reveal their internal structure visually and the way their internal lattices were oriented was studied. In these studies it was demonstrated that the smooth surface of the particles that is observed before any treatment, is etched away by the acid to reveal the internal structure of the crystal. This internal structure exhibits pyramids at one end of the particle while the particles taper to a flat side at the end. Clearly defined layers sandwiched between the two ends of the particle are observed. Commercial Sylvania zinc sulfide materials demonstrate the foregoing features as shown in Figure 7.1.

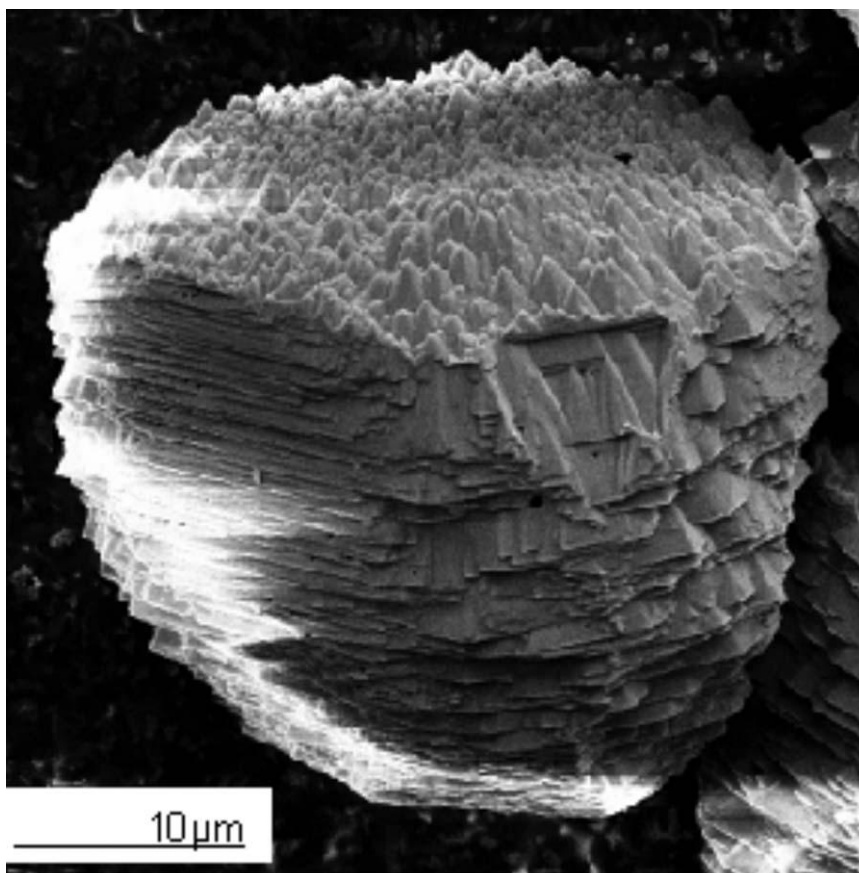


Figure 7.1: FESEM image of a single Osram Sylvania _type 728_-uncoated ACEL ZnS:Cu-based particle after etching with hydrochloric acid for 15 min, showing the layered structure along the [111] direction and pyramids at one end (courtesy of Wolfson Centre, Brunel university).

The cubic zinc sulfide is twined along the [111] axis. This twining is reported for both synthetic ACEL zinc sulfide⁷⁸ and also on natural Thomsaton Dam sphalerite mineral⁷⁹.

Through personal discussions with these researchers it was declared that via their most recent research of the ACEL phenomenon, they have demonstrated that the particles emit photons along the planes, visible under microscope, provided that the crystal layers are in line with the electric field. Otherwise as the orientation of these layers occurs against the direction of the field, the intensity of luminance is decreased and at 90° there will be absolutely no emission. During the firing steps taken in synthesising these materials from

the one micron precursor zinc sulfide particles, it is possible to end up producing larger particles resulting from the fusion of the precursors. As a result, particles will be formed which may have some constituent having their planes formed at different angles to the planes of other constituents within the particle. This is simply referred to as particles having fault in their crystal structure. So far it can be argued that aside from the luminescent centres, the direction of the crystal planes play a vital role in the phenomenon of ACEL.

7.4 X-ray analysis of the phosphor particles

A comparison between the quenched and un-quenched phosphors using XRPD ($\lambda=0.828692\text{\AA}$) and x-ray absorption spectroscopy (XAS) has been undertaken. The XRPD results (Figure 4.11 a) shows that the expected highly faulted structure is observed with excellent resolution out to 150° {or to the (12 2 2)} of the Sphalerite phase. The quenched sample compared to the reference sample shows a large change in peak ratios between 46.7° and 46.9° , thought to correspond to the Wurtzite (0 0 6), (0 3 2) and Sphalerite (3 3 3)/(5 1 1) peaks. Hence a large proportion of this diffraction is lost from the material upon rapid quenching but not when the material is allowed to cool slowly (the heated sample showed reversible thermal expansion). Figure 4.11 shows the separation of the sphalerite (1 1 1) and wurtzite (0 0 2) diffraction lines with very broad diffraction intensity shown whereby diffraction intensity is observed between the three peaks. In Figure 4.11b the region between 46.7° and 46.9° is shown which corresponds to the wurtzite and sphalerite lines indicated. On quenching the sphalerite intensity is dramatically reduced.

The Zn K edge XAS data (Figure 4.12) does not allow for an easy understanding of the subtle crystallographic differences between quenched and unheated specimens. However it gives an indication that the electronic structure has altered due to changes in Zn K-edge shape. It is noted that the blue EL emission bands are also lost upon quenching, although a large amount of all EL emission intensity is also removed which is consistent with these findings. It has only been possible to collect powder diffraction data for just a few grains of phosphor in a printed ACEL panel due to the high flux X-ray source provided by synchrotron radiation. XRPD of a working ACEL device is shown in Figure 4.13. This work is a novel approach toward studying the crystal structure of zinc sulfide crystals; that is analysis of the crystal structure under an electric field. No such work has been reported to date. When the AC field is applied across the EL phosphor the diffraction peaks are all observed to shift, but remain within the region where broad diffraction intensity is observed for a normally collected powder sample, (i.e. random orientation). Indeed the sharp diffraction lines are observed to span across each broad diffraction area associated with the sphalerite phase. The panel exhibits a different diffraction pattern when the device is powered in an AC field even though the phosphor is fixed in the binder (no dielectric powder was added to the panel). These in panel data (off and on) show multiple sharp diffraction lines spread out under the region which is shown using capillary data to manifest broad diffraction intensity. This indicates that the phosphor powder is comprised of unique crystals each having a different (faulted) structure. One hypothesis is that the particles will reorient based on the way they are placed against the field. A dipole moment arising from the piezoelectric effect would cause the particles to move under the alternating field. All crystals in a ferroelectric state are also piezoelectric

and when a stress is applied to the crystal its electric polarization is altered. Hence an electric field applied to a crystal will cause the crystal to become strained; when the crystal is stressed it will develop polarization in the direction of the field⁸⁰. Again, this polarization can be hypothesized to be the stimulating factor affecting electronic configuration of the Cu luminescent centres within the lattice.

When investigating the intensity of the peaks relating to various planes, after thermal quenching of the material most, but not all, peaks seem to have been affected in a way that untreated sample shows a more intense signal. The peak intensity can be interpreted as a quantitative factor in respect of crystallinity of the material. Considering that the material does possess cubic structure, along with some degree of hexagonal distortion, the results demonstrate lowering of the peaks relative to either crystal structure form. It can be concluded that the quenching of the material affects that particular structure. In fact these studies were carried out in order to gain an in-depth insight in to the way the quenching affects the crystal structure. The results of this analysis are presented in Figures 4.16 and 4.17. The percentage by which some main peaks were reduced in intensity after quenching relative to the untreated sample was calculated. As can be seen from Figure 4.17, both hexagonal and cubic crystal planes are affected, however the degree to which each plane is affected is very variable.

The conversion of hexagonal to cubic phase involves rearrangement of a modular layer stacking pattern from ABABABA... to ABCABC... and this can be achieved by the insertion of deformation faults into the structure. Layer stacking faults may be located

randomly, non-randomly or periodically in the lattice. During the synthesis of these materials, which involves double firing of the phosphor at above and then below the cubic to hexagonal phase transition i.e. $\sim 1024^{\circ}\text{C}$, the hexagonal to cubic conversion occurs upon annealing the wurtzite modification at temperature below the transition temperature. Previously it has been reported that this is initiated by random insertion of deformation faults in the ABABA... structure⁸¹. These faults arise due to slippage of two parts of the crystal past each other and hence provide the nuclei for cubic region to grow. This cubic structure has been reported to be highly twinned along the (111) h, k, l axis⁷². Overall the 111 twinned cubic phase of the zinc sulfide doped with copper appears to be implicated in the ac electroluminescence of the material. As demonstrated in Figure 4.17, the intensity of the signal related to the 111 axis has reduced to a factor of $\sim 32\%$, however other planes demonstrate reduction in intensity. This may explain the slight reduction the ac electroluminescence property of the material after quenching but does not clearly explain the change in the emission wavelength already discussed. However, it allows an argument for possible reduction in the green emission intensity due to the affected 111 plane, which would then indicate that the blue emissions arise from a different set of crystal plane or properties.

7.5 Panel analysis

In defining a relationship between the luminance of a panel and the applied voltage, when using commercial Sylvania samples, the most accurate model was equation 6.2. Hence the constant 'a' can be regarded as a factor relating directly to the property of the phosphor material. However when sample D1 was investigated equation 6.2 seemed to be inaccurate and instead equation 6.3 was a more accurate form of defining the relationship. This can only be explained through the difference in the particle size of the two phosphors. The commercial sample had an average particle size of ~20 microns while the D1's average size range was ~5 microns, thereby suggesting that perhaps the particle size itself was a major factor when considering the luminance of these particles against the voltage applied. The electric field is the driving force behind AC-electroluminescence and hence it can be argued that the interaction of the electric field with the particles is different when different particle sizes are considered. At the same time the particle size distribution in these materials can never be homogenous hence causing an error factor when defining a mathematical relationship for their EL properties. An alternative hypothesis for the difference between D1 and the commercial sample is that since the D1 samples were smaller, the actual phosphor film's thickness in the panel may have resulted in equation 7.3 being more accurate, however, when 12 and 23 micron spacers were used to compensate for this difference; nevertheless, equation 6.3 was just as favourable.

When considering the major drawback of ACEL technology i.e. its short life time and degradation characteristics, defining a mathematical model of its emission degradation is a step towards understanding part of the mechanism of the ACEL process. The 400 Hz

frequency was initially investigated and the models to define a relationship for the decay of luminescence were analysed. The most accurate mathematical relationships were equations 6.4, 6.5 and 6.6; however even these models were not as accurate when considering the relevant R squared factor. Equation 6.6 was statistically chosen as the most probable relationship. However, the frequency of the driving voltage directly affects both the luminance in terms of generating brighter EL effect while at the same time enhancing the degradation of the panel i.e. the frequency affects a parameter (emission brightness) both in a positive and negative manner at the same time, an indication of the frequency has a role in the EL process. As a result, as mentioned in chapter 6, using an extensively large pool of data, equation 6.7 was proposed and tested for accuracy as an indicative model that may relate the driving voltage, frequency and luminance output of an ACEL panel. This model statistically seems accurate with an R squared value of 0.9954. However the fit is only specific to the particular panel under study.

At the same time in order to define the relationship between luminance decay and the relevant frequency of the driving voltage three models were investigated: 6.8a, 6.8b and 6.8c; from which the 6.8c model was statistically the most accurate. This model defines three parameters A, B and C and these were calculated and presented in Table 6.6. These factors seem to increase as the frequency of the driving voltage is increased to 20 KHz, however the 30KHz data are to some degree lower than the 20 KHz values. This coincides with the fact that when above 20 KHz the panel no longer demonstrates a brighter EL property. The key conclusion of these observations is that independent from the voltage and luminance properties of the phosphor each particular frequency affects the three factors (A, B & C) adding to the complication of defining a mathematical model

for ACEL process. This would be even more challenging when considering that for each batch of zinc sulfide phosphor materials, the relationship between voltage and luminance is unique depending on the particle size distribution, as discussed earlier. Using the sample D1 and an extensive set of data at various driving voltages, frequency and the 12 and 23 micron spacer in the panel an attempt was made to arrive at an overall fundamental mathematical relationship that would synchronise these data and could be used as a model for estimating a phosphor's performance at particular frequency and voltage. The method of this analysis is presented in chapter 6. The overall calculations led to deriving the mathematical model: equation 6.15. This fit was derived both for panels with 23 micron and the 12 micron spacer. However when this model was used in parallel to practical results, it failed to estimate the luminescence of the panel when actual practical observations were considered. Even though it was statistically the most accurate model, it failed to be practically viable; possibly due to the multiple factors that affect the ACEL property of the materials. For example as discussed and demonstrated earlier, the frequency of the driving voltage affects the luminance and the decay of the material positively in parallel and hence would create contradicting outcomes when considering a mathematical correlation.

Considering that zinc sulfide can exhibit two different crystal structures depending on the firing temperature; cubic below 1000°C and hexagonal above this temperature, it was an interesting idea to compare these two crystal structures in terms of their possible effect on the ACEL. It is concluded that with both samples the already discussed $lum = a \cdot volt^\alpha$ fit is most accurate. The estimated values of the two parameters of this relationship (a & α) are demonstrated in Figures 7.2 & 7.3 in a graphical format.

It is clear from the results that the hexagonal crystal structure demonstrates lower values for 'a' with a sharp drop when the frequency of the driving voltage is increased while α seems unaffected in relation to the crystal structure. This further enhances the earlier argument that α is a factor relating to the particle size of the materials while a is a parameter that is directly influenced by possible core factors such as band energy or copper distribution within the lattice. Figure 7.2 demonstrates the way in which parameter 'a' from equation 6.2 is affected by the frequency of the driving voltage in cubic and hexagonal AMT samples and Figure 7.3 demonstrates the effect on parameter α .

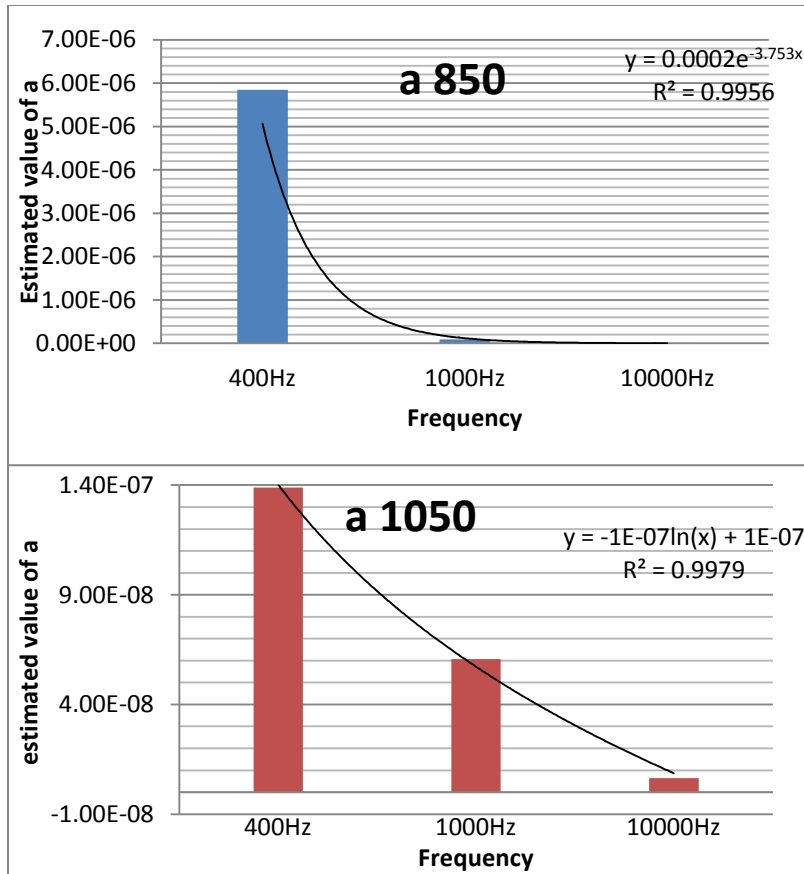


Figure 7.2: Estimated values of 'a' at various frequencies in respect of formula 7.2 for AMT850 and AMT1050 samples. This parameter is affected more intensely in cubic crystal structure.

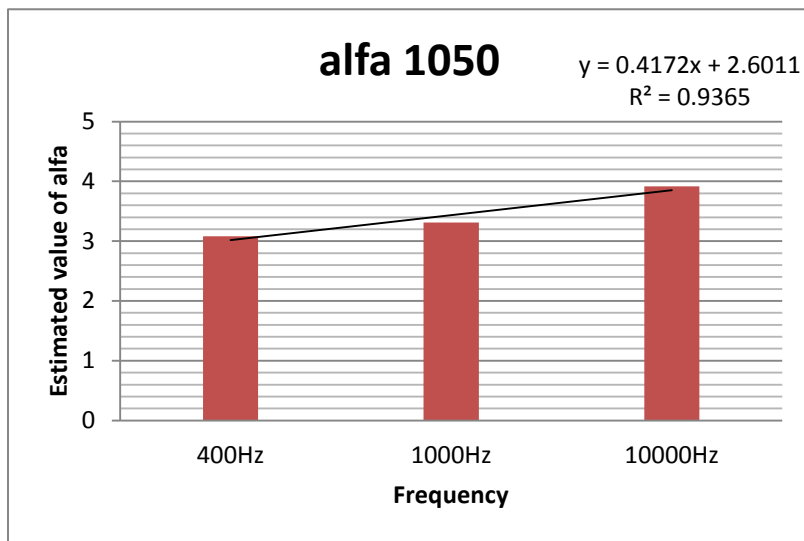
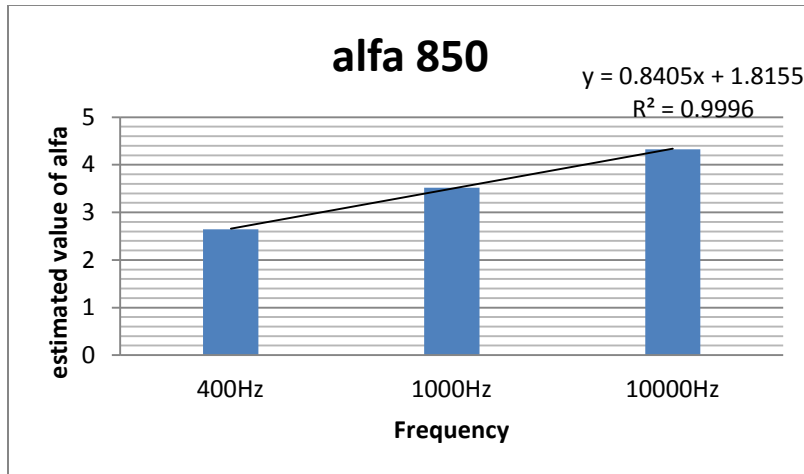


Figure 7.3: Estimated values of ‘ α ’ at various frequencies in respect of formula 7.2 for AMT850 and AMT1050 samples. This parameter seems to be effected similarly for both cubic and hexagonal crystal structures.

The difference between the hexagonal and cubic phase of zinc sulfide in terms of its ACEL properties is also apparent when considering the decay of the luminance at high frequencies considering equation 6.8c.

AMT 850 Freq (Hz)	<i>A</i>	<i>B</i>	<i>c</i>
15000	0.1874E-5	-0.3486E-2	4.4181
20000	0.1933E-5	-0.3566E-2	4.4355

AMT1050 Freq (Hz)	<i>A</i>	<i>B</i>	<i>c</i>
15000	0.5974E-8	-0.4810E-3	2.1561
20000	0.2777E-6	-0.0880E-3	2.5682

Table 7.1: Estimating the parameters of formula 6.8c for AMT850 and AMT 1050 at different frequencies.

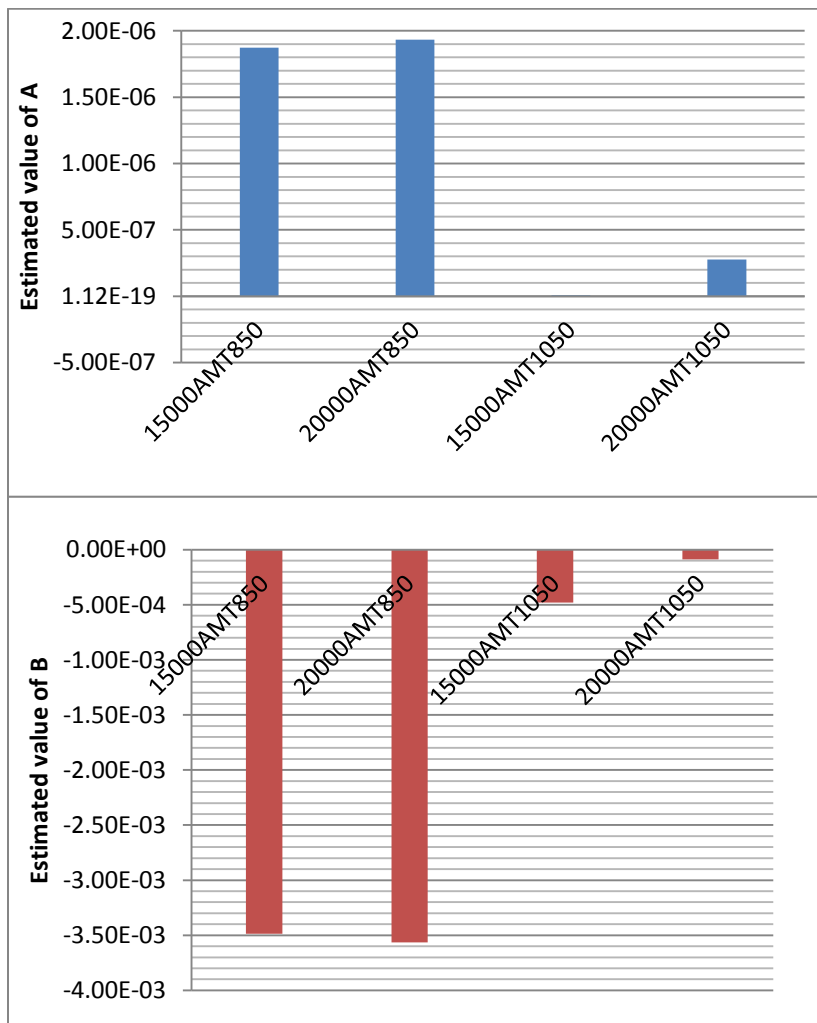


Figure 7.4: Estimating the parameters (A and B) of formula 6.8c for AMT850 and AMT1050 at different frequencies.

These values are highlighted in Table 7.1 and Figure 7.4. Based on the defined equation of luminescence loss over time for each particular frequency, the parameter ' B ' is significant in a way which the more negative its value, the swifter the loss of luminance at that particular frequency. The parameter ' A ' shows an opposing response; the higher it is the more stable is the phosphor's luminescence over time (Figure 7.4).

Based on this study it can be concluded that the hexagonal crystal structure which is formed at higher temperatures is more stable in comparison to the cubic structure because the atomic positions within the lattice are more stable in hexagonal configuration due to the closer packing of them while in cubic structure comparatively it is not as stable.

7.6 Conclusion

Based on the findings and the issues discussed in this research, it can be hypothesized that the mechanism of the ACEL process may involve formation of nano p-n junction across the particles where copper doped zinc sulfide forms the p type region and the higher zinc containing regions due to the evaporation of sulphur form the n type region. The vibration of the interstitial copper atom under an alternating field may affect the permeability of charge carries in these p-n junctions's environment; hence electron injection occurs and luminescent centres are activated.

High frequency of the power source creates more energetic and vigorous vibrations of the interstitial copper. Under higher frequencies, the enhanced vibrational energy (considering the piezoelectric property of ZnS) may lead to dislocation of the interstitial copper from its optimum location of and as a result EL emission will be reduced.

D1 & D2 sample preparation technique which involves addition of raw zinc sulfide to an already copper doped zinc sulfide creates higher occurrence of nano p-n junctions species within the lattice (particularly the n type) relative to the other methods discussed and that may be the reason for their brighter emission. Larger particles have higher probability of containing interstitial copper sites during firing as copper atoms tend to migrate out of the zinc sulfide lattice toward the surface. Hence larger particles (commercial) demonstrate better emission properties.

Thermal quenching affects the interstitial copper sites more than the other luminescent centres formed of substitutional copper sites. Hence the lowered blue emission occurs.

Due to the vast dispersing probability of Cu atoms within the ZnS lattice an affirmative mathematical model cannot be developed for an EL panel.

Exafs analysis cannot be fully relied up on in respect of the copper environment in these phosphors considering that a small fraction of the copper impurity the phosphor exists as an interstitial site. However, the Xanes results do confirm an alternation of the Zn atoms electronic configuration when samples are quenched. Double firing technique, creates better distribution of copper within the lattice as the sodium chloride flux prevents this if only the single firing procedure is conducted. Piezoelectric effect is an important factor in the emission and degradation property of these materials as demonstrated from mixing Barium titanate and strontium titanate along with under field XRPD analysis of the panels.

7.7 Future work

The experiments in this research covered many aspects of copper doped zinc sulfide ACEL phosphors. Their crystal structure and morphology along with emission properties and synthesis techniques were investigated. The copper doped zinc sulfide phosphors emit light in the green and blue regions of the electromagnetic spectrum, which as discussed is related to the copper luminescent centres. This would suggest that the nature of the doping element is a fundamental aspect of emission properties. Hence, any future work on electroluminescent phosphors should involve investigation of other potential ACEL host lattices and doping elements with the objective of allocating a host lattice that does not demonstrate degradation under high frequency/time and doping elements that would enable the emission of electromagnetic waves in the red and infra-red region of the spectrum. The proposed hypothetical mechanism of action highlighted in conclusion can be further investigated by fabricating ZnS:Cu/ZnS light emitting diodes to evaluate the proposed mechanism of action assumed in this research. Drift velocity of charges (e or h) can be analysed in terms of the conductivity of single ZnS:Cu particles and comparative studies carried out. The conductivity of the particles should be analysed under electric fields and neutral conditions.

However, due to the economic constraints involving the high cost of research and development in this particular field, prior to any further investigation, a realistic proposal should be made on where this technology can commercially accommodate itself when currently light emitting diode (LED), LCD and plasma technologies have monopolised specific parts of the market as there have been substantial investments in this area. The

one distinctive advantage of ACEL panels is the very thin & flexible panel structure that can be produced via this technology and hence decorative interior lighting of luxury automobiles and aircrafts can be considered a potential market, especially that these panels demonstrate a low energy consumption and they can be shaped to a great extent to be aligned with curves and angles in the environment they are used for. Hence further research can also be directed toward the substrates which these panels are prepared on and enhancement of implementing curves and shapes to the actual panels.

REFERENCES

- ¹ Kroger, F, A. & Hellingman, J, E. (1949). J. Electrochem. Soc., **95**, 68.
- ² Van Goole, W. (1961). Philips. Res. Rept. Suppl., **3**, 664.
- ³ Shionoya, S. Urabe, K. Koda, T. Era, K & Fujiwara, H. (1968). J. Phys. Chem .Sol., **29**, 935.
- ⁴ Urabe, K. Shionoya, S. (1968).J. Phys. Soc. (Japan), **25**, 1611.
- ⁵ Stanley, J. Jiang, Y. Bridges, F. Carter, S, A. & Ruhlen, L, S. (2010). J. Phys. Condens. Mat., **22**, 055301.
- ⁶ Kroger, F, A. (1940). Physica, **7**, 1.
- ⁷ Shinoya, S. Koda, T. Era, K. & Fujiwara, H. (1964). J. Phys. Soc. (Japan), **19**, 1157.
- ⁸ Shinoya, S. Koda, T. Era, K. & Fujiwara, H. (1966). J. Phys. Chem. Sol., **27**, 865.
- ⁹ Bowers, R. & Melamed, N, T. (1955).Phys. Rev., **99**, 1781.
- ¹⁰ Apple, E,F. & Prener, J, S. (1960). J. Phys. Chem. Solids, **13**, 81.
- ¹¹ Suzuki, A. & Shionoya, S. (1971). J. Phys, Soc. (Japan), **31**, 1455.
- ¹² Blinks, H. Riehl, N. & Sizmann, R. Z. (1961). Phys., **163**, 594.
- ¹³ Holton, W, C. De wit, M. Watts, R, K. Estle, T, L. & Schneider, J. (1969). J. Phys. Chem. Solids, **30**, 963.
- ¹⁴ Tabei, M. Shionoya, S. & Ohmatsu, H. (1975). J. Appl. Phys. (Japan) **14**, 240.

-
- ¹⁵ Tabei, M. Shionoya, S. (1977). *J. Lumin.*, **15**, 201.
- ¹⁶ Yang, Z.Ch. (1983). *Faguang Yu Xianshi*, **3**, 85.
- ¹⁷ Kokin S, M. Mikov, S, N, B. & Puzovb I. P. (2001). *J. Appl. Spectrosc.*, **68**, 962.
- ¹⁸ Khosravi, A. & Kundu, M. (1995). *Appl. Phys. Lett.*, **67**, 2702.
- ¹⁹ Yang, Y. & Duke, C, B. (1987). *Phys. Rev.*, **B36**, 2763.
- ²⁰ Yen, W,M. Shionoya, S. & Yamamoto, H. (2007). 'Phosphor Handbook' 2nd Edition, London: CRC press.
- ²¹ Neumark, G, F.(1997). *Mater. Sci. Eng.*, **R21**, 1.
- ²² Watkins, G, D. (1973).*Solid. State Com.*, **12**, 589.
- ²³ Bube, R. (1978). 'Photo conductivity of solids'. New York: Rob Kreiger Publishing.
- ²⁴ O'Brien, T. Zerner, M, C. Rack, P, D & Holloway, P, H. (2000). *J. Electrochem. Soc.*, **147**, 792.
- ²⁵ Pickering, H, S. (1978). 'The Covalent bond'. London: Wykenham Publications.
- ²⁶ Gerloch, M. Salde, R.C.(1973) 'Ligand field parameters' .London: Cambridge university press.
- ²⁷ Harrison, W,A. (1980). '*Electronic structure and properties of solids*'. San Francisco: Freeman & company.

-
- ²⁸ Harrison, W, A. (1990). Phys. Rev., **B41**, 6008.
- ²⁹ Harrison, W, A. (1985). Phys Rev., **B31**, 2121.
- ³⁰ Harrison, W,A. (1980). *'Electronic structure and properties of solids'*. San Francisco: Freeman & Company.
- ³¹ Savchenko, N. D. Shchurova, T.N. Popovych, K.O. Rubish, I.D. Leising, G. (2004). Semiconductor. Phys. Quant. Elec. & Photoelectronics, **7**, N2, 133.
- ³² Kolomoitsev, F, I. Nemchenko, A, M & Perekrestova, L,G. (1971). Electroluminescence of Solids, in: Proc. III Electroluminescence Meeting. Kiev, 71.
- ³³ Destriau, G. (1947). Phil. Mag., **38**, 700, 774.
- ³⁴ Destriau, G. (1936). J. Chem. Phys., **33**, 620.
- ³⁵ Chakrabarti, K. Mathur, V,K. Rhodes, J,F. & Abbundi, R,J. (1988). J. Appl. Phys., **64**, 1362.
- ³⁶ Sze, S.M. (1981). *'Physics of Semiconductor Devices'*, 2nd Edition. New York: John Wiley & Sons.
- ³⁷ Shockley, W. (1961).Solid-State Electron, **2**, 35.
- ³⁸ Bringuier, E. (1994). J.Appl. Phys., **75**, 4291.
- ³⁹ Bhattacharyya, K. Goodnick, S.M. & Wager, J.F. (1993). J. Appl. Phys., **73**, 3390.
- ⁴⁰ Destriau, G. (1936). J. Chem. Phys., **33**, 620.

-
- ⁴¹ Fischer, A.G. (1962). *J. Electrochem. Soc.*, **109**, 1043.
- ⁴² Zalm, P. (1956). *Philips. Res, Rep.* 11, **353**, 417.
- ⁴³ Cramer, D. Haaranen, J. & Pitkanen, T.(1993). *Application Digest of 1993 SID international symposium.* 57.
- ⁴⁴ Barrow ,W. Coovert, R, E. King, C, N.(1998). *Application digest of 1988 SID international symposium.* 284
- ⁴⁵ Harris, D, C. & Bertolucci, M,D.(1978). *'An introduction to vibrational and electronic spectroscopy'*. Oxford: Oxford university press.
- ⁴⁶ Fischer, A,G. (1966). *'Electroluminescence in II-IV compounds, in luminescence of inorganic Solids'*. New York: Academic press.
- ⁴⁷ Cramer, D. Haaranen, J. & Pitkanen, T.(1993). *Application digest of 1993 SID international symposium, 57.*
- ⁴⁸ Fischer, A,G. (1963). *J. Electrochem. Soc.*, **110**, 733.
- ⁴⁹ Ono, Y. Shirage, N. Kadokura, H & Yamada, K. (1990). *Inst. Electron, Inform. Com. Eng. Tech. Rep.*, **89**, 378.
- ⁵⁰ Stanley, J. Bridges, F. Jiang, Y. Carter, S. Ruhlen, L. (2010). *J. Phys. Condens. Matter.*, **22**, 1
- ⁵¹ Medling, S. France, C. Balaban, B. Bridges, F. Carten, S. (2011). *J. Phys:D: Appl. Phys.* **44**. 5402
- ⁵² Howard, W,E. (1981). *Proc. Soc. Inform. Display.*, **22**, 47.

-
- ⁵³ Lines, M, E. Glass, A, M. (1977). '*Principles and Applications of Ferroelectrics and Related Materials*'. Oxford: Clarendon Press.
- ⁵⁴ Burfoot, J, C. Taylor, G ,W. (1979). "*Polar Dielectrics and Their Applications*". London: Macmillan.
- ⁵⁵ Vecht, A. Werring, N.J. Ellis, R & Simth, J.F. (1973). Proceedings of IEEE., **61**, 902.
- ⁵⁶ Zworykin, V,K. (1938). U.S Patent # 2,141,059 December 20.
- ⁵⁷ Fransworth, P,T.(1930). U.S Patent # 1,773,980 August 26.
- ⁵⁸ Kawamoto, H. (2002). Proceedings of the IEEE, 90, 4.
- ⁵⁹ de Gennes, P,G. & Prost, J.(1995). '*The physics of liquid crystals*'^{2nd} Edition, Oxford: Oxford university press.
- ⁶⁰ Jacobsen, S,M. Stoffers, C. Yang, S. & Jacobsen S. M. (1996). J. SID, **4**, 331.
- ⁶¹ Nasser Hajibagheri, M, A., (1999), '*Methods in Molecular Biology*', 117, Humanna Press.
- ⁶² Jenkins, R. Jenkins, A. & Snyder, B. (1996). '*Introduction to X-ray powder diffractometry*', London: Wiley-interscience.
- ⁶³ Kelly, S,D. Hesterberg, D. & Ravel, B. (2008). '*Analysis of Soils and Minerals Using X-ray Absorption Spectroscopy*'. Part 5 -Mineralogical Methods, (A.L. Ulery and L.R. Drees, Eds.). Soil Science Society of America, Madison, WI, USA, 367

-
- ⁶⁴ Erko, I. Packe, W. Gudat, N. Abrosimov, Firsov, A. (2000). 'A Graded Crystal Monochromator at BESSY II'. SPIE **4145**.122.
- ⁶⁵ Alcock, N,W. (1995) Anal. Chem., 67, **12**, 503
- ⁶⁶ Raymond , L, L. (1998). Appl. Optics., 37, **9** ,1506.
- ⁶⁷ Goldstein, J, I. (2003). 'Scanning Electron Microscopy and X-Ray Microanalysis'. 3rd edition. New York: Springer.
- ⁶⁸ Davies, D, A. Silver, J. Vecht, A. Marsh,P, J. & Rose, J, A. (2001). J. Electrochem. Soc., **148**, H143
- ⁶⁹ Gillson, J, J, L. & Darnell, F,J. (1962). Phys. Rev., 125, **1**, 149.
- ⁷⁰ Silver, J. Withnall, R. Fern, G, R. Marsh, P, J. Ireland, T,G. & Salimian, A. (2006) 'International display workshop'. 6-8 Dec, (Ostu, Japan).
- ⁷¹ McKeag, A, H. & Steward, E, G. (1957).J. Electrochem. Soc., **104**, 41.
- ⁷² Thompson, S, P. Parker, J, E. Potter, J. Cobb, T, M. & Tang, C, C. (2009). Rev. Sci. Inst., **80**, 075107.
- ⁷³ Withnal, R. Silver, J. Fern, G.R. Salimian, A. *The 13th international workshop on organic and inorganic electroluminescence & 2006 internal conference on the science and technology of emission displays and lighting Report*, (2006), (South Korea) **18-22**, 108.
- ⁷⁴ Skobeltsyn, D.V. (1972). Electroluminescence, **50**, 1.

-
- ⁷⁵ Suzuki, A. & Shionoya, S. (1971). *J. Phys. Soc. (Japan)*, **31**, 1455.
- ⁷⁶ Patel, J, L. Davies, J, J. & Nicholls, J, E. (1981). *J. Phys.*, **C14**, 5546.
- ⁷⁷ Withnall, R. Silver, J. Ireland, T,G. Fern, G, R. & Marsh, P, J. (2009). *J. Electrochem. Soc.*, **156**, 326.
- ⁷⁸ Wright, A, C. & Viney, I. V. F. (2001). *Philos. Mag. (B)*, **81**, 279.
- ⁷⁹ Fleet, M, E. (1977). *Am. Mineral.*, **62**, 540.
- ⁸⁰ Kittel, C. (1968). *'Introduction to solid state physics'*. New York, London, Sydney: Wiley Publications.
- ⁸¹ Sebastian, M.T. Krishna, P. (1994). *'Random, non-random and periodic faulting in Crystals'*. Amsterdam: Gordon and Breach Science.

Appendix

A1

$$lum = a.volt + d \quad (6.1)$$

	a	d
$R^2 = 0.994452$ $\bar{R}^2 = 0.994199$		
Parameter estimate	0.416863	-24.1006
SE	0.006638	1.21692
t statistics	62.7946	-19.8046
P-value	0.00	0.00

$$lum = a.volt \quad (6.2)$$

	a
$R^2 = 0.994452$ $\bar{R}^2 = 0.994452$	
Parameter estimate	0.350379
SE	0.014375
t statistics	21.1338
P-value	0.00

$$lum = a.volt^\alpha \quad (6.3)$$

	$\ln a$	α
$R^2 = 0.958499$ $\bar{R}^2 = 0.956612$		
Parameter estimate	-8.48701	2.3481
SE	0.511401	0.104173
t statistics	-16.5956	22.5411
P-value	0.00	0.00

Statistical analysis of the proposed relationship equations (6.1-6.3) relating voltage and luminance in an ACEL panel.

A2

$$lum = a.time + d \quad (6.4)$$

$R^2 = 0.952383$ $\bar{R}^2 = 0.948054$	a	d
Parameter estimate	0.00329009	49.8432
SE	0.000221813	0.051568
t statistics	-14.8327	966.549
P-value	0.00	0.00

$$lum = a.time^{\alpha} \quad (6.5)$$

$R^2 = 0.93506$ $\bar{R}^2 = 0.929157$	a	α
Parameter estimate	0.00262995	-0.0071849
SE	0.0026299	0.0005709
t statistics	1493.92	-12.5852
P-value	0.00	0.00

$$lum = e^{a.time+d} \quad (6.6)$$

$R^2 = 0.953845$ $\bar{R}^2 = 0.949649$	a	d
Parameter estimate	0.00006685	3.9089
SE	0.00000443	0.0010308
t statistics	15.0774	3791.98
P-value	0.00	0.00

Statistical analysis of the proposed equations 6.4, 6.5 and 6.6 relating time and luminance of the panel.

A3

$R^2 = 0.995422$ $\bar{R}^2 = 0.995256$	ln A	α	β
Parameter	-13.0451	0.881419	2.25853
S.E.	0.151088	0.13889	0.0263
t-Statistics	-86.3415	63.461	85.8761
P-value	0.00	0.00	0.00

Statistical analysis of equation (6.7).

A4

Variables & Diagnoses For 1KHz Data		T²	T	intercept	R²	Adj. R²
Model (6.8a)	Parameter	A	B	C	0.78125	0.78125
	Estimated Value	-	0.147867	-		
	S.E.	-	0.015249	-		
	t-Statistics	-	9.696746	-		
	Prob.	-	0.000	-		
Model (6.8b)	Parameter	A	B	C	0.991724	0.991501
	Estimated Value	-	0.00643-3	4.182506		
	S.E.	-	9.66E-05	0.002236		
	t-Statistics	-	- 66.5884	1870.143		
	Prob.	-	0.000	0.000		
Model (6.8c)	Parameter	A	B	C	0.99771	0.99758
	Estimated Value	4.78E-05	- 0.008351	4.194795		
	S.E.	4.93E-06	0.000204	0.00174		
	t-Statistics	9.700396	-408688	2410.861		
	Prob.	0.000	0.000	0.000		

Statistical analysis of equations (6.8a-c) at 1KHz frequency

A4

Variables & Diagnoses For 10KHz Data		T²	T	intercept	R²	Adj. R²
Model (6.8a)	Parameter	A	B	C	0.647.375	0.647.375
	Estimated Value		0.18814			
	S.E.		0.019483			
	t-Statistics		9.656842			
	Prob.		0.000			
Model (6.8b)	Parameter	A	B	C	0.984565	0.984148
	Estimated Value		-0.008995	5.343614		
	S.E.		0.000185	0.004286		
	t-Statistics		-48.58214	1246.702		
	Prob.		0.000	0.000		
Model (6.8c)	Parameter	A	B	C	0.998540	0.998459
	Estimated Value	0.000103	-0.013108	5.3699964		
	S.E.	5.53E-06	0.000229	0.001950		
	t-Statistics	18.56046	-57.24114	2753.972		
	Prob.	0.000	0.000	0.000		

Statistical analysis of equations (6.8a-c) at 10 KHz frequency.

A4

Variables & Diagnoses For 20KHz Data		T²	T	intercept	R²	Adj. R²
Model (7.6a)	Parameter	A	B	C		
	Estimated Value	-	0.197069	-	0.821.1634	0.821.1634
	S.E.	-	0.020285	-		
	t-Statistics	-	9.714854	-		
	Prob.	-	0.000	-		
Parameter	A	B	C			
Model (7.6b)	Estimated Value	-	-	5.563702	0.953672	0.952420
	S.E.	-	0.000297	0.006860		
	t-Statistics	-	-	810.301427.59811		
	Prob.	-	0.000	0.000		
	Parameter	A	B	C		
Model (7.6c)	Estimated Value	0.000166	-	5.606260	0.996306	0.996101
	S.E.	8.13E-06	0.000337	0.002868		
	t-Statistics	20.3836	-	1955.10344.03207		
	Prob.	0.000	0.000	0.000		
	Parameter	A	B	C		

Statistical analysis of equations (6.8a-c) at 20 KHz frequency.

A4

Variables & Diagnoses For 30KHz Data		T²	T	intercept	R²	Adj. R²
Model (6.8a)	Parameter	A	B	C	0.747.866	0.747.866
	Estimated Value	-	0.194819	-		
	S.E.	-	0.020099	-		
	t-Statistics	-	9.692743	-		
	Prob.	-	0.000	-		
Model (6.8b)	Parameter	A	B	C	0.966721	0.965822
	Estimated Value	-	- 0.008557	5.512765		
	S.E.	-	0.000261	0.006042		
	t-Statistics	-	- 32.78430	912.4476		
	Prob.	-	0.000	0.000		
Model (6.8c)	Parameter	A	B	C	0.997887	0.996101
	Estimated Value	0.000147	- 0.014453	5.550541		
	S.E.	6.38E-06	0.000264	0.002252		
	t-Statistics	23.04048	- 54.65038	2464.914		
	Prob.	0.000	0.000	0.000		

Statistical analysis of equations (6.8a-c) at 30 KHz frequency.

A5

Sample	$lum = a.Volt^\alpha$ Determination coefficient \bar{R}^2	$lum = a.Volt$ Determination coefficient \bar{R}^2
Standard	0.990307	0.998243
B2	0.993340	0.999681
B4	0.995887	0.999387
B6	0.993960	0.999857
S2	0.994436	0.995603
S4	0.985766	0.995439
S6	0.976883	0.996638

Comparison of the equation (6.3) and (6.2) in terms of accuracy relating to the voltage vs. luminance effect when powder dielectric materials were mixed with the phosphor grains.

Sample	Estimated value of (a)
Standard	0.359765
B2	0.284097
B4	0.205508
B6	0.180847
S2	0.193124
S4	0.124394
S6	0.107800

Estimation of parameter (a) considering equation (6.2) as the most accurate model.

A6

$lum = a.Volt^\alpha$	$\ln a$	α
$R^2 = 0.993881$		
$\bar{R}^2 = 0.993541$		
Parameter estimate	-14.2508	3.24426
SE	0.26541	0.06
t statistics	-53.6937	54.0709
P-value	0.00	0.00
$lum = a . Volt$	a	
$R^2 = 0.910894$		
$\bar{R}^2 = 0.910894$		
Parameter estimate	0.045184	
SE	0.0050678	
t statistics	8.9158	
P-value	0.00	

Statistical evaluation of the equation (6.2) & (6.3) and estimated parameters for DI samples.

Data series	Determination coefficient \bar{R}^2
12 Micron (a)	
50Hz	0.971300
100Hz	0.982945
150Hz	0.993541
200Hz	0.922220
250Hz	0.993499
300Hz	0.989250
400Hz	0.986563
1000Hz	0.943536
5000Hz	0.994903
10000Hz	0.987095
15000Hz	0.992282
20000Hz	0.981809

Statistical analysis of the equation 6.3 at different frequencies for sample D1 using the 12 μ m spacer.

A6

Data series 23 Micron (b)	Determination coefficient \bar{R}^2
50Hz	0.989092
100Hz	0.989611
150Hz	0.990144
200Hz	0.992028
250Hz	0.989862
300Hz	0.990764
400Hz	0.988940
1000Hz	0.988355
5000Hz	0.989009
10000Hz	0.990057
15000Hz	0.987582
20000Hz	0.992056

Statistical analysis of the equation 6.3 at different frequencies for sample D1 using the 23 μm spacer.

A6

Frequency (Hz) 12 Micro spacer	$\ln a$	α
50	-11.3695	2.64171
100	-13.8533	3.14014
150	-14.2508	3.24426
250	-15.1433	3.45319
300	-15.8597	3.60953
400	-16.1538	3.68965
1000	-17.1443	3.97897
5000	-17.9138	4.18103
10000	-18.9942	4.37914
15000	-19.2704	4.40209
20000	-19.035	4.32455

Frequency (Hz) 23 Micron spacer	$\ln a$	α
50	-15.2736	3.48
100	-15.7744	3.65306
150	-16.5217	3.81810
250	-17.1292	3.95723
400	-17.5179	4.08288
1000	-17.715	4.19908
5000	-18.4875	4.42828
10000	-19.7251	4.66909
15000	-20.176	4.7675
20000	-20.9287	4.9218

Estimating each parameter for 12 and 23micron spacer at various frequencies.

A7

$\alpha = \rho \cdot \text{freq} + m$ (a) $R^2 = 0.554739$ $\bar{R}^2 = 0.505265$	ρ	m
Parameter estimate	0.0000608	3.44249
SE	0.000018157	0.150063
t statistics	3.34856	22.9403
P-value	0.00	0.00

$\alpha = \rho \cdot \text{freq}^\beta$ (b) $R^2 = 0.877328$ $\bar{R}^2 = 0.863698$	$\ln \rho$	β
Parameter estimate	0.820933	0.071103
SE	0.63018	0.0088625
t statistics	13.027	8.02288
P-value	0.00	0.00

$\alpha = \text{freq}^\beta$ (c) $R^2 = 0.877328$ $\bar{R}^2 = 0.877328$	β
Parameter estimate	0.181658
SE	0.010795
t statistics	16.8272
P-value	0.00

$\alpha = \rho \cdot \text{freq}^\beta$ (d) $R^2 = 0.885073$ $\bar{R}^2 = 0.870707$	$\ln \rho$	β
Parameter estimate	0.789281	0.076908
SE		
t statistics	11.9017	7.84918
P-value	0.00	0.00

Statistical analysis of equations 6.9-12 and estimated parameters using 12 micron spacer.

A8

$lum = a.volt$ AMT850- 400Hz	a	α
Parameter	0.043070	-
S.E.	0.003977	-
t-statistics	10.8284	-
P-value	0.00	-
$R^2 = 0.997157$		$\bar{R}^2 = 0.997157$

$lum = volt^\alpha$ AMT850- 400Hz	ln a	α
Parameter	-	0.342437
S.E.	-	0.043193
t-statistics	-	7.9281
P-value	-	0.00
$R^2 = 0.974166$		$\bar{R}^2 = 0.974106$

$lum = a.volt^\alpha$ AMT850- 400Hz	ln a	α
Parameter	-12.0486	2.64588
S.E.	0.75085	0.143794
t-statistics	-16.0462	18.4005
P-value	0.00	0.00
$R^2 = 0.974106$		$\bar{R}^2 = 0.971229$

$lum = a.volt$ AMT850- 1kHz	ln a	α
Parameter	0.066654	-
S.E.	0.00903	-
t-statistics	7.37992	-
P-value	0.00	-
$R^2 = 0.983575$		$\bar{R}^2 = 0.983575$

A8

$lum = a.volt^\alpha$ AMT850-1kHz	ln a	α
Parameter	-16.236	3.51652
S.E.	0.92154	0.177228
t-statistics	-17.6191	19.8417
P-value	0.00	0.00
$R^2=0.98253$		$\bar{R}^2=0.980035$

$lum = a.volt$ AMT850-10kHz	ln a	α
Parameter	-	0.19969
S.E.	-	0.036057
t-statistics	-	5.5375
P-value	-	0.00
$R^2=0.944727$		$\bar{R}^2=0.944727$

$lum = volt^\alpha$ AMT850-10kHz	ln a	α
Parameter	-	0.56193
S.E.	-	0.075062
t-statistics	-	7.48627
P-value	-	0.00
$R^2=0.994579$		$\bar{R}^2=0.994579$

$lum = a.volt^\alpha$ AMT850-10kHz	ln a	α
Parameter	-19.5557	4.32682
S.E.	0.62612	0.120731
t-statistics	-31.2332	35.8384
P-value	0.00	0.00
$R^2=0.994579$		$\bar{R}^2=0.993805$

Statistical analysis of voltage luminance models in respect of AMT850 sample.

A9

$lum = a.volt$ AMT1050-400Hz	a	α
Parameter	0.0096935	-
S.E.	0.0012467	-
t-statistics	7.77507	-
P-value	0.00	-
$R^2=0.981011$		$\bar{R}^2=0.981011$

$lum = volt^\alpha$ AMT1050-400Hz	$\ln a$	α
Parameter	-	0.034222
S.E.	-	0.055203
t-statistics	-	0.619924
P-value	-	0.619924
$R^2=0.992188$		$\bar{R}^2=0.992188$

$lum = a.volt^\alpha$ AMT1050-400Hz	$\ln a$	α
Parameter	-15.789	3.08106
S.E.	0.500166	0.09666
t-statistics	-31.5675	31.8754
P-value	0.00	0.00
$R^2=0.992188$		$\bar{R}^2=0.991211$

$lum = a.volt$ AMT1050-1kHz	a	α
Parameter	0.14709	-
S.E.	0.00213	-
t-statistics	0.88771	-
P-value	0.00	-
$R^2=0.965975$		$\bar{R}^2=0.965975$

A9

$lum = volt^\alpha$ AMT1050-1kHz	$\ln a$	α
Parameter	-	0.103129
S.E.	-	0.57916
t-statistics	-	1.78066
P-value	-	0.00
$R^2=0.996866$		$\bar{R}^2=0.996866$

$lum = a.volt^\alpha$ AMT1050-1kHz	$\ln a$	α
Parameter	-16.617	3.31015
S.E.	0.339536	0.065623
t-statistics	-48.9415	50.4416
P-value	0.00	0.00
$R^2=0.996866$		$\bar{R}^2=0.996474$

$lum = a.volt$ AMT1050-10kHz	a	α
Parameter	0.041392	-
S.E.	0.007211	-
t-statistics	5.73967	-
P-value	0.00	-
$R^2=0.94481$		$\bar{R}^2=0.94481$

$lum = volt^\alpha$ AMT1050-10kHz	$\ln a$	α
Parameter	-	0.272676
S.E.	-	0.065898
t-statistics	-	4.13784
P-value	-	0.003
$R^2=0.997471$		$\bar{R}^2=0.997471$

A9

$lum = a.volt^\alpha$ AMT1050-10kHz	$\ln a$	α
Parameter	-18.8572	3.91549
S.E.	0.360321	0.069709
t-statistics	-52.3345	56.1694
P-value	0.00	0.00
$R^2=0.997471$	$\bar{R}^2=0.997155$	

Statistical analysis of voltage luminance models in respect of AMT1050 sample

A10

AMT850 15kHz	<i>a</i>	<i>b</i>	<i>C</i>
Parameter	0.18741E-5	-0.34865E-2	4.41813
S.E.	0.22951E-6	0.20222E-3	0.035235
t-statistics	8.16538	-17.2404	125.392
p- value	0.00	0.00	0.00
$R^2=0.987567$		$\bar{R}=0.985495$	

AMT850 20kHz	<i>a</i>	<i>b</i>	<i>C</i>
Parameter	0.1933E-5	-0.35663E-2	4.35548
S.E.	0.23629E-6	0.0.21031E-3	0.037699
t-statistics	8.1806	-16.957	115.532
p- value	0.00	0.00	0.00
$R^2=0.985533$		$\bar{R}=0.983467$	

AMT1050 15kHz	<i>a</i>	<i>b</i>	<i>C</i>
Parameter	0.59745E-8	-0.48104E-3	2.1561
S.E.	0.45214E-7	0.44083E-4	0.6347E-2
t-statistics	0.132137	-10.9123	339.668
p- value	0.00	0.00	0.00
$R^2=0.998802$		$\bar{R}=0.998003$	

AMT1050 20kHz	<i>a</i>	<i>b</i>	<i>C</i>
Parameter	0.27779E-6	-0.88006E-3	2.56822
S.E.	0.3576E-7	0.339926E-4	0.515E-2
t-statistics	7.76844	-25.8898	498.534
p- value	0.001	0.00	0.00
$R^2=0.999151$		$\bar{R}=0.998811$	

Statistical analysis of equation 6.16 and the estimated parameters at 15 & 20kHz frequency for AMT 850 and 1050 samples.